

**Structural Characterization of Ribonucleic Acids and Their Complexes by
Negative-ion Mode Mass Spectrometry**

by

Kevin M. Ileka

**A dissertation submitted in partial fulfillment
of the requirements for the degree of
Doctor of Philosophy
(Chemistry)
in the University of Michigan
2018**

Doctoral Committee:

**Professor Kristina I. Håkansson, Chair
Professor Philip C. Andrews
Associate Professor Brandon T. Ruotolo
Professor Nils G. Walter**

Kevin M. Ileka

ikevin@umich.edu

ORCID iD: 0000-0002-2612-826X

© Kevin M. Ileka 2018

**To my support system,
Dad, Mom, Atoki, Steven, and Ruthie**

Acknowledgments

“If I have seen further, it is by standing upon the shoulders of giants.” These words by written by Sir Isaac Newton is understood to believe if not for the discoveries made by scientists that preceded him he would not have reached the scientific feats that he accomplished. The individuals that I will acknowledge (my giants) all played a part in my scientific growth and has provided me with a great foundation for my scientific journey moving forward.

There are not enough words to express my utmost appreciation to my research advisor Kristina Håkansson, for her guidance and mentorship throughout my doctoral journey. Her scientific enthusiasm and versatility has allowed me the freedom to further explore the realm of nucleic acids by studying them in the gas-phase. She has challenged me in every aspect of scientific reasoning and communication. I am extremely humbled to have worked in her research laboratory over the past half decade. I have not only grown as a scientist but also as a person as a whole.

I would like to thank my doctoral committee members, Professors Philip Andrews, Brandon Ruotolo, and Nils Walter. My committee has taught me to think like a scientist by critically evaluating data and posing the most important questions. I extend gratitude to the Ruotolo lab for accepting me with open arms when I needed instrument time on the Synapt; Dr. Jessica Rabuck-Gibbons whom I collaborated with the Chapter 3 project, Sugyan Dixit and Daniel Polasky whom helped me with the numerous python scripts needed for streamline the analysis of large data sets. I would like to acknowledge Professor Aaron Frank for his mentorship (and patience) with the computational work presented in this dissertation. Finally I need to thank the students of CHEM 242 for their valuable feedback needed to design and optimize the microfluidics laboratory experiment.

I would like to acknowledge the Håkansson Group members that I've had the pleasure to work with for the past 5 years; Dr. Di Gao, Dr. Ning Wang, Dr. Wendi Hale,

Jordan Ernst, Dr. Tao Jiang, Dr. Phillip McClory, Emma Wang, Dr. Hye Kyong Kweon, Dr. Nicolas Borotto, and Dr. Isaac Agyekum and also all of the undergraduates and rotator student. The Håkansson lab has provided me with an environment where I can be challenged scientifically and have a good time while doing so.

I would like to acknowledge my graduate school cohort; Jonathan Bennion, Matthew Gunsch, Paige Malec, Cassie Joiner, and Kyle Korshavn. It was honor experiencing graduate school with them from the first day of orientation to now. I look forward to seeing where our scientific journey takes us in the future. Furthermore, I would like to acknowledge my other friends in and out of the UM Chemistry Department; my intramural sports teammates, the post-doc social group and my roommates throughout my years in Ann Arbor (Jipu, Zheng, BJ, Eric, and Joy).

Finally, I need to thank my dearest friends and family around the world for their love, support and patience throughout all of my years. I cannot thank my parents enough for the sacrifices that they made that have allowed me to be in the position that I am in today.

Table of Contents

Dedication	ii
Acknowledgements	iii
List of Figures	ix
List of Tables	xiv
List of Schemes	xv
List of Abbreviations	xvi
Abstract	xviii
Chapter 1. Introduction	1
1.1 RNA Structure and Function	2
1.2 Mass Spectrometry	4
1.2.1 Ion Generation	4
1.2.2 Fourier Transform Ion Cyclotron Resonance Mass Spectrometry (FT-ICR MS)	6
1.2.3 Vibrational Activation	12
1.2.4 Electron-based Fragmentation	14
1.2.5 Traveling-Wave Ion Mobility Spectrometry-Mass Spectrometry (TWIM-MS)	15
1.2.6 Modeling RNA Higher Order Structure	19
1.3 RNA-Protein Complexes	21
1.3.1 Mass Spectrometric Strategies for Identification of RNA-Protein Interactions	23
1.4 Dissertation Overview	23
1.5 References	24
Chapter 2. Exploration of the Negative Ion Electron Capture Dissociation (niECD) Mechanism for RNA Oligonucleotides and Proton Transfer Reactions for Improved niECD	33
2.1 Introduction	33

2.2 Experimental	35
2.2.1 Reagents.....	35
2.2.2 Mass Spectrometry	36
2.3 Results and Discussion.....	36
2.3.1 niECD of RNA Hexamers and Mechanism of Fragmentation.....	36
2.3.2 Effect of Nucleobase Composition on Electron Capture and niECD Fragmentation Efficiency	42
2.3.3 PTR-assisted niECD of RNA Hexamers and an 11-mer	44
2.4 Conclusion	48
2.5 References.....	49
Chapter 3. Traveling-wave Ion Mobility Mass Spectrometry and Molecular Dynamic Simulations Reveal the Effects of Solution on a Gas-phase RNA Hairpin and its Small Molecule Complexes.....	53
3.1 Introduction.....	53
3.2 Experimental	55
3.2.1 Reagents	55
3.2.2 Traveling Wave Ion Mobility Mass Spectrometry	55
3.2.3...Circular Dichroism Spectroscopy.....	56
3.2.4...Molecular Modeling.....	56
3.2.4.1 Replica-Exchange Molecular Dynamics Simulations.....	56
3.4.2.2 Clustering Analysis	57
3.2.5 Competitive Ligand Binding K_D Measurements.....	57
3.3 Results and Discussion	58
3.3.1 Solvent Effects on A-site Conformation.....	58
3.3.2 Molecular Modeling.....	64
3.3.3 MeOH and pH Effects on RNA-ligand B	68
3.4 Conclusion.....	73
3.5 References	74
Chapter 4. Negative-Ion Mode Mass Spectrometry for Revealing Interaction sites within RNA-Protein Complexes and Selective Infrared Multiphoton Dissociation of RNA-peptide Crosslinks Species.....	79

4.1	Introduction	79
4.2	Experimental	81
4.2.1	Reagents.....	81
4.2.2	Non-Covalent Complex.....	82
4.2.3	Tandem Mass Spectrometry.....	83
4.2.4	Protein Digestion and LC/MS Separation	83
4.2.5	Click-Chemistry Reaction and LC/MS/MS via Data Independent Acquisition.....	83
4.3	Results and Discussion.....	84
4.3.1	MS/MS of Non-covalent RNA-peptide Complexes	84
4.3.2	Selective IRMPD of RNA-peptide Crosslinks	87
4.4	Conclusions	93
4.5	References.....	93
	Chapter 5. On-Chip Mixing for Colorimetric Quantitation of Salicylic Acid in Agar Microfluidic Channels: An Undergraduate Laboratory Experiment	97
5.1	Introduction.....	97
5.2	Experimental Overview	98
5.2.1	Fabrication of Microfluidics Chips.....	99
5.2.2	Characterization of Flow Regimes.....	100
5.2.3	On-chip Detection of Salicylate	100
5.2.4	Hazards	100
5.3	Results and Discussion	101
5.3.1	Chip Fabrication	101
5.3.2	Characterization of chip: The Reynolds's Number	102
5.3.2	On-chip detection	105
5.3.2	Student Responses	107
5.4	Conclusions.....	108
5.5	References	109
5.6	Forms	111
5.6.1	Pre-lab protocol provided to students.....	111
5.6.2	Pre-lab Questionnaire.....	119

5.6.3 Post-lab Questionnaire	120
Chapter 6. Conclusions and Future Outlook	121
6.1 Summary of Results	121
6.2 Future Work and Development	122
6.2.1 Expanding the Utility of PTR/niECD to Larger Ions	122
6.2.2 Further Interrogation of RNA Conformations in the Gas Phase.....	123
6.2.3 Negative-Ion Mode RNA-Centric Mass Spectrometry for Revealing Interaction Sites within RNA-Protein Complexes	124
6.3 References	125

List of Figures

Figure 1.1. (A) Watson-Crick base pairing. (B) Hoogsteen base pairing.....	2
Figure 1.2. Schematic view of RNA folding beginning with an unstructured species, to a structured secondary fold, which includes a series of stem loops and junctions. Further folding results in a detailed tertiary structure, consisting of various interactions. PDB ID: 1EHZ18; crystal structure of yeast phenylalanine tRNA at 1.93 Å resolution	3
Figure 1.3. Schematic representation of possible mechanisms for formation of gaseous ions in ESI: (A) IEM, (B) CRM, and (C) CEM. PDB ID: 1A3M; A-Site of 16S rRNA NMR structure.....	6
Figure 1.4. Schematic diagram of a SolariX ESI-Q-7-T FT-ICR (Bruker Daltonics) retrofitted with CO ₂ IR laser	7
Figure 1.5. McLuckey nomenclature for RNA fragment ions in tandem mass spectrometry.....	13
Figure 1.6. Schematic diagram of a Synapt nESI-Q-TWIMS Mass Spectrometer (Waters Corporation).....	17
Figure 2.1. Representative niEC(D) spectra of the homopolymers (a) rA ₆ and (b) rU ₆	37
Figure 2.2. niECD of singly deprotonated (a) rAUUUUU, (b) rUUAUUU, and (c) rUUUUUA. Precursor anions were irradiated with 4.2–4.5 eV electrons for 5 seconds	39
Figure 2.3. niEC(D) efficiency as a function of ECD cathode bias for the homopolymers (a) rA ₆ , (b) rG ₆ , (c) rC ₆ , and (d) rU ₆ . Data obtained on an Apex Q FT-ICR instrument (Bruker Daltonics, Billerica, MA).....	43
Figure 2.4. (a) Comparison of electron energies for which maximum electron capture efficiency was observed for rA ₆ , rG ₆ , rC ₆ , and rU ₆ . (b) niEC(D), electron capture, and fragmentation efficiencies calculated for each RNA oligonucleotide. Error bars correspond to half of the FWHM of the total energy distribution	44
Figure 2.5. Negative-ion mode electrospray mass spectrum of rGCAUAC.....	45
Figure 2.6. (a) niECD spectrum of doubly deprotonated rGCAUAC, 6.0 V cathode bias for 5 seconds, (b) PTR of doubly deprotonated rGCAUC, (c) PTR-niECD of in-cell isolated singly deprotonated rGCAUAC	46
Figure 2.7. Negative-ion mode ESI mass spectrum of an 11-mer RNA oligonucleotide, rUAACUAUGACG	47

Figure 2.8. (a) niECD spectrum of a triply deprotonated 11-mer, 6.0 V cathode bias for 5 seconds, (b) PTR of the triply deprotonated 11-mer, (c) PTR-niECD of in-cell isolated doubly deprotonated 11-mer	48
Figure 3.1. nESI mass spectra of a 27-mer A-site RNA construct as function of NH ₄ OAc concentration: (a) 10 mM, (b) 20 mM, (c) 50 mM, (d) 75 mM and (e) 100 mM	59
Figure 3.2. nESI mass spectra of a 27-mer A-site RNA construct as function of MeOH content (vol/vol): (a) 0%, (b) 10%, (c) 20%, (d) 30%, (e) 40%, and (f) 50%.....	61
Figure 3.3. Circular dichroism spectra of the A-site RNA construct in different concentrations of MeOH; 0% (green), 10% (red), 30% (blue), and 50% (purple)	62
Figure 3.4. Arrival time distributions of A-site RNA's charge states; 5- charge state (black line), 6- charge state (red line), 7- charge state (blue line) and 8- charge state (green line) plotted as a function of MeOH content: (a) 0%, (b) 10%, (c) 20%, (d) 30%, (e) 40%, and (f) 50%	63
Figure 3.5. Replica-exchange molecular dynamics structures of different RNA hairpin charge states; 5- charge state (blue), 6- charge state (red), 7- charge state (green), 8- charge state (purple), and 9- charge state (teal). Structures are sorted by calculated CCS (from IMoS software) and plotted as a function of CHARMM energy. Experimental calibrated CCSs (from TWIMS) are also plotted. Error bars are the least square analysis from triplicate experimentally measured CCS values.....	65
Figure 3.6. Computationally modeled structures sorted by CHARMM energy as a function of the percent CCS difference from the mean experimentally determined CCS values; (a) 5- charge state, (b) 6- charge state, (c) 7- charge state, (d) 8- charge state, and (e) 9- charge state	66
Figure 3.7. (Left) 1,000 computationally generated structures of the 7- charge state of the model A-site RNA. The structures are clustered (9 total clusters) based on RMSD of the RNA structure. (Middle) representative structure from the lowest energy cluster (pink data points). (Right) NMR derived structure, PDB ID: 1A3M	67
Figure 3.8. (Top) Aminoglycoside ligands; (a) paromomycin, (b) kanamycin B (c) apramycin and (d) ribostamycin. (Bottom Left) 16S sequence, (Right) 16* sequence...	69
Figure 3.9. Mass spectra of 16S/16S* - paromomycin complexes plotted as a function of MeOH content	70
Figure 3.10. 16S (blue diamonds) and 16S* (red squares) / aminoglycoside complex KD values as a function of MeOH content; (a) paromomycin, (b) kanamycin B, (c) apramycin, and (d) ribostamycin. Error bars are the result of triplicate measurements .	70
Figure 3.11. Mass spectra of 16S/16S* - paromomycin complexes plotted as a function of solution pH	72
Figure 3.12. 16S (blue diamonds) and 16S* (red squares) / aminoglycoside complex KD values as a function of solution pH; (a) paromomycin, (b) kanamycin B, (c) apramycin, and (d) ribostamycin. Error bars are the result of triplicate measurements .	73

Figure 4.1. (a) ESI mass spectrum of a non-covalent RNA-substance P complex in negative-ion mode (pH 7); (b) positive-ion mode (pH 7). The percent RNA-peptide complex is significantly increased in negative ion-mode at neutral pH 85

Figure 4.2. (a) CID (15 V) MS/MS of RNA-angiotensin I complex. Extensive fragmentation of the RNA moiety is observed with very limited fragmentation of the peptide; (b) niEC(D) spectrum of the doubly deprotonated RNA-angiotensin I complex. Electron capture is observed but no fragments are generated 86

Figure 4.3. (a) CID (20 V) MS/MS spectrum of RNA-substance P complex. Extensive fragmentation of the RNA moiety is observed (blue) with no fragmentation of the peptide; (b) AI-niECD spectrum of the doubly deprotonated RNA-substance P complex 87

Figure 4.4. Total ion chromatogram of trypsin digested PRORP1 protein. About 90% sequence coverage was obtained following LC/MS of trypsin-digested protein (Inset) The crystal structure of proteinaceous RNase P 1 (PRORP1) from *A. thaliana*. PDB ID: 4G26..... 88

Figure 4.5. Extracted ion chromatograms for (a) rGCAUAC, (b) the synthetic crosslink, (c) ACTH 1-10, (d) angiotensin I, (e) 4-azidophenylalanine-containing PRORP1 tryptic peptide, (f) CCK, and (g) oxidized insulin chain A before (black) and after (red) IR irradiation for 150 ms at 6.25 W 89

Figure 4.6. Mass spectrum of RNA hexamer, rGCAUAC, before (black) and after (red) IR irradiation 90

Figure 4.7. Mass spectrum of RNA-PRORP1 peptide crosslink before (black) and after (red) IR irradiation. Peaks that are not annotated do not correspond to any sequence informative ions from the heteroconjugate 90

Figure 4.8. Mass spectrum of ACTH 1-10 peptide before (black) and after (red) IR irradiation..... 91

Figure 4.9. Mass spectrum of angiotensin I peptide before (black) and after (red) IR irradiation..... 91

Figure 4.10. Mass spectrum of CCK peptide before (black) and after (red) IR irradiation 91

Figure 4.11. Mass spectrum of oxidized insulin chain A peptide before (black) and after (red) IR irradiation..... 92

Figure 4.12. Mass spectrum of 4-azidophenylalanine-containing PRORP1 peptide before (black) and after (red) IR irradiation 93

Figure 5.1. Outline of channel geometries that students will construct: “Y” channel (A), “90°” channel (B), and “Zigzag” channel. Figures are not drawn to scale 99

Figure 5.2. Photo of experimental setup..... 102

Figure 5.3. Representative photos taken from 90° turning channels on student-constructed chips; (a) Pure water; the flow remains laminar with the red and blue dye flowing side by side. (b) 50/50 water/methanol; little mixing is observed. (c) Pure methanol; mixing is observed. Photos were taken of the same region of the channel. The width of the channel is 0.5 cm 103

Figure 5.4. Photographs of student-constructed microfluidic devices. Channels a-c have colored water flowing through the channels. Despite varying the channel geometry, the flow remains laminar. Channels d-f contain 50% methanol dye solutions. In these cases, mixing is observed. However, despite this fluid composition, very little to no mixing was observed in the “Y” channels (d) 104

Figure 5.5. Measured kinematic viscosity as a function of methanol composition at room temperature 105

Figure 5.6. Iron (III)–salicylate solutions at increasing concentrations of salicylate. The width of the channel is 0.5 cm 106

Figure 5.7. Representative calibration curves from student-constructed microfluidic device (top) and from visible spectroscopy (bottom). Very good correlation is observed between the RGB analysis and salicylate concentration with an R2 value of 0.96, which is only slightly lower than for the absorbance vs. salicylate curve 107

Figure 5.8. Results of student surveys: We surveyed students across two sections (N = 47) before and after they completed the microfluidics experiment. Students replied to a series of statements with values that ranged from 1 (strongly disagree) to 5 (strongly agree) 108

Figure 5.9. Pre-lab protocol provided to students 111

Figure 6.1. ESI-PTR mass spectra of a 27-mer RNA oligonucleotide anion. Upon PTR of the quadrupole-isolated, quadruply deprotonated species, triply and doubly deprotonated species at high m/z values are observed. PTR reagent was accumulated for 500 ms. Data collected on a solariX-XR FT-ICR mass spectrometer, at Bruker Daltonics (Billerica, MA), equipped with an ETD module for PTR and a ParaCell3 for mass analysis. * denotes noise peaks 123

Figure 6.2. Proposed workflows for the study of the tRNA-PRORP1 complex; (top) conventional workflow identifying crosslinking sites at the residue level on peptides whereas (bottom) proposes an RNA-centric approach for crosslink identification 125

List of Tables

Table 3.1. Calibrated CCS values for charge states 5- to 9- as function of NH ₄ OAc concentration in solution.....	60
Table 3.2. KD values of aminoglycosides bound to 16S A-site construct as a function of MeOH content	71
Table 3.3. KD values of aminoglycosides bound to 16s A-site construct as a function of pH.....	73
Table 5.1. R _e as a function of methanol composition and channel geometry	105

List of Schemes

- Scheme 1.1.** Fragmentation route for methods involving vibrational activation, e.g. CID and IRMPD. The multiple collisions or absorbed photons brings the anion into an excited state, later resulting in ion fragmentation 12
- Scheme 1.2.** Fragmentation route for ECD, “low” electron energy corresponds to energy levels < 1 eV. Upon electron capture by a cation, a charged reduced radical species is produced which later fragments via a radically driven process 14
- Scheme 1.3.** Fragmentation route for EDD, “high” electron energy corresponds to energy levels > 18 eV. An electron is ejected from the anion resulting in a charge reduced radical and 2 electrons. The metastable radical later fragments via a radically driven process 15
- Scheme 1.4.** Fragmentation route for niECD. Upon electron capture by an anion, a charged increased radical species is produced which later fragments via a radically driven process 15
- Scheme 4.1.** Schematic of the click chemistry reaction for formation of a model RNA-peptide crosslink. 4-azidophenylalanine reacts with 5EdU via a copper mediated reaction to form a triazole linkage 89

List of Abbreviations

5-BrU	5-Bromouridine
CCS	Collision Cross Section
CI	Chemical Ionization
CID	Collision Induced Dissociation
CRM	Charged Residue Model
DC	Direct Current
DIA	Data-independent Acquisition
DNA	Deoxyribonucleic Acid
ECD	Electron Capture Dissociation
EDD	Electron Detachment Dissociation
EHSS	Exact Hard Sphere Scattering
EID	Electron Induced Dissociation
ESI	Electrospray Ionization
ETD	Electron Transfer Dissociation
FA	Formic Acid
FID	Free Induction Decay
FRET	Förster Resonance Energy Transfer
FT-ICR	Fourier Transform-Ion Cyclotron Resonance
i.d.	Inner Diameter
IEM	Ion Ejection Model
IRMPD	Infrared Multiphoton Dissociation
IMAC	Immobilized Metal Affinity Chromatography
K_D	Dissociation Constant
MD	Molecular Dynamics

mRNA	Messenger RNA
MS	Mass Spectrometry
MS/MS	Tandem Mass Spectrometry
<i>m/z</i>	mass-to-charge
ncRNA	Non-coding RNA
nESI	Nanoelectrospray Ionization
niECD	Negative-Ion Electron Capture Dissociation
PA	Projection Approximation
PAR-CLIP	Photoactivateable Ribonucleoside Enhanced Crosslinking and Immunoprecipitation
PDMS	Polydimethylsiloxane
PRORP	Proteinaceous RNase P
REMD	Replica-Exchange Molecular Dynamics
RF	Radio Frequency
RNA	Ribonucleic Acid
RNase	Ribonuclease
RNP	Ribonucleoproteins
rRNA	Ribosomal RNA
TEA	Triethylamine
TM	Trajectory Method
tRNA	Transfer RNA
TWIMS	Traveling-Wave Ion Mobility Spectrometry
UVPD	Ultraviolet Photodissociation

Abstract

Chair: Kristina I. Håkansson

Ribonucleic acids (RNAs) form complexes with deoxyribonucleic acids, proteins, other RNAs, and smaller ligands. Detailed knowledge of RNA interaction sites provides a basis for understanding functions. With limited analytical techniques available to obtain deeper understanding of RNA structure, negative ion mode mass spectrometry (MS) has the potential to significantly expand RNA primary, secondary, tertiary, and quaternary structure information. This dissertation presents novel MS methods for characterizing RNAs and their complexes.

Negative-ion electron capture dissociation (niECD) involves ~3.5-6.5 eV electron irradiation to yield charge-increased intermediates that further undergo radical-driven fragmentation. The proposed niECD mechanism involves gas-phase zwitterionic structures in which nucleobases are protonated and the phosphate backbone is deprotonated. We found that electron-capture efficiency is higher for purine nucleobases compared with pyrimidines and that purine radicals are more stable, presumably because purines have higher proton affinities and can form intramolecular hydrogen bonds. niECD efficiency decreases with increased charge state due to Coulomb repulsion. We show that gas-phase proton-transfer reactions can be combined with niECD for improved performance.

Electrospray ionization (ESI) of a model RNA hairpin from native-like (10 mM ammonium acetate) and methanol-containing (up to 50%) solvents resulted in identical charge state distributions, suggesting a minor methanol effect on overall conformation. Experimentally determined collision cross sections (CCSs) for the 5- and 6- charge states of this RNA are smaller (789 \AA^2 and 830 \AA^2 , respectively) than those predicted from the NMR structure. Replica-exchange molecular dynamics showed that these charge states adopt globular collapsed structures due to self-solvation whereas the 7-charge state showed hairpin retention. Higher charge states showed extended structures (higher CCSs). Ligand (e.g., paromomycin) binding assays at varied

methanol content resulted in strongest binding at 0% methanol (64 ± 6 nM K_D). However the K_D remained within one standard deviation up to 50% methanol, suggesting that the binding site is mainly unperturbed in methanol. Assays at varied pHs showed strongest binding at neutral pH. Overall, these data suggest that moderate methanol concentrations, which facilitate ESI, can be tolerated in native RNA MS.

Crosslinking techniques coupled with MS provide an alternative tool for identifying RNA interaction sites. We show that collisional activation can provide full sequence coverage of the RNA moiety within non-covalent RNA-peptide complexes; however complexes are disrupted, resulting in loss of site-specific information. By contrast, niECD, in combination with infrared multiphoton dissociation provided sufficient sequence coverage while retaining non-covalent interactions. We also show that IR irradiation at 10.6 μm selectively dissociates RNA-peptide crosslinked species within a peptide mixture due to resonance absorption by phosphate groups, thus allowing identification of such species.

Microfluidics is a highly efficient technology for biological analysis. Microfluidic-type approaches, including nano-ESI and nano-LC, coupled with MS provide several advantages, e.g., limited sample consumption and enhanced sensitivity. In order to disseminate microfluidic principles, we developed a 2-week (8 hour) laboratory experiment for an undergraduate analytical chemistry course. Students are introduced to soft lithography concepts by designing/characterizing their own agar-based microfluidic chips. They learn about fluid dynamics by approaching the challenge of mixing in microfluidic channels. By varying solvent viscosity and channel geometries, terms that govern the Reynolds number, students achieve mixing. The optimal chip geometry/solvent condition is used to quantify salicylic acid-iron (III) complex by colorimetric analysis.

Overall, this dissertation describes the utility of MS (and its associated tools) for the study of RNA, RNA-small molecule, and RNA-protein complexes.

Chapter 1

Introduction

With the discovery of the double helix structure of deoxyribonucleic acid(s) (DNAs), by James Watson and Francis Crick in the early 1950s, came along what is now known as the central dogma of molecular biology.¹⁻³ This central dogma states that DNA is transcribed to ribonucleic acids (RNAs), which are later translated to proteins, detailing the transfer of genetic information from the genome to the proteome. DNA carries the genetic code and contains thousands of genes, which determine the sequences of proteins. A protein sequence ultimately dictates its structure and function, and directs cellular processes. Proteins are synthesized based on unique transfer (t)RNA sequence and code carried by messenger (m)RNA. Protein synthesis takes place in ribosomes, which contain protein and ribosomal (r)RNA subunits. The proteome, constituting the workhorse of the cell, has been extensively studied in the fields of chemistry, biochemistry, biology, biophysics, etc. Furthermore, the structure and function of RNAs which code for proteins have been extensively studied.⁴ However, the roles of non-coding (nc)RNAs are understudied and often underappreciated.

ncRNAs were discovered as a new class of RNAs through the remarkable technological feat of The Human Genome Project.⁵⁻⁸ In fact, only about 1-3% of our genome actually codes for functional proteins. Every day, new functions for these ncRNAs are being discovered. RNAs and their complexes (with other nucleic acids, proteins, and small molecules, etc.) play vital roles in cell biology, drug discovery, and have been shown to have catalytic activity, which has been the major driving force of the RNA world hypothesis (e.g., ribozymes).⁹ To perform these diverse functions, RNA molecules adopt unique three-dimensional structures.¹⁰⁻¹⁶ It is of utmost importance, therefore, to develop analytical methods to study the structures of RNAs and their complexes to gain more insight into function.

1.1 RNA Structure and Function

RNAs are macromolecular polymers made up of nucleotides. Nucleotides are composed of a heterocyclic nitrogenous base, a ribose sugar, and a phosphate group. RNAs contain two purine bases, adenine (A) and guanine (G), and two pyrimidine bases: cytosine (C) and uracil (U). Nucleotides are connected via the 3' hydroxyl of one nucleotide to the 5' hydroxyl of the adjacent nucleotide, thus forming the sequence of RNAs. One notable example of the importance of RNA sequence is in mRNA. The coding region of mRNA must be unfolded for genetic information to be translated.^{11,17} Secondary structure is dominated by non-covalent interactions in the form of complementary Watson-Crick base pairing (Figure 1.1). Other non-canonical base pairing (e.g., Hoogsteen base pairing) forms various secondary structures, such as helices, hairpin stem-loops, hammerhead, and pseudoknots, just to name a few (Figure 1.2).

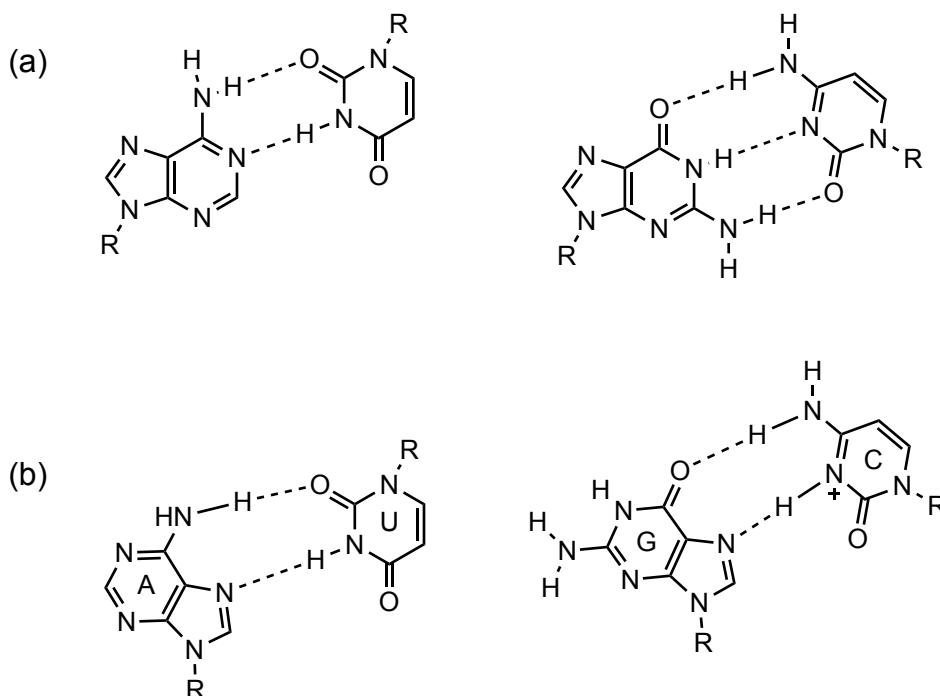


Figure 1.1: (a) Watson-Crick base pairing. (b) Hoogsteen base pairing.

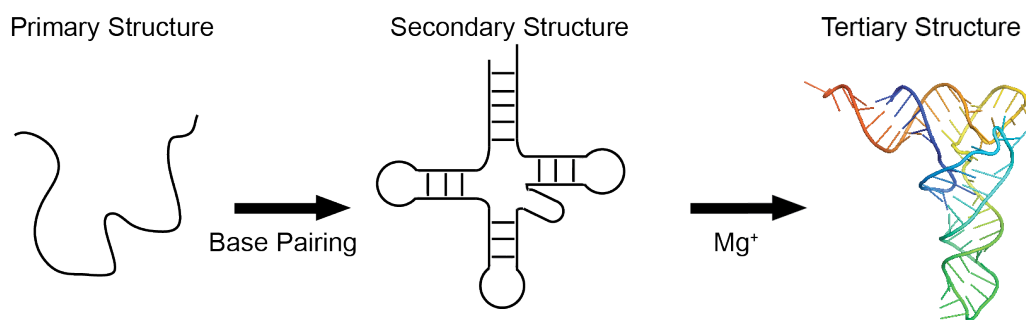


Figure 1.2: Schematic view of RNA folding beginning with an unstructured species, to a structured secondary fold, which includes a series of stem loops and junctions. Further folding results in a detailed tertiary structure, consisting of various interactions. PDB ID: 1EHZ¹⁸; crystal structure of yeast phenylalanine tRNA at 1.93 Å resolution.

RNA can further adopt a variety of complex tertiary structures. Tertiary structures are formed due to the presence of high rotational freedom along the backbone and its non-base paired regions. Thus, tertiary structures involve the formation of base triplets and base backbone interactions, such as those found in tRNA. In order for RNAs to perform their biological functions, they form complexes with DNAs, proteins, other RNA molecules, and smaller ligands. Notable biological functions of RNA complexes include pre-transfer RNA (pre-tRNA) processing and major roles in protein synthesis (rRNA).

Despite the apparent simplicity of RNA, being composed of only four main building blocks, RNAs have the propensity to fold into more than one secondary and tertiary stable state. Non-native folded states can be as stable as their native state counterparts, trapping the RNA in a non-active state. RNA and other molecules often interact in a transient manner and, for this reason, the study of RNA structure present many analytical challenges. Furthermore, detailed knowledge of interaction sites within RNA complexes provides a profound basis for understanding their functions. Many biophysical techniques have been employed to study interaction sites of RNA complexes, including nuclear magnetic resonance (NMR) spectroscopy and X-ray crystallography. Not only does NMR provide high-resolution structures but it can also provide dynamic information whereas many other methods cannot.¹⁹⁻²² Demands for high spectral resolution, however, drastically increases as the size of the molecule increases.²³ X-ray crystallography can provide up to atomic resolution structures but the

quality of crystallography data strongly depends on the quality of the grown crystal and because, RNAs are very dynamic systems, the ability to solve the phase problem becomes increasingly difficult when a crystal is obtained.²⁴ Both NMR spectroscopy and X-ray crystallography also suffer from their high sample requirement. FRET (Förster resonance energy transfer) spectroscopy is a powerful technique for studying molecular interactions inside living cells. FRET efficiency is dependent on the distance between the FRET donor and acceptor and is highest when both donor and acceptor are positioned within the Förster radius, thus presenting a distance constraint limiting the elucidation of overall structure.^{25,26} Mass spectrometry (MS), on the other hand, is a very powerful and versatile technique used to study a plethora of chemical and biological systems. Applications of MS include the analysis of aerosols, small molecules, nucleic acids, peptides and proteins, and carbohydrates. MS, a label-free method, provides complementary information to many chemical and biophysical techniques as well as several technological advantages, which include high-throughput analysis, increased selectivity, detection limits, and limited sample consumption. MS has emerged as a powerful technique for studying RNA structure, and interactions with other biologically relevant molecules.²⁷⁻³⁰

1.2 Mass Spectrometry

1.2.1 Ion Generation

Electrospray ionization (ESI) is a soft ionization technique used for the formation of gaseous ions. The advent of ESI has allowed for large macromolecules to be introduced into the gas phase relatively or entirely intact.³¹⁻³⁴ ESI produces multiply charged ions, which, even for large macromolecules, can be analyzed with a mass analyzer of limited mass-to-charge (m/z) range. ESI works by placing a capillary at high voltage a few centimeters away from the inlet of a mass spectrometer, serving as a counter electrode, and forcing a solution with a desired analyte through this capillary. The electric field generated by the high voltage results in charge accumulation at the end of the capillary and, as a result, pulls the meniscus of the liquid into a Taylor cone. The Taylor cone is

pulled into a jet, and further into charged aerosolized droplets. The origin of gas phase ions from these charged droplets is still an ongoing area of research but the three widely accepted mechanisms are the charge residue mechanism (CRM)³⁵, the ion evaporation mechanism (IEM),³⁶ and, more recently, the chain ejection mechanism (CEM).³⁷ In all mechanisms, fission of the charged droplets occurs when they reach the Rayleigh limit (Figure 1.3), given by the Rayleigh Equation 1.1³⁸:

$$Z_R = 4\pi(\epsilon_0\gamma R^3)^{1/2} \quad \text{(Equation 1.1)}$$

in which Z_R is the charge on the droplet, ϵ is the permittivity of the surrounding medium, γ is the surface tension of the solvent and R is the radius of the droplet.

Large globular molecules (e.g., biomolecules) are believed to follow the CRM. In CRM, many stages of droplet fission occurs until evaporation of solvent from ultimate droplets leads to ionized versions of their contents, i.e., single analyte molecules. By contrast, in the IEM, droplet charge density is depleted by ion evaporation from the surface of the droplets. The IEM mechanism has been proposed for low-molecular weight analytes. Finally, the CEM has been proposed for unfolded polymers. As polymers become unfolded, they become more hydrophobic, thus making it unfavorable for the polymer to remain in the droplet. As a consequence, the polymer migrates to the surface of the droplet and is later ejected into the gas phase.

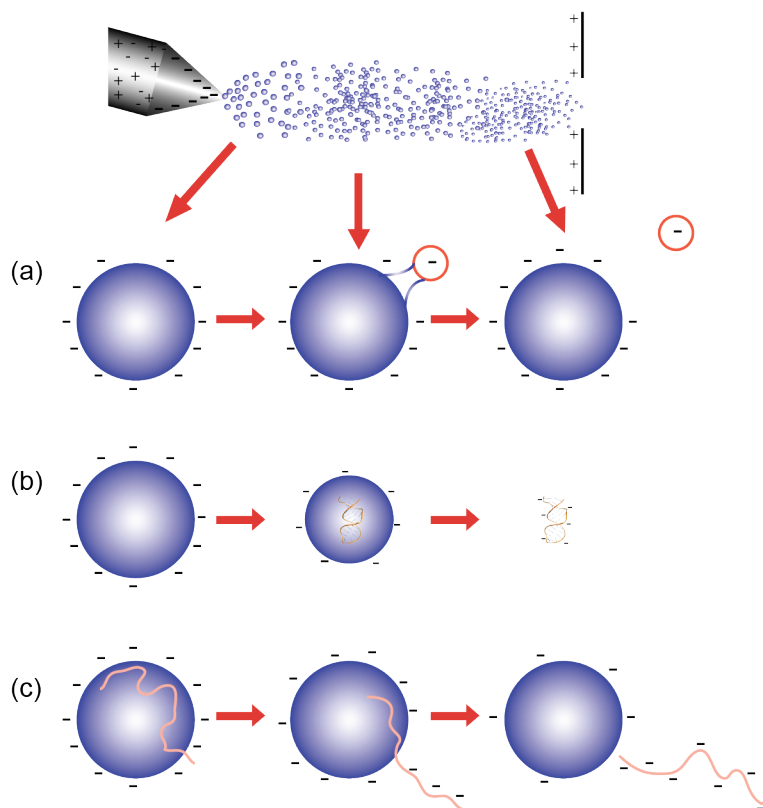


Figure 1.3: Schematic representation of possible mechanisms for formation of gaseous ions in ESI: (a) IEM, (b) CRM, and (c) CEM.

1.2.1 Fourier Transform Ion Cyclotron Resonance Mass Spectrometry (FT-ICR MS)

FT-ICR MS provides unmatched resolution and mass accuracy compared with other mass analyzers because the principle of analysis is independent of the kinetic energy and instead measures the cyclotron frequency of an ion in a homogenous magnetic field. From the first introduction of FT-ICR by Comisarow and Marshall in 1974, the technology has grown immensely pushing the boundaries of high mass resolution and mass accuracy.⁴⁰⁻⁴⁶ The main components of the FT-ICR instruments used for this dissertation include an electrospray ionization source and source optics, a quadrupole (Q) interface, ion transfer optics, and the ICR Infinity Cell.

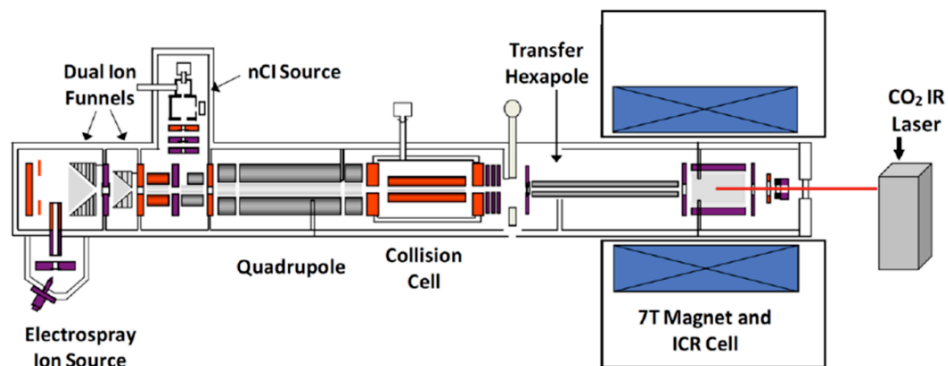


Figure 1.4: Schematic diagram of a Solarix ESI-Q-7-T FT-ICR (Bruker Daltonics) retrofitted with CO₂ IR laser.

A sample is introduced into the Apollo II ionization source where the sample is subjected to the electrospray process by means of a strong electric field between the ESI capillary and the spray shield. A nebulizer gas, N₂, helps aerosolize the sample solution. The nebulizing gas also helps to direct the spray toward the mass spectrometer. A heated drying gas, also N₂, flows in the opposite direction of the stream of droplets entering the spray chamber. The heated gas aids in volatilization and desolvation, which in turn aids in the overall ionization of the sample. It also helps carry away any uncharged material. The nebulizing gas also helps guide the sample aerosol past the spray shield at temperatures ranging from 100°C to 400°C. There is an electric field between the spray capillary, which is at ground potential for safety reasons, and a negatively (or positively, if operating in negative-ion mode) biased metal-coated glass capillary. The off-axis geometry of the Apollo II source helps prevent neutrals from clogging and corroding the glass capillary.

Ions generated by the electrospray event enter the first vacuum stage of the mass spectrometer through the glass capillary. Exiting the capillary, ions are deflected into the first ion funnel with assistance of a deflector plate. The entrance of the ion funnel is biased with a voltage. An electric field is formed when this voltage is dropped over the length of the ion funnel down to its last element at the first skimmer, thus directing ions into the instrument. An RF field is also applied to the first ion funnel and, together with collisions, helps focus ions through the aperture of the skimmer. After passing through the first skimmer, ions enter a second funnel with another voltage

leading to the second skimmer. The dual ion funnel/skimmer system improves overall ion transmission efficiency through ESI-MS interfaces.

The ion funnel consists of a series of cylindrical ring electrodes (equally spaced) of decreasing inner diameter, enabling the spatially dispersed ion cloud entering the ion funnel to be effectively focused to a smaller radial size for efficient ion transmission.⁴⁷ The ion funnel technology has been incorporated in other areas of mass spectrometry, including the stacked ring ion guides used in traveling wave ion mobility instruments (discussed later).^{48,49}

After passing through the second skimmer, ions enter the source octopole.⁵⁰ This octopole consists of eight cylindrical, parallel rods with an RF voltage applied on the rods. The polarity of the RF-voltage is opposite from one adjacent rod to another. The applied RF voltage confines ions radially, whereas collisions with neutral gas molecules cool the ions. The octopole serves as an ion guide, it focuses ions and transports them efficiently from a high-pressure region to the high vacuum region of the mass spectrometer. The basic principles of the octopole are discussed in the quadrupole section below. The SolariX instrument is equipped with a split octopole to introduce ions from both the electrospray source and a chemical ionization source.

The quadrupole mass filter uses the stability of the trajectories in oscillating electric fields to filter ions based on their m/z ratios. A quadrupole consists of four cylindrical, parallel metal rods. Two of the opposite rods have an applied potential of $U + V\cos(\omega t)$ and the other two rods having an applied potential of $-[U + V\cos(\omega t)]$, in which U is the resolving DC potential and $V\cos(\omega t)$ is the applied RF potential. The ions travel under the influence of the RF field superimposed on the DC field. Ions are accelerated radially by the electric field in the space between the rods (x and y direction) and maintain their velocity along the z axis. Ion trajectories will be stable if the values of x and y never reaches the value of r_0 (ions do not hit the rods). The motion of ions within a quadrupole is governed by the Mathieu equations⁵⁰:

$$q_u = \frac{4eV}{mr_0^2\Omega^2} \quad a_u = \frac{8eU}{mr_0^2\Omega^2} \quad (\text{Equation 1.2})$$

The Mathieu equations are reduced to two parameters, a and q , that describe ion stability within the quadrupole. U is the resolving DC potential and V is the zero-to-peak amplitude of the applied RF voltage, m is the mass of the ion, r_0 is the inscribed radius of the quadrupole, e is the elementary charge multiplied by the number of charges on the ion and Ω is the RF drive frequency (equal to $2\pi\nu$ and is constant for a given quadrupole). An important element of the above equations is the relationship between a and U and q and V . Parameter a is proportional to the applied DC voltage, whereas parameter q is proportional to the RF amplitude. Both are inversely proportional to m/z ratio. An a, q diagram is used to represent the regions of ion stability. Quadrupoles can be operated in RF/DC mode or RF-only mode. RF/DC mode is used for ion isolation by placing ions of interest on the apex of the stability diagram and forcing all other ions to be outside of the stability area. In RF-only mode, only an RF voltage is applied to the rods ($U = 0$ V), thus all ions have an a value equal to 0. As a consequence, all ions will lie on the q axis of the stability diagram with ions of decreasing mass at increasing q values. RF-only mode allows a large mass range of ions to pass through the quadrupole into the collision cell, where ions can be stored.

The collision cell is a hexapole ion guide operating in RF-only mode. The principles of a hexapole are similar to those applying to the quadrupole (see above). A hexapole consists of six parallel rods placed symmetrically to form a long tube around the transfer axis. The rods are connected in pairs of three. An RF voltage is applied to the rods, with a polarity inverted from one rod to the next. The effective potential trap stores, and focuses the trajectories of the ions in two dimensions along the axis of the guide to the analyzer cell. A DC pole bias is added to the rods and pulsed between two values; the bias is set to one value when the ions enter the cell and then pulsed to a higher value to extract ions towards the ICR cell. The resulting difference between the DC on the source octopole and the DC on the hexapole collision cell while ions are entering the cell is the collision energy. This potential difference causes ions to collide with background neutral gases as they are accelerated into the cell. The collision cell is at an elevated pressure of $\sim 1 \times 10^{-3}$ mbar, typically Argon. Conditions are changed (to a larger potential difference) to induce fragmentation of mass-selected precursor ions via inelastic collisions. Product ions are trapped by low energy collisions with background

neutrals. Finally, ions are transferred to the analyzer cell by pulsing the DC bias voltage to an extraction value. Ion storage in the collision cell hexapole improves the duty cycle of the MS experiment. The SolariX instrument uses an RF-only hexapole to focus ions along the magnetic field axis into the ICR cell, allowing for high transmission efficiency.

The magnetic and electric fields that are present govern ion motion in an ICR cell. The magnetic field acts on the component of the velocity of an ion that is perpendicular to the magnetic field axis (Equation 1.3).^{40,41}

$$F = qv \otimes B \quad (\text{Equation 1.3})$$

The ion experiences a force (Lorentz force) that is perpendicular to both the direction of the magnetic field and to the velocity of the ion. The Lorentz force causes the ion motion to travel in a circular orbit perpendicular to the magnetic field (cyclotron motion). The cyclotron frequency is determined by magnetic field strength, the charge on an ion, and its mass (Equation 5).

$$f_c = \frac{qB}{2\pi m} \quad (\text{Equation 1.4})$$

The cyclotron frequency is constant for an ion of given m/z and the radius of the cyclotron orbit depends on the kinetic energy of the ion.

The Infinity Cell (FT-ICR analyzer; Bruker Daltonics, Billerica, MA) is composed of a pair of trapping, excitation, and detection plates. The trapping plates are responsible for axially confining ions by applying DC potentials to the trapping electrodes. Trapping motion is an oscillating motion in which the ions oscillate along the z-axis due to the force experienced from the electric field present. A typical FT-ICR MS experiment consists of a series of events; the quench, the ionization, excitation, and detection events. During the quench event, the analyzer cell is emptied of any ions that may be present from the previous experiment. Applying a positive voltage to one trapping plate and also applying a negative voltage to the other trapping plate achieves ejection of unwanted ions. Under such conditions, ions are ejected axially from the cell in ~25 ms. Ions to be analyzed are then injected into the ICR cell from an external source and trapped in the ICR cell in the subsequent experimental event. The ions are

confined and detected in an ICR cell of a closed cylindrical geometry consisting of pairs of trapping, excitation, and detection plates. The cell is located in the center of a superconducting magnet that provides a magnetic field of high homogeneity to radially confine ions. The radially confined ions, however, due to the magnetic field can easily escape along the z axis of the cylinder. To prevent this, a small voltage (0.5-1.5V) of the same polarity as the trapped ions is applied to the trapping plates, providing axial confinement by creating a potential barrier that retains ions within the cell. Ions undergo harmonic oscillation between the trapping plates along the magnetic field axis, termed trapping motion.

The radius of the cyclotron orbit of an ion is usually small compared to the geometry of the cell. To detect ions, they are excited to a higher cyclotron radius by applying a sinusoidal voltage to the pair of opposite excitation plates. The ions spiral to a larger orbit when their cyclotron frequency is in resonance with the applied RF field. All ions of the same m/z are excited into coherence. That is, ions of the same m/z undergo cyclotron motion as a packet. A wide m/z range of ions can be detected by applying a frequency sweep, or RF chirp, that causes all ions in a given frequency range to be excited to large cyclotron orbits. After ions are excited, their cyclotron radii are close to the detection plates. The movements of the ions as they pass the detection plates induce a local electric field change on the surface of the detection electrodes. The image current as ions pass from one electrode to another is recorded. This time domain signal is converted to a frequency domain signal by applying fast Fourier Transform algorithm. The frequency domain spectrum is then converted to a conventional mass spectrum by applying a calibration function based on equation 1.4.

A major advantage of FT-ICR is the high resolution and high mass accuracy. The high homogeneity of the applied magnetic field, as well as the fact that ion detection is independent of kinetic energy, allows an ion to be detected with unsurpassed high resolution. Additionally, the principle of detection is the cyclotron frequency of an ion. Because frequency can be measured very precisely and accurately, FT-ICR provides high mass precision and accuracy. Another advantage of FT-ICR is the tandem mass spectrometry (MS/MS) versatility. Tandem mass spectrometry is a general method involving two or more stages of mass analysis. MS/MS is performed in conjunction with

a dissociation process or a chemical reaction that causes the mass or charge of an ion to change. MS/MS experiments are used for elucidation of biomolecular structures, determination of fragmentation mechanisms, observation of ion molecule reactions, and thermochemical data determination. Ion activation techniques used in MS/MS experiments include collision-induced dissociation (CID)⁵¹⁻⁵³, infrared multiphoton dissociation (IRMPD)⁵⁴, ultra-violet photodissociation (UVPD)^{55,56}, electron-capture dissociation (ECD)⁵⁷⁻⁵⁹, electron transfer dissociation (ETD)⁶⁰, electron detachment dissociation (EDD)⁶¹⁻⁶³, and negative-ion electron capture dissociation (niECD)^{64,65} just to name a few.^{66,67}

1.2.2 Vibrational Activation

Of all fragmentation methods used for the structural elucidation of biomolecules, CID remains the most common. The CID process occurs in two steps (Scheme 1.1). Ions are accelerated into a cell pressurized with a background of neutral gas (e.g., Ar), where multiple ion-neutral collisions occur. A fraction of the ion translational energy from each collision is converted into internal energy. The energy is distributed throughout the ion via intramolecular vibrational-energy redistribution (IVR). If significant enough, the internal energy brings the ion to excited vibrational states close to the dissociation threshold. The second step in the CID process corresponds to the dissociation of the weakest bonds, both covalent and non-covalent, within an RNA or RNA complex. The product ions are formed through the lowest energy pathways. RNA gas-phase fragmentation occurs along the phosphate backbone (Figure 1.5), producing predominately *c* (from the 5' end) and *y*-type ions. *w* and (*a* – base)-type ions are also observed if the collision energy is high enough and at high anion charge states.^{68,69}



Scheme 1.1: Fragmentation route for methods involving vibrational activation, e.g. CID and IRMPD. The multiple collisions or absorbed photons brings the anion into an excited state, later resulting in ion fragmentation.

Other MS/MS techniques which result from electronic and vibrational activation include photodissociation (UVPD)⁵⁵ and infrared multiphoton dissociation (IRMPD), respectively.⁵⁹ UVPD and IRMPD use lasers that are directed through a window to irradiate the interior of the mass analyzer. Ions absorb one or more photons. Compared to UV photons, IR photons are much less energetic (~0.1 eV) requiring the ion to absorb multiple photons. As each photon is absorbed, the internal energy of the ion increases and is redistributed into several vibrational modes until the ion fragments, as in CID. The most commonly applied laser for IRMPD is a 10.6 μm CO₂ laser. FT-ICR platforms are best suited for IRMPD because the UHV minimizes collisional cooling of activated precursor ions. Furthermore, IRMPD can be used in conjunction with other techniques, e.g. ECD or niECD, for supplemental activation to break non-covalent interactions to improve sequence coverage.⁷⁰

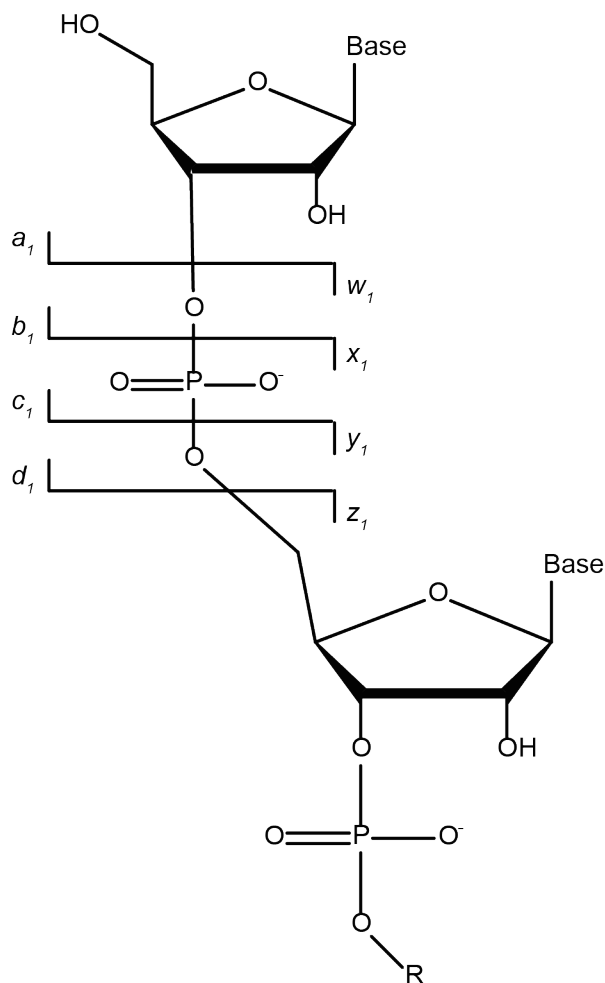
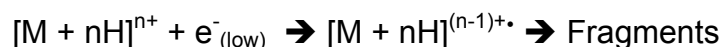


Figure 1.5: McLuckey nomenclature for RNA fragment ions in tandem mass spectrometry.⁶⁶

1.2.3 Electron-based Fragmentation

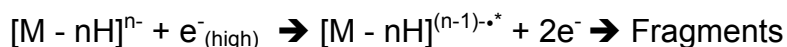
In ECD, multiply charged cations are irradiated with low-energy (~1 eV) electrons, resulting in a charged-reduced intermediate. The electron recombination energy drives the charged-reduced species to undergo rapid radical-driven dissociation producing unique, complementary sequence informative product ions (Scheme 1.2). Electron-based fragmentation techniques produce *d* and *w*-type ions for nucleic acids. The mechanism of product ion formation is currently the subject of much debate.^{67,71-73}



Scheme 1.2: Fragmentation route for ECD, “low” electron energy corresponds to energy levels < 1 eV. Upon electron capture by a cation, a charged reduced radical species is produced which later fragments via a radically driven process.

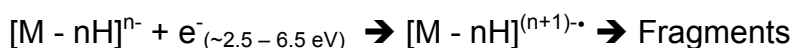
ECD can preserve labile bonds, including non-covalent interactions, and generates complementary backbone fragments compared with other MS/MS techniques such as CAD or IRMPD.⁵⁸ ECD was primarily performed in FT-ICR mass spectrometers, until recently.⁷⁴⁻⁷⁶ To implement ECD on other mass analyzers, a magnet is typically added because electrons cannot be confined long enough in a radiofrequency field (e.g., ion traps). ECD has been performed in modified ion traps; however the fragmentation efficiency is typically lower than with FT-ICR MS.^{77,78} Compared to ECD, ETD induces fragmentation of cations by transferring electrons to them via an ion-ion reaction. However, utilizing free electrons, rather than anions, as the source of electron transfer provides more precise control over their energy.⁷⁹ As a result there is access to more flexible, information rich, fragmentation data that cannot be obtained in the absence of free electrons.

ECD, however, involves positively charged precursor ions and generating multiply charged cations can be challenging for acidic analytes such as RNA. For this reason, negative-ion MS/MS techniques such as electron detachment dissociation (EDD) and recently discovered (niECD) are desired.



Scheme 1.3: Fragmentation route for EDD, “high” electron energy corresponds to energy levels > 18 eV. An electron is ejected from the anion resulting in a charge reduced radical and 2 electrons. The metastable radical later fragments via a radically driven process.

A challenge with EDD, however, is that it suffers from low fragmentation efficiency and requires high charge states that may not be amenable with RNA native-like conformations. niECD, therefore, is a promising alternative as lower charge states are favorable. In niECD, negatively-charged species are irradiated with electrons of a narrow energy range (~2.5-6.5 eV), resulting in charge-increased species that undergo structurally informative backbone fragmentation.



Scheme 1.4: Fragmentation route for niECD. Upon electron capture by an anion, a charged increased radical species is produced which later fragments via a radically driven process.

Ion-electron reactions (such as EDD and (ni)ECD) provide advantages over slow heating methods (such as negative ion CID or IRMPD) because non-covalent interactions are retained and, for niECD, more predictable fragmentation occurs for peptide analysis. Less is known about the niECD fragmentation behavior for nucleic acids. The performance of niECD is dependent on the precursor ion charge state. As charge state increases, it becomes more difficult for gas-phase anions to capture an electron due to Coulomb repulsion, thus decreasing niECD efficiency. Methods, therefore, must be developed and implemented to reduce charge states to improve niECD efficiency for electrosprayed large ions. Ion-ion reactions, such as proton transfer reaction (PTR) with tandem mass spectrometry, have been demonstrated to expand the structural characterization of proteins.⁸⁰⁻⁸⁷

1.2.3 Traveling-Wave Ion Mobility Mass Spectrometry (IM-MS)

Native mass spectrometry has been shown to be effective in preserving protein solution-phase structure into the gas phase.⁸⁸ Protein complexes and protein interaction networks have been studied extensively in this manner. Memory of the solution-phase structure has allowed mass spectrometry to accurately determine structure. Mass analysis in native mass spectrometry is achieved from a “native like” environment, in the absence of denaturing conditions such as high organic solvent content or highly basic or acidic solvents, conventionally included to optimize signal rather than to preserve structure. Ammonium acetate is a common buffer in native mass spectrometry experiments and has been shown to be effective in preserving solution-phase structure into the gas phase.⁸⁹ The majority of work in this area involves proteins in positive ion mode. Much less is known about the effect of such environment on the fate of RNA gas-phase structures.

Ion mobility separation allows for the investigation of gas-phase conformation. Ion mobility separates ions based on their gas-phase mobility through a particular medium. The ions are separated by both their charge and their size, both of which affect the time it takes to travel through an ion guide. The drift time for a given ion is related to its rotationally averaged gas-phase collision cross section (CCS) according to the Mason-Schamp equation^{88,90-93}:

$$K_0 = \frac{3ze}{16N} \left(\frac{2\pi}{\mu k_B T} \right)^{1/2} \frac{1}{\Omega} \quad (\text{Equation 1.5})$$

in which K_0 is the reduced mobility, z is the number of charges on the ion, e is the elementary charge, N is the gas number density, μ is the reduced mass of the ion-neutral pair, k_B is the Boltzmann constant, T is the temperature and Ω is the experimental CCS. The calculated CCS provides insight into the gas-phase structure of biomolecules because it can be directly compared with structural data obtained by, e.g., electron microscopy (EM), NMR spectroscopy or X-ray crystallography.

The Synapt “G1” is a commercial instrument that integrates IM with mass spectrometry. The Synapt instruments have an ion mobility separation cell consisting of stacked ring ion guides. A series of DC pulses superimposed on top of RF voltages propels ions through the mobility chamber. Because of the non-uniform nature of the so-

called traveling wave, the mobility of an ion cannot be directly compared to CCS as in conventional drift time ion mobility instruments.⁹⁰ Nevertheless, with the use of carefully measured standards, it is possible to convert mobilities measured in N₂ as a drift gas in Synapt instruments into He based CCSs. Ruotolo et al. have previously published an extensive protocol for calibrating Synapt instruments.⁹⁴ The main components of the Synapt is the electrospray source, T-wave ion guide, quadrupole (for transmission of large biomolecular ions up to 8 kDa), the TriWave region, reflectron time-of-flight mass analyzer, and finally an electron multiplier detector.

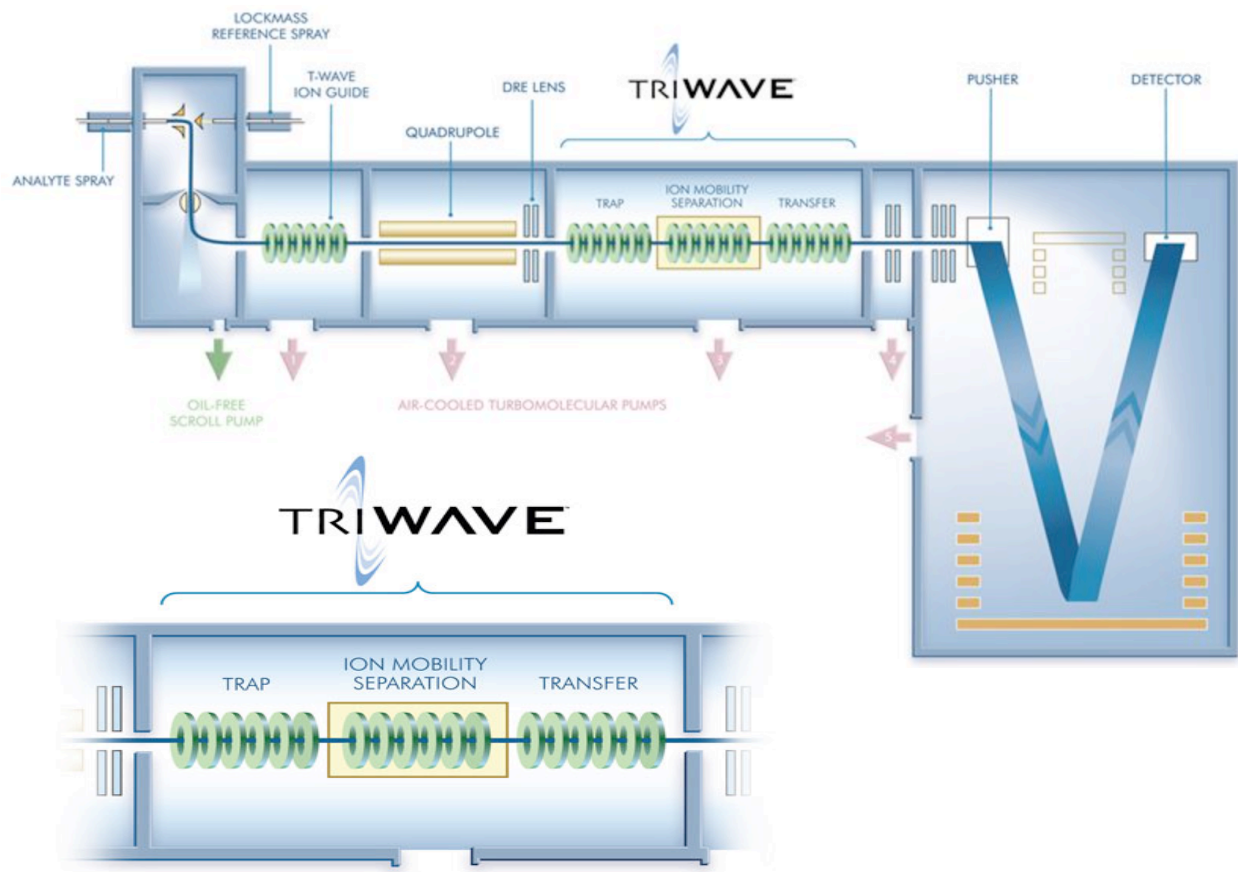


Figure 1.6: Schematic diagram of a Synapt nESI-Q-TWIMS Mass Spectrometer (Waters Corporation).

The Synapt uses a Z-Spray (Figure 1.6) nano-electrospray ionization (nESI) source and has some notable differences from the Apollo II source on the FT-ICR instrument. First, a voltage is applied to the spray capillary by a Pt wire or a metal film coated on the outside of the capillary, as opposed to the capillary being held at ground

as in the Apollo II source. The Z-spray source does not use a syringe pump to inject solvent through a capillary into the source region of the instrument; rather the capillary is loaded with approximately 5 μL of solvent containing the analyte of interest. Electroosmotic flow directs the solvent into the instrument where ionization can then occur. Voltages applied to the sampling cone direct ions further into the mass spectrometer toward the transfer optics. The orthogonal geometry of the ion source allows for the separation of ions and neutrals. A traveling wave ion guide (T-wave) is used instead of an RF only octopole in the source region.

The T-wave ion guide uses RF voltages to radially confine ions in the high-pressure region of the mass spectrometer. T-wave ion guides use stacked ring ion guides, similar to the ion funnel. By alternating the phase of the applied RF voltage for each ring, radial confinement and an effective potential well are achieved. A DC pulse is superimposed on the RF voltage, producing a moving electric field, or the so-called T-wave. The T-wave propels ions axially through the center of the electrodes. Ions 'surf' on the waves, moving down the potential gradient caused by the pulse into the lower field region. When the pulse moves forward, ions are driven forward and transmitted through the cell. The Tri-wave region of the mass spectrometer consists of three consecutive stacked ring ion guides, a collision and a storage cell (TRAP), the ion mobility cell, and an ion delivery device (TRANSFER; can also be used as a collision cell). Each ion guide operates with the T-wave principle (see above). Ions arriving in the Tri-wave region are accumulated in the TRAP T-wave and then released into the IMS T-Wave where mobility separation occurs. The ion mobility separated packets of ions are transferred to the time-of-flight analyzer by the TRANSFER T-Wave.

T-wave ion mobility separation utilizes non-uniform, moving electric field pulses to push ions through a neutral buffer gas, typically N_2 or He. As the ions traverse through the cell, they collide with the neutral buffer gas, which affects the transit time of the ions. Ions can, therefore, be separated based on their overall size, shape and charge. Species with higher mobility, more compact, 'surf' more on the wave front and are overtaken by the wave less often than species of lower mobility.

ToF analyzers separate ions based on their velocities when they traverse through a field free flight tube. The m/z of an ion is determined by measuring the time ions take to move through the drift tube and to the detector,

$$t^2 = \frac{m}{z} \left(\frac{L^2}{2eV_s} \right) \quad (\text{Equation 1.6})$$

in which t is the time needed to cover distance L and V_s is the potential used to accelerate all ions. A major advantage of ToF analyzers is the unlimited mass range, making this type of analyzer ideal for measuring large biomolecular compounds in the gas-phase. Another advantage of ToF is that it is a high throughput technique; a spectrum over a wide mass range can be obtained in microseconds. A major drawback of ToF, however, is the moderate mass resolution relative to FT-ICR. Mass resolution is affected by factors that create a distribution in flight times. These factors include the length of the ion formation pulse, size of the volume where the ions are formed, variation of initial kinetic energy, etc. Reflectrons minimizes such factors.

1.2.4 Modeling RNA Higher Order Structure

IM-MS measurements produce CCS values that are representative of gas-phase ion populations. In order for such gas-phase models to answer biologically relevant questions, they must be strongly correlated with their solution-phase counterparts. Recently, Gabelica et al. modeled the fate of nucleic acids as they undergo the electrospray process. Nucleic acids, upon desolvation, tend to self-solvate resulting in significant compaction compared to their native solution-phase structures.⁹⁵ The self-solvation of the phosphate moiety dominates over the Coulomb repulsion, which is in stark contrast to proteins in a solvent free environment, where minimal salt-bridge interactions are perturbed, producing a gas-phase structure that retain much of their solution-phase structures.³⁷ RNAs are highly charged polymers with well-defined structures in solution. Mass spectrometry can produce structures that are close to the native structure in solution; however, the solution-like gas-phase minimum may not be a true representation of the real solution-phase minimum. RNA gas-phase ions can be

compared with high-resolution solution-phase structures (e.g., from NMR or X-Ray structures). The assumption being that, for low charged species, there is minimal Coulomb repulsion along the phosphate backbone. Thus, compact conformations can be retained.^{96,97} Comparisons between gas-phase CCS structures and high-resolution solution-phase structures require refined models built via computational methods^{98,99} and subsequent calculations of theoretical CCS values via algorithms designed to simulate the IM process.^{100,101}

Molecular dynamics (MD) simulations are used to model nucleic acid gas-phase structures.^{99,102-109} Approaches such as simulated annealing¹¹⁰ and replica-exchange molecular dynamics (REMD)⁹⁸ experiments have been studied extensively and have produced detailed theoretical models. Simulated annealing, the less expensive of the two, models the process of heating a system, which unfolds the system, and then slowly lowering the temperature to allow the RNA to refold. The oscillation in temperature avoids the system from being trapped in any local minima, allows global exploration and thus sampling of a wider range of possible structures. REMD simulations enhance the sampling space, relative to standard MD simulations, by allowing systems of similar potential energies to sample conformations at different temperatures. Energy barriers on the potential energy surface may be overcome, allowing for exploration of a new conformational space. REMD is much more computationally expensive, thus, not as commonly used as the standard MD workflow. The choice of charge location is also very important when modeling nucleic acids and must be handled with care. As the size of a nucleic acid polymer increases so does the number of phosphates, thus increasing the number of possible deprotonation sites. The number of possible states for a given charge is given by:

$$P = \frac{m!}{n!(m-n)!} \quad (\text{Equation 1.7})$$

in which m is the number of phosphates and n is the number of protons needed for a given charge. The location of charge can potentially have drastic effects on the conformation that nucleic acids adopt in the gas phase.¹¹¹ A way to circumvent this issue is to assume distribution neutralization, e.g., to distribute the total charge across

all of the phosphates within the molecule by assigning a partial charge to all phosphate groups.^{112,113} The approach, although simple, has only been shown to be effective for DNA duplexes and has not yet been expanded to studies of RNA.

The most common methods for theoretical CCS calculations of *in silico* models include the projection approximation (PA)¹¹⁴, trajectory method (TM)¹¹⁵, and the exact hard sphere scattering (EHSS) method.^{101,116,117} All methods are parameterized to determine CCS values in either N₂ or He. The PA is the simplest of the approaches, equating the CCS to the average projected area of the molecule, taking into account the size of the IM background gas. PA leads to an underestimation of CCS values because it ignores scattering and long-range interactions. TM on the other hand takes into account the long-range interactions to approximate the momentum transferred from each incident collision to the target molecule. TM is often considered the most reliable method for larger biomolecules as it also takes into account the effects of multiple collisions. In the EHSS model, CCS values are calculated by averaging the momentum transfer cross section, which is related to the scattering angles between the incoming and departing background gas atom trajectory. EHSS removes long-range interactions calculated by TM, improving computational efficiency. EHSS, however, overestimates experimental CCS values.

1.3 RNA-Protein Complexes

RNAs form complexes with proteins, or ribonucleoproteins (RNPs), in the cell to perform a variety of functions. Well-known RNPs include RNase P, spliceosomes, and the ribosome, just to name a few. These RNPs are responsible for the processing to mature tRNA, transport and activity of mRNA, and are also directly involved in protein synthesis in the cell via the ribosome, respectively. RNPs stabilize, protect, and transport RNA to mediate RNA interactions with other molecules or act catalytically on RNA.

The RNA world hypothesis states that the current world was originated from early RNA catalysis. Throughout time, however, structural evidence has supported the central dogma of biology in which RNA serves mainly as genetic transfer.¹¹⁸ One exception is ribonuclease P (RNase P), which is an enzyme that catalyzes the maturation of the 5'

end of tRNA precursors by cleaving extra nucleotides at this end. Until recently, all discovered RNase P enzymes were composed of RNA and one or more protein components. However, Holzmann et al. showed evidence of a protein-only RNase P (PRORP) in human mitochondria.^{119,120} The question, therefore, is whether or not the PRORP evolved independently from the RNA-RNaseP. To help answer this question, it is of utmost importance to first understand how RNase P interacts with tRNA (binding affinity, catalytic strategies, molecular recognition etc.). To obtain a detailed understanding of how RNA-binding modulates such activity, high-resolution structures of RNA-protein complexes are necessary. High-resolution techniques such as NMR or X-ray crystallography are often not suitable for studying RNA-protein interaction sites as biologically relevant systems become too large and because such interactions are transient in nature. Therefore, as new structures are being discovered, new methods must also be developed to obtain high-resolution interaction maps so that the function of such complexes can be elucidated.

Interaction sites within RNPs can be determined either chemically or photochemically. A drawback of chemical crosslinking, such as formaldehyde crosslinking, of an RNP is that the complex may be perturbed, resulting in loss of native interactions within the complex.^{121,122} Common photochemical approaches to studying interaction sites involve combining short-range crosslinking techniques, such as UV crosslinking, with immunoprecipitation *in vivo* or *in vitro*. For example, the photoactivatable ribonucleoside enhanced crosslinking and immunoprecipitation (PAR-CLIP) method is a technique used to identify RNA-protein interaction sites in live cells.¹²³ At 254 nm, RNA nucleobases are naturally reactive, inducing a formation of a covalent bond between the reactive base and an amino acid residue in close proximity.¹²⁴ However, at 254 nm, all nucleobases are reactive, resulting in vast photo bleaching and formation of a large number of non-specific crosslinks. Incorporating base analogues such as 5-bromo-2'-deoxyuridine or 4-thio-uracil within the RNA sequence mitigates this issue to a certain extent.¹²⁵ Base analogues are reactive at longer wavelengths (306–312 nm) and can be incorporated site specifically, making the mapping of interaction sites more facile. The challenge is to successfully identify native RNA-protein crosslinks.

1.3.1 Mass Spectrometric Strategies for Identification of RNA-Protein Interactions

MS is a powerful technique that provides not only complementary sequencing information, but also provides several technical advantages over traditional biochemical techniques. For example, it enables rapid mapping of RNA-protein interactions and uses limited amounts of RNA and/or protein samples. Urlaub and co-workers have emerged as leaders in identifying RNA-protein crosslinks via bottom-up mass spectrometric techniques from developing on-line enrichment techniques to developing in-house informatics tools to streamline the data analysis.¹²⁶⁻¹³³ Such methods are not amenable for elucidation of binding sites within intact, or semi-intact, RNA moieties. Top-down mass spectrometry provides advantages over conventional bottom-up approaches through the potential to access the entire RNA (or protein) sequence.¹³⁴ Complementary tandem mass spectrometric techniques allows for a broader range of sequence information because multiple fragmentation pathways are accessed.

1.5 Dissertation Overview

This dissertation focuses on the development of mass spectrometric methods, in particular in negative-ion mode, for characterizing RNA and RNA complexes. In Chapter 2, the mechanism of niECD in the context of RNA oligonucleotide fragmentation is explored. Also, PTR is utilized as a means of charge reduction to facilitate electron capture of highly charged anionic species. Chapter 3 combines TWIMS, REMD and KD competitive binding assays to investigate the effect of solution on an A-site/aminoglycoside complex. In Chapter 4, an RNA-centric top-down approach towards RNA-peptide heteroconjugates with the goal of elucidating the binding sites between protein-only RNase P (PRORP) and pre-tRNA are explored. Chapter 5 highlights contributions made to the design and improvements of a microfluidics laboratory experiment introduced in an introductory analytical chemistry undergraduate course: CHEM 242: Introduction to Chemical Analysis Laboratory. Finally, Chapter 6

summarizes the discoveries of my doctoral work and discusses future research directions.

1.6 References

- (1) Watson, J. D.; Crick, F. H. C. The Structure of DNA. *Cold Spring Harb. Symp. Quant. Biol.* **1953**, *18*, 123-131.
- (2) Crick, F. H. C. The Complementary Structure of DNA. *PNAS* **1954**, *40*, 756-758.
- (3) Crick, F. H. C. Central Dogma of Molecular Biology. *Nature* **1970**, *227*, 561-563.
- (4) Cooper, T. A.; Wan, L.; Dreyfuss, G. RNA and disease. *Cell* **2009**, *136*, 777-793.
- (5) Venter, J. C.; Adams, M. D.; Myers, E. W.; Li, P. W.; Mural, R. J.; Sutton, G. G.; Smith, H. O.; Yandell, M.; Evans, C. A.; Holt, R. A.; Gocayne, J. D.; Amanatides, P.; Ballew, R. M.; Huson, D. H.; Wortman, J. R.; Zhang, Q.; Kodira, C. D.; Zheng, X. H.; Chen, L.; Skupski, M.; Subramanian, G.; Thomas, P. D.; Zhang, J.; Gabor Miklos, G. L.; Nelson, C.; Broder, S.; Clark, A. G.; Nadeau, J.; McKusick, V. A.; Zinder, N.; Levine, A. J.; Roberts, R. J.; Simon, M.; Slayman, C.; Hunkapiller, M.; Bolanos, R.; Delcher, A.; Dew, I.; Fasulo, D.; Flanigan, M.; Florea, L.; Halpern, A.; Hannenhalli, S.; Kravitz, S.; Levy, S.; Mobarry, C.; Reinert, K.; Remington, K.; Abu-Threideh, J.; Beasley, E.; Biddick, K.; Bonazzi, V.; Brandon, R.; Cargill, M.; Chandramouliswaran, I.; Charlab, R.; Chaturvedi, K.; Deng, Z.; Francesco, V. D.; Dunn, P.; Eilbeck, K.; Evangelista, C.; Gabrielian, A. E.; Gan, W.; Ge, W.; Gong, F.; Gu, Z.; Guan, P.; Heiman, T. J.; Higgins, M. E.; Ji, R.-R.; Ke, Z.; Ketchum, K. A.; Lai, Z.; Lei, Y.; Li, Z.; Li, J.; Liang, Y.; Lin, X.; Lu, F.; Merkulov, G. V.; Milshina, N.; Moore, H. M.; Naik, A. K.; Narayan, V. A.; Neelam, B.; Nusskern, D.; Rusch, D. B.; Salzberg, S.; Shao, W.; Shue, B.; Sun, J.; Wang, Z. Y.; Wang, A.; Wang, X.; Wang, J.; Wei, M.-H.; Wides, R.; Xiao, C.; Yan, C. The Sequence of the Human Genome. *Science* **2001**, *291*, 1304-1351.
- (6) Mattick, J. S. Challenging the Dogma: The Hidden Layer of Non-protein-coding RNAs in Complex Organisms. *Bioessays* **2003**, *25*, 930-939.
- (7) Guthrie, C.; Patterson, B. Spliceosomal snRNAs. *Annu. Rev. Genet.* **1988**, *22*, 387-419.
- (8) Cech, T. R.; Steitz, J. A. The noncoding RNA revolution-trashing old rules to forge new ones. *Cell* **2014**, *157*, 77-94.
- (9) Sahin, U.; Kariko, K.; Tureci, O. mRNA-based therapeutics--developing a new class of drugs. *Nat. Rev. Drug Discov.* **2014**, *13*, 759-780.
- (10) Seeman, N. C.; Rosenberg, J. M.; Rich, A. Sequence-specific Recognition of Double Helical Nucleic Acids by Proteins. *Proc. Natl. Acad. Sci.* **1976**, *73*, 804-808.
- (11) Adams, C. C.; Stern, D. B. Control of mRNA stability in chloroplasts by 3' inverted repeats- effects of stem and loop mutations on degradation of psbA mRNA in vitro. *Nucleic Acids Res.* **1990**, *18*, 6003-6010.
- (12) Lingel, A.; Simon, B.; Izaurralde, E.; Sattler, M. Structure and Nucleic-acid Binding of the Drosophila Argonaute 2 PAZ Domain. *Nature* **2003**, *426*, 465-469.

- (13) Gu, S. Q.; Jockel, J.; Beinker, P.; Warnecke, J.; Semenov, Y. P.; Rodnina, M. V.; Wintermeyer, W. Conformation of 4.5S RNA in the Signal Recognition Particle and on the 30S Ribosomal Subunit. *RNA* **2005**, *11*, 1374-1384.
- (14) Eubanks, C. S.; Forte, J. E.; Kapral, G. J.; Hargrove, A. E. Small Molecule-Based Pattern Recognition To Classify RNA Structure. *J. Am. Chem. Soc.* **2017**, *139*, 409-416.
- (15) Parsons, J.; Castaldi, M. P.; Dutta, S.; Dibrov, S. M.; Wyles, D. L.; Hermann, T. Conformational inhibition of the hepatitis C virus internal ribosome entry site RNA. *Nat. Chem. Biol.* **2009**, *5*, 823-825.
- (16) Zemora, G.; Waldsich, C. RNA folding in living cells. *RNA Biol.* **2014**, *7*, 634-641.
- (17) Maniatis, T.; Reed, R. The Role of Small Nuclear Ribonucleoprotein Particles in Pre-mRNA Splicing. *Nature* **1987**, *325*, 673-678.
- (18) Shi, H.; Moore, P. B. The crystal structure of yeast phenylalanine tRNA at 1.93 Å resolution- A classic structure revisited. *RNA* **2000**, *6*, 1091-1105.
- (19) Al-Hashimi, H. M. Dynamics-based amplification of RNA function and its characterization by using NMR spectroscopy. *ChemBioChem.* **2005**, *6*, 1506-1519.
- (20) Bothe, J. R.; Nikolova, E. N.; Eichhorn, C. D.; Chugh, J.; Hansen, A. L.; Al-Hashimi, H. M. Characterizing RNA dynamics at atomic resolution using solution-state NMR spectroscopy. *Nat. Methods* **2011**, *8*, 919-931.
- (21) Burge, S.; Parkinson, G. N.; Hazel, P.; Todd, A. K.; Neidle, S. Quadruplex DNA: Sequence, Topology and Structure. *Nucleic Acids Res.* **2006**, *34*, 5402-5415.
- (22) Foumy, D.; Recht, M. I.; Blanchard, S. C.; D., P. J. Structure of the A site of Escherichia coli 16S Ribosomal RNA Complexed with an Aminoglycoside Antibiotic. *Science* **1996**, *274*, 1367-1371.
- (23) Zhang, Q.; Al-Hashimi, H. M. Extending the NMR Spatial Resolution Limit for RNA by Motional Couplings. *Nat. Methods* **2008**, *5*, 243-245.
- (24) Keel, A. Y.; Rambo, R. P.; Batey, R. T.; Kieft, J. S. A general strategy to solve the phase problem in RNA crystallography. *Structure* **2007**, *15*, 761-772.
- (25) Walter, N. G. In *Curr. Protoc. in Nucleic Acid Chem.*; John Wiley & Sons, Inc.: 2003.
- (26) Rueda, D.; Bokinsky, G.; Rhodes, M. M.; Rust, M. J.; Zhuang, X.; Walter, N. G. Single-molecule enzymology of RNA- Essential functional groups impact catalysis from a distance. *PNAS* **2004**, *101*, 10066-10071.
- (27) Nordhoff, E.; Kirpekar, F.; Roepstorff, P. Mass Spectrometry of Nucleic Acids. *Mass Spectrom. Rev.* **1996**, *15*, 67-138.
- (28) Fabris, D. A role for the MS analysis of nucleic acids in the post-genomics age. *J. Am. Soc. Mass Spectrom.* **2010**, *21*, 1-13.
- (29) Fabris, D. MS analysis of nucleic acids in the post-genomic era. *Anal. Chem.* **2011**, *83*, 5810-5816.
- (30) Abi-Ghanem, J.; Gabelica, V. Nucleic acid Ion Structures in the Gas Phase. *Phys. Chem. Chem. Phys.* **2014**, *16*, 21204-21218.
- (31) Fenn, J. B.; Mann, M.; Meng, C. K.; Wong, S. F.; Whitehouse, C. M. Electrospray Ionization for Mass Spectrometry of Large Biomolecules. *Science* **1989**, *246*, 64-71.

- (32) Fenn, J. B.; Mann, M.; Meng, C. K.; Wong, S. F. Electrospray ionization-principles and practice. *Mass Spectrom. Rev.* **1990**, *9*, 37-70.
- (33) Gale, D. C.; Goodlett, D. R.; Light-Wahl, K. J.; Smith, R. D. Observation of Duplex DNA-Drug Noncovalent Complexes by Electrospray Ionization Mass Spectrometry. *J. Am. Chem. Soc.* **1994**, *116*, 6027-6028.
- (34) Limbach, P. A.; Crain, P. F.; McCloskey, J. A. Molecular Mass Measurement of Intact Ribonucleic Acids via Electrospray Ionization Quadrupole Mass Spectrometry. *J. Am. Soc. Mass Spectrom.* **1994**, *6*, 27-39.
- (35) Fernandez de la Mora, J. Electrospray Ionization of Large Multiply Charged Species Proceeds via Dole's Charged Residue Mechanism. *Anal. Chim. Acta.* **2000**, *406*, 93-104.
- (36) Kebarle, P.; Verkerk, U. H. Electrospray: From Ions in Solution to Ions in the Gas Phase, What We Know Now. *Mass Spectrom. Rev.* **2009**, *28*, 898-917.
- (37) Konermann, L.; Ahadi, E.; Rodriguez, A. D.; Vahidi, S. Unraveling the Mechanism of Electrospray Ionization. *Anal. Chem.* **2013**, *85*, 2-9.
- (38) Kebarle, P.; Tang, L. From Ions in Solution to Ions in the Gas Phase- The Mechanism of Electrospray Mass Spectrometry. *Anal. Chem.* **1993**, *65*, 972-986.
- (39) Fourmy, D.; Yoshizawa, S.; Puglisi, J. D. Paromomycin Binding Induces a Local Conformational Change in the A-site of 16 S rRNA. *J. Mol. Biol.* **1998**, *277*, 333-345.
- (40) Marshall, A. G.; Grosshans, P. B. Fourier Transform Ion Cyclotron Resonance Mass Spectrometry: The Teenage Years Marshall. *Anal. Chem.* **1991**, *63*, 215-229.
- (41) Amster, J. I. Fourier Transform Mass Spectrometry. *J. Mass Spectrom.* **1996**, *31*, 1325-1337.
- (42) Marshall, A. G.; Hendrickson, C. L.; Jackson, G. S. Fourier Transform Ion Cyclotron Resonance Mass Spectrometry: A Primer. *Mass Spectrom. Rev.* **1998**, *17*, 1-35.
- (43) Shi, S. D. H.; Drader, J. J.; Hendrickson, C. L.; Marshall, A. G. Fourier Transform Ion Cyclotron Resonance Mass Spectrometry in a High Homogeneity 25 Tesla Resistive Magnet. *J. Am. Soc. Mass Spectrom.* **1999**, *10*, 265-268.
- (44) Marshall, A. G. Milestones in Fourier Transform Ion Cyclotron Resonance Mass Spectrometry Technique Development. *Int. J. Mass Spectrom.* **2000**, *200*, 331-356.
- (45) Marshall, A. G.; Hendrickson, C. L. Fourier Transform Ion Cyclotron Resonance Detection Principles and Experimental Configurations. *Int. J. Mass Spectrom.* **2001**, *215*, 59-75.
- (46) Schaub, T. M.; Hendrickson, C. L.; Horning, S.; Quinn, J. P.; Senko, M. W.; Marshall, A. G. High-Performance Mass Spectrometry: Fourier Transform Ion Cyclotron Resonance at 14.5 Tesla. *Anal. Chem.* **2008**, *80*, 3985-3990.
- (47) Kelly, R. T.; Tolmachev, A. V.; Page, J. S.; Tang, K.; Smith, R. D. The Ion Funnel: Theory, Implementations, and Applications. *Mass Spectrom. Rev.* **2010**, *29*, 294-312.
- (48) Guan, S.; Marshall, A. G. Stacked-Ring Electrostatic Ion Guide. *J. Am. Soc. Mass Spectrom.* **1995**, *7*, 101-106.

- (49) Shaffer, S. A.; Tolmachev, A. V.; Prior, D. C.; Anderson, G. A.; Udeseth, H. R.; Smith, R. D. Characterization of an Improved Electrodynamic Ion Funnel Interface for Electrospray Ionization Mass Spectrometry. *Anal. Chem.* **1999**, *71*, 2957-2964.
- (50) Tolmachev, A. V.; Udeseth, H. R.; Smith, R. D. Radial Stratification of Ions as a Function of Mass to Charge Ratio in Collisional Cooling Radio Frequency Multipoles Used as Ion Guides or Ion Traps. *Rapid Commun. Mass Spectrom.* **2000**, *14*, 1907-1913.
- (51) Huang, T. Y.; Kharlamova, A.; Liu, J.; McLuckey, S. A. Ion Trap Collision-induced Dissociation of Multiply Deprotonated RNA: c/y-ions versus (a-B)/w-ions. *J. Am. Soc. Mass Spectrom.* **2008**, *19*, 1832-1840.
- (52) Huang, T.; Liu, J.; Liang, X.; Hodges, B. D. M.; McLuckey, S. A. Collision-Induced Dissociation of Intact Duplex and Single-Stranded siRNA Anions. *Anal. Chem.* **2008**, *80*, 8501-8508.
- (53) Harper, B.; Neumann, E. K.; Solouki, T. DNA Oligonucleotide Fragment Ion Rearrangements Upon Collision-Induced Dissociation. *J. Am. Soc. Mass Spectrom.* **2015**, *26*, 1404-1413.
- (54) Hakansson, K.; Hudgins, R. R.; O'Hair, R. A. J.; Marshall, A. G. Electron Capture Dissociation and Infrared Multiphoton Dissociation of Oligodeoxynucleotide Dications. *J. Am. Soc. Mass Spectrom.* **2003**, *14*, 23-41.
- (55) Smith, S. I.; Brodbelt, J. S. Characterization of Oligodeoxynucleotides and Modifications by 193 nm Photodissociation and Electron Photodetachment Dissociation. *Anal. Chem.* **2010**, *82*, 7218-7226.
- (56) Smith, S. I.; Brodbelt, J. S. Hybrid Activation Methods for Elucidating Nucleic Acid Modifications. *Anal. Chem.* **2011**, *83*, 303-310.
- (57) Zubarev, R. A.; Kelleher, N. L.; McLafferty, F. W. Electron Capture Dissociation of Multiply Charged Protein Cations. A Nonergodic Process. *J. Am. Chem. Soc.* **1998**, *120*, 3265-3266.
- (58) Cooper, H. J.; Hakansson, K.; Marshall, A. G. The Role of Electron Capture Dissociation in Biomolecular Analysis. *Mass Spectrom. Rev.* **2005**, *24*, 201-222.
- (59) Yang, J.; Hakansson, K. Fragmentation of oligoribonucleotides from gas-phase ion-electron reactions. *J. Am. Soc. Mass Spectrom.* **2006**, *17*, 1369-1375.
- (60) Gao, Y.; McLuckey, S. A. Electron transfer followed by collision-induced dissociation (NET-CID) for generating sequence information from backbone-modified oligonucleotide anions. *Rapid Commun. Mass Spectrom.* **2013**, *27*, 249-257.
- (61) Budnik, B. A.; Haselmann, K. F.; Zubarev, R. A. Electron Detachment Dissociation of Peptide Di-anions an Electron Hole Recombination Phenomenon. *Chem. Phys. Lett.* **2001**, 299-302.
- (62) Yang, J.; Hakansson, K. Characterization and optimization of electron detachment dissociation Fourier transform ion cyclotron resonance mass spectrometry. *Int. J. Mass Spectrom.* **2008**, *276*, 144-148.
- (63) Yang, J.; Mo, J.; Adamson, J. T.; Hakansson, K. Characterization of Oligodeoxynucleotides by Electron Detachment Dissociation Fourier Transform Ion Cyclotron Resonance Mass Spectrometry. *Anal. Chem.* **2005**, *77*, 1876-1882.

- (64) Hersberger, K. E.; Hakansson, K. Characterization of O-sulfopeptides by negative ion mode tandem mass spectrometry: superior performance of negative ion electron capture dissociation. *Anal. Chem.* **2012**, *84*, 6370-6377.
- (65) Yoo, H. J.; Wang, N.; Zhuang, S.; Song, H.; Hakansson, K. Negative-ion electron capture dissociation: radical-driven fragmentation of charge-increased gaseous peptide anions. *J. Am. Chem. Soc.* **2011**, *133*, 16790-16793.
- (66) Wu, J.; McLuckey, S. A. Gas-phase Fragmentation of Oligonucleotide Ions. *Int. J. Mass. Spectrom.* **2004**, *237*, 197-241.
- (67) Schurch, S. Characterization of Nucleic Acids by Tandem Mass Spectrometry - The Second Decade (2004-2013): From DNA to RNA and Modified Sequences. *Mass Spectrom. Rev.* **2016**, *35*, 483-523.
- (68) Huang, Y.; Guan, S.; Kim, H. S.; Marshall, A. G. Ion Transport Through a Strong Magnetic Field Gradient by R.F.-only Octupole Ion Guides. *Int. J. Mass Spectrom.* **1996**, *152*, 121-133.
- (69) Bartlett, M. G.; McCloskey, J. A.; Manalili, S.; Griffey, R. H. The Effect of Backbone Charge on the Collision-Induced Dissociation of Oligonucleotides. *J. Mass Spectrom.* **1996**, *31*, 1277-1283.
- (70) Mikhailov, V. A.; Cooper, H. J. Activated Ion Electron Capture Dissociation (AI ECD) of Proteins: Synchronization of Infrared and Electron Irradiation with Ion Magnetron Motion. *J. Am. Soc. Mass Spectrom.* **2009**, *20*, 763-771.
- (71) Chan, T. W.; Choy, M. F.; Chan, W. Y.; Fung, Y. M. A Mechanistic Study of the Electron Capture Dissociation of Oligonucleotides. *J. Am. Soc. Mass Spectrom.* **2009**, *20*, 213-226.
- (72) Taucher, M.; Breuker, K. Characterization of modified RNA by top-down mass spectrometry. *Angew Chem. Int. Ed. Engl.* **2012**, *51*, 11289-11292.
- (73) Andersen, T. E.; Kirpekar, F.; Haselmann, K. F. RNA fragmentation in MALDI mass spectrometry studied by H/D-exchange: mechanisms of general applicability to nucleic acids. *J Am Soc Mass Spectrom* **2006**, *17*, 1353-1368.
- (74) Voinov, V. G.; Bennett, S. E.; Beckman, J. S.; Barofsky, D. F. ECD of tyrosine phosphorylation in a triple quadrupole mass spectrometer with a radio-frequency-free electromagnetostatic cell. *J. Am. Soc. Mass Spectrom.* **2014**, *25*, 1730-1738.
- (75) Voinov, V. G.; Beckman, J. S.; Deinzer, M. L.; Barofsky, D. F. Electron-capture dissociation (ECD), collision-induced dissociation (CID) and ECD/CID in a linear radio-frequency-free magnetic cell. *Rapid Commun. Mass Spectrom.* **2009**, *23*, 3028-3030.
- (76) Voinov, V. G.; Deinzer, M. L.; Barofsky, D. F. Radio-Frequency-Free Cell for Electron Capture Dissociation in Tandem Mass Spectrometry. *Anal. Chem.* **2009**, *81*, 1238-1243.
- (77) Silivra, O. A.; Kjeldsen, F.; Ivonin, I. A.; Zubarev, R. A. Electron Capture Dissociation of Polypeptides in a Three-dimensional Quadrupole Ion Trap: Implementation and First Results. *J. Am. Soc. Mass Spectrom.* **2005**, *16*, 22-27.
- (78) Baba, T.; Campbell, J. L.; Le Blanc, J. C.; Hager, J. W.; Thomson, B. A. Electron Capture Dissociation in a Branched Radio-frequency Ion Trap. *Anal. Chem.* **2015**, *87*, 785-792.
- (79) Ben Hamidane, H.; Chiappe, D.; Hartmer, R.; Vorobyev, A.; Moniatte, M.; Tsybin, Y. O. Electron Capture and Transfer Dissociation: Peptide Structure Analysis at

- Different Ion Internal Energy Levels. *J. Am. Soc. Mass. Spectrom.* **2009**, *20*, 567-575.
- (80) Drabik, A.; Bodzon-Kulakowska, A.; Suder, P. Application of the ETD/PTR reactions in top-down proteomics as a faster alternative to bottom-up nanoLC-MS/MS protein identification. *J. Mass Spectrom.* **2012**, *47*, 1347-1352.
- (81) Holden, D. D.; Brodbelt, J. S. Ultraviolet Photodissociation of Native Proteins Following Proton Transfer Reactions in the Gas Phase. *Anal. Chem.* **2016**, *88*, 12354-12362.
- (82) Laszlo, K. J.; Munger, E. B.; Bush, M. F. Folding of Protein Ions in the Gas Phase after Cation-to-Anion Proton-Transfer Reactions. *J. Am. Chem. Soc.* **2016**, *138*, 9581-9588.
- (83) Martens, J.; Berden, G.; Oomens, J. Structures of Fluoranthene Reagent Anions Used in Electron Transfer Dissociation and Proton Transfer Reaction Tandem Mass Spectrometry. *Anal. Chem.* **2016**, *88*, 6126-6129.
- (84) Holden, D. D.; McGee, W. M.; Brodbelt, J. S. Integration of Ultraviolet Photodissociation with Proton Transfer Reactions and Ion Parking for Analysis of Intact Proteins. *Anal. Chem.* **2016**, *88*, 1008-1016.
- (85) Laszlo, K. J.; Buckner, J. H.; Munger, E. B.; Bush, M. F. Native-Like and Denatured Cytochrome c Ions Yield Cation-to-Anion Proton Transfer Reaction Products with Similar Collision Cross-Sections. *J. Am. Soc. Mass Spectrom.* **2017**, *28*, 1382-1391.
- (86) Laszlo, K. J.; Munger, E. B.; Bush, M. F. Effects of Solution Structure on the Folding of Lysozyme Ions in the Gas Phase. *J. Phys. Chem. B.* **2017**, *121*, 2759-2766.
- (87) Laszlo, K. J.; Bush, M. F. Interpreting the Collision Cross Sections of Native-like Protein Ions: Insights from Cation-to-Anion Proton-Transfer Reactions. *Anal. Chem.* **2017**, *89*, 7607-7614.
- (88) Uetrecht, C.; Rose, R. J.; van Duijn, E.; Lorenzen, K.; Heck, A. J. Ion Mobility Mass Spectrometry of Proteins and Protein Assemblies. *Chem. Soc. Rev.* **2010**, *39*, 1633-1655.
- (89) Heck, A. J. Native mass spectrometry: a bridge between interactomics and structural biology. *Nat. Methods* **2008**, *5*, 927-933.
- (90) Shvartsburg, A. A.; Smith, R. D. Fundamentals of Traveling Wave Ion Mobility Spectrometry. *Anal. Chem.* **2008**, *80*, 9689-9699.
- (91) Smith, D. P.; Knapman, T. W.; Campuzano, I.; Malham, R. W.; Berryman, J. T.; Radford, S. E.; Ashcroft, A. E. Deciphering Drift Time Measurements from Travelling Wave Ion Mobility Spectrometry-mass Spectrometry Studies. *Eur. J. Mass Spectrom.* **2009**, *15*, 113-130.
- (92) Clemmer, D. E.; Jarrold, M. F. Ion Mobility Measurements and their Applications to Clusters and Biomolecules. *J. Mass. Spectrom.* **1997**, *32*, 577-592.
- (93) Hilton, G. R.; Benesch, J. L. Two Decades of Studying Non-covalent Biomolecular Assemblies by Means of Electrospray Ionization Mass Spectrometry. *J. R. Soc. Interface* **2012**, *9*, 801-816.
- (94) Ruotolo, B. T.; Benesch, J. L.; Sandercock, A. M.; Hyung, S. J.; Robinson, C. V. Ion Mobility-mass Spectrometry Analysis of Large Protein Complexes. *Nat. Protoc.* **2008**, *3*, 1139-1152.

- (95) Porrini, M.; Rosu, F.; Rabin, C.; Darre, L.; Gomez, H.; Orozco, M.; Gabelica, V. Compaction of Duplex Nucleic Acids upon Native Electrospray Mass Spectrometry. *ACS Cent. Sci.* **2017**, *3*, 454-461.
- (96) Baker, E. S.; Bowers, M. T. B-DNA helix stability in a solvent-free environment. *J. Am. Soc. Mass Spectrom.* **2007**, *18*, 1188-1195.
- (97) Baker, E. S.; Dupuis, N. F.; Bowers, M. T. DNA Hairpin, Pseudoknot, and Cruciform Stability in a Solvent-Free Environment. *J. Phys. Chem. B.* **2009**, *113*, 1722-1727.
- (98) Sugita, Y.; Okamoto, Y. Replica-Exchange Molecular Dynamics Method for Protein Folding. *Chem. Phys. Lett.* **1999**, *314*, 141-151.
- (99) Shapiro, B. A.; Yingling, Y. G.; Kasprzak, W.; Bindewald, E. Bridging The Gap in RNA Structure Prediction. *Curr. Opin. Struct. Biol.* **2007**, *17*, 157-165.
- (100) Marklund, E. G.; Degiacomi, M. T.; Robinson, C. V.; Baldwin, A. J.; Benesch, J. L. Collision Cross Sections for Structural Proteomics. *Structure* **2015**, *23*, 791-799.
- (101) Larriba, C.; Hogan, C. J. Free molecular collision cross section calculation methods for nanoparticles and complex ions with energy accommodation. *J. Comput. Phys.* **2013**, *251*, 344-363.
- (102) Feig, M.; Karanicolas, J.; Brooks, C. L., 3rd MMTSB Tool Set: enhanced sampling and multiscale modeling methods for applications in structural biology. *J. Mol. Graph Model* **2004**, *22*, 377-395.
- (103) Brooks, B. R.; Brooks, C. L., 3rd; Mackerell, A. D., Jr.; Nilsson, L.; Petrella, R. J.; Roux, B.; Won, Y.; Archontis, G.; Bartels, C.; Boresch, S.; Caffisch, A.; Caves, L.; Cui, Q.; Dinner, A. R.; Feig, M.; Fischer, S.; Gao, J.; Hodoscek, M.; Im, W.; Kuczera, K.; Lazaridis, T.; Ma, J.; Ovchinnikov, V.; Paci, E.; Pastor, R. W.; Post, C. B.; Pu, J. Z.; Schaefer, M.; Tidor, B.; Venable, R. M.; Woodcock, H. L.; Wu, X.; Yang, W.; York, D. M.; Karplus, M. CHARMM: the biomolecular simulation program. *J. Comput. Chem.* **2009**, *30*, 1545-1614.
- (104) Perez, A.; Marchan, I.; Svozil, D.; Sponer, J.; Cheatham, T. E., 3rd; Laughton, C. A.; Orozco, M. Refinement of the AMBER Force Field for Nucleic Acids: Improving the Description of Alpha/Gamma Conformers. *Biophys. J.* **2007**, *92*, 3817-3829.
- (105) Cornell, W. D.; Cieplak, P.; Bayly, C. I.; Gould, I. R.; Merz, K. M.; Ferguson, D. M.; Spellmeyer, D. C.; Fox, T.; Caldwell, J. W.; Kollman, P. A. A Second Generation Force Field for the Simulation of Proteins, Nucleic Acids, and Organic Molecules. *J. Am. Chem. Soc.* **1995**, *117*, 5179-5197.
- (106) Foloppe, N.; Mackerell, A. D., Jr. All-atom Empirical Force Field for Nucleic Acids- I. Parameter Optimization Based on Small Molecule and Condensed Phase Macromolecular Target Data. *J. Comput. Chem.* **2000**, *21*, 86-104.
- (107) Duan, Y.; Wu, C.; Chowdhury, S.; Lee, M. C.; Xiong, G.; Zhang, W.; Yang, R.; Cieplak, P.; Luo, R.; Lee, T.; Caldwell, J.; Wang, J.; Kollman, P. A Point-Charge Force Field for Molecular Mechanics Simulations of Proteins Based on Condensed-Phase Quantum Mechanical Calculations. *J. Comput. Chem.* **2003**, *24*, 1999-2012.
- (108) Reddy, S. Y.; Leclerc, F.; Karplus, M. DNA Polymorphism A Comparison of Force Fields for Nucleic Acids. *Biophys. J.* **2003**, *84*, 1421-1449.

- (109) Hornak, V.; Abel, R.; Okur, A.; Strockbine, B.; Roitberg, A.; Simmerling, C. Comparison of multiple Amber force fields and development of improved protein backbone parameters. *Proteins* **2006**, *65*, 712-725.
- (110) Schmitz, M.; Steger, G. Description of RNA Folding by "Simulated Annealing". *J. Mol. Biol.* **1996**, *225*, 254-266.
- (111) Hoaglund, C. S.; Liu, Y.; Ellington, A. D.; Pagel, M.; Clemmer, D. E. Gas-Phase DNA Oligothymidine Ion Conformers. *J. Am. Chem. Soc.* **1997**, *119*, 9051-9052.
- (112) Rueda, M.; Kalko, S. G.; Luque, J.; Orozco, M. The Structure and Dynamics of DNA in the Gas Phase. *J. Am. Chem. Soc.* **2003**, *125*, 8007-8014.
- (113) Arcella, A.; Portella, G.; Ruiz, M. L.; Eritja, R.; Vilaseca, M.; Gabelica, V.; Orozco, M. Structure of Triplex DNA in the Gas Phase. *J. Am. Chem. Soc.* **2012**, *134*, 6596-6606.
- (114) Bleiholder, C.; Wyttenbach, T.; Bowers, M. T. A novel projection approximation algorithm for the fast and accurate computation of molecular collision cross sections (I). *Method. Int. J. Mass Spectrom.* **2011**, *308*, 1-10.
- (115) Mesleh, M. F.; Hunter, J. M.; Shvartsburg, A. A.; Schatz, G. C.; Jarrold, M. F. Structural Information from Ion Mobility Measurements- Effects of the Long-Range Potential. *J. Phys. Chem.* **1996**, 16082-16086.
- (116) Shvartsburg, A. A.; Jarrold, M. F. An exact hard-spheres scattering model for the mobilities of polyatomic ions. *Chem. Phys. Lett.* **1996**, *261*, 86-91.
- (117) Jurneczko, E.; Barran, P. E. How useful is ion mobility mass spectrometry for structural biology? The relationship between protein crystal structures and their collision cross sections in the gas phase. *Analyst* **2011**, *136*, 20-28.
- (118) Gesteland, R. F.; Cech, T. R.; Atkins, J. F. *The RNA World*; Cold Spring Harbor Laboratory Press: New York, 1999.
- (119) Holzmann, J.; Frank, P.; Loffler, E.; Bennett, K. L.; Gerner, C.; Rossmann, W. RNase P without RNA: Identification and Functional Reconstitution of the Human Mitochondrial tRNA Processing Enzyme. *Cell* **2008**, *135*, 462-474.
- (120) Howard, M. J.; Lim, W. H.; Fierke, C. A.; Koutmos, M. Mitochondrial Ribonuclease P Structure Provides Insight into the Evolution of Catalytic Strategies for Precursor-tRNA 5' Processing. *Proc. Natl. Acad. Sci.* **2012**, *109*, 16149-16154.
- (121) Sutherland, B. W.; Toews, J.; Kast, J. Utility of Formaldehyde Cross-linking and Mass Spectrometry in the Study of Protein-protein Interactions. *J. Mass Spectrom.* **2008**, *43*, 699-715.
- (122) Hoffman, E. A.; Frey, B. L.; Smith, L. M.; Auble, D. T. Formaldehyde crosslinking: a tool for the study of chromatin complexes. *J Biol Chem* **2015**, *290*, 26404-26411.
- (123) Hafner, M.; Landthaler, M.; Burger, L.; Khorshid, M.; Hausser, J.; Berninger, P.; Rothballer, A.; Ascano, M., Jr.; Jungkamp, A. C.; Munschauer, M.; Ulrich, A.; Wardle, G. S.; Dewell, S.; Zavolan, M.; Tuschl, T. Transcriptome-wide identification of RNA-binding protein and microRNA target sites by PAR-CLIP. *Cell* **2010**, *141*, 129-141.
- (124) Saito, I.; Sugiyama, H.; Matsuura, T. Photochemical Reactions of Nucleic Acids and Their Constituents of Photobiological Relevance. *Photochem. Photobiol.* **1983**, *38*, 735-743.

- (125) Willis, M. C.; LeCuyer, K. A.; Meisenheimer, K. M.; Uhlenbeck, O. C.; Koch, T. H. An RNA Protein Contact Determined by 5 Bromouridine substitution, Photocrosslinking and Sequencing. *Nucleic Acids Res.* **1994**, *22*, 4947-4952.
- (126) Kramer, K.; Sachsenberg, T.; Beckmann, B. M.; Qamar, S.; Boon, K. L.; Hentze, M. W.; Kohlbacher, O.; Urlaub, H. Photo-cross-linking and High-resolution Mass spectrometry for Assignment of RNA-binding sites in RNA-binding Proteins. *Nat. Methods* **2014**, *11*, 1064-1070.
- (127) Kuhn-Holsken, E.; Lenz, C.; Sander, B.; Luhrmann, R.; Urlaub, H. Complete MALDI-ToF MS Analysis of Cross-linked Peptide–RNA Oligonucleotides Derived from Nonlabeled UV-irradiated Ribonucleoprotein Particles. *RNA* **2005**, *11*, 1915-1930.
- (128) Lenz, C.; Kuhn-Holsken, E.; Urlaub, H. Detection of Protein-RNA Crosslinks by NanoLC-ESI-MS/MS using Precursor ion Scanning and Multiple Reaction Monitoring (MRM) Experiments. *J. Am. Soc. Mass Spectrom.* **2007**, *18*, 869-881.
- (129) Kuhn-Holsken, E.; Dybkov, O.; Sander, B.; Luhrmann, R.; Urlaub, H. Improved Identification of Enriched Peptide RNA Cross-links From Ribonucleoprotein Particles (RNPs) by Mass Spectrometry. *Nucleic Acids Res.* **2007**, *35*, e95.
- (130) Luo, X.; Hsiao, H. H.; Bubunencko, M.; Weber, G.; Court, D. L.; Gottesman, M. E.; Urlaub, H.; Wahl, M. C. Structural and Functional Analysis of the E. coli NusB-S10 Transcription Antitermination Complex. *Mol. Cell* **2008**, *32*, 791-802.
- (131) Richter, F. M.; Hsiao, H. H.; Plessmann, U.; Urlaub, H. Enrichment of Protein-RNA Crosslinks from Crude UV-Irradiated Mixtures for MS Analysis by On-line Chromatography Using Titanium Dioxide Columns. *Biopolymers* **2009**, *91*, 297-309.
- (132) Kramer, K.; Hummel, P.; Hsiao, H.-H.; Luo, X.; Wahl, M.; Urlaub, H. Mass-spectrometric Analysis of Proteins Cross-linked to 4-thio-uracil- and 5-bromo-uracil-substituted RNA. *Int. J. Mass Spectrom.* **2011**, *304*, 184-194.
- (133) Schmidt, C.; Kramer, K.; Urlaub, H. Investigation of protein-RNA interactions by mass spectrometry-Techniques and applications. *J. Proteomics* **2012**, *75*, 3478-3494.
- (134) Schneeberger, E. M.; Breuker, K. Native Top-Down Mass Spectrometry of TAR RNA in Complexes with a Wild-Type tat Peptide for Binding Site Mapping. *Angew. Chem. Int. Ed.* **2017**, *56*, 1254-1258.

Chapter 2

Exploration of the Negative Ion Electron Capture Dissociation (niECD) Mechanism for RNA Oligonucleotides and Proton Transfer Reactions for Improved niECD

2.1 Introduction

Nucleic acids are essential for various cellular processes as they are responsible for the storage and transfer of genetic information, which ultimately dictate cellular function. Ribonucleic acids (RNAs) are particularly unique as they can both carry genetic information and have catalytic function.¹ Similar to proteins, the structures of nucleic acids are closely related to their cellular functions. However, compared with the proteome, much less is known about RNA detailed structure and function. Nuclear magnetic resonance (NMR) spectroscopy is widely used for characterization of nucleic acids as it provides high resolution and dynamic information.^{2,3} NMR, however, suffers from size and sensitivity limitations. Fluorescence resonance energy transfer (FRET) is a labeling technique that can provide single molecule information.⁴ FRET, however, is limited by the placement of the added fluorophores. Mass spectrometry, on the other hand, is a powerful, versatile, highly sensitive, label-free technique that can be used for the structural interrogation of nucleic acids in a manner complementary to other biophysical techniques.

Various tandem mass spectrometry (MS/MS) techniques have been applied for the sequence and structural analysis of nucleic acids.⁵⁻⁷ Commonly employed MS/MS strategies involve vibrational activation from slow heating, such as collision induced dissociation (CID) and infrared multiphoton dissociation (IRMPD).⁸⁻¹⁴ One major disadvantage for oligonucleotide sequencing in this manner is extensive uninformative neutral loss such as water and nucleobase loss. Such losses spread available signal over multiple peaks, which complicates spectral interpretation and decreases sensitivity.

Positive-ion mode electron-based fragmentation methods such as electron capture dissociation (ECD) and electron transfer dissociation (ETD) provide extensive sequence coverage with limited neutral losses and complementary sequence informative fragments to the aforementioned slow heating fragmentation techniques.¹⁵⁻²⁰ However, nucleic acids are inherently negatively charged because of their highly acidic phosphate backbone. Therefore, nucleic acids have higher ionization efficiency in negative-ion mode compared with positive ion-mode. As a result, MS/MS techniques that operate in negative-ion mode are preferred. Breuker and co-workers have shown the utility of CID in negative-ion mode to probe interaction sites in RNA-peptide complexes.¹² However, similar to positive-ion mode CID, they observed extensive base loss. Taucher and Breuker also showed the utility of electron detachment dissociation (EDD) for probing base modifications in up to 61 base pair RNA.^{21,22} EDD of multiply charged RNA oligomers has been shown to produce *c*-, *y*-, *d*- and *w*-type ions. EDD of larger RNAs provided evidence that the *c*- and *y*-type ions may result from vibrational activation. EDD, however, requires low mass-to-charge (*m/z*), multiply charged ions and is thus not applicable to singly charged ions, or to native MS applications.

We previously described a phenomenon in which electrons within a certain energy range (~3.5-6.5 eV) are captured by peptide anions, resulting in a charge-increased radical intermediate, which further dissociates and produces fragment ions similar to ECD or ETD.²³ We termed this process negative-ion electron capture dissociation (niECD). We have shown the superiority of niECD over other negative ion MS/MS techniques for PTM site mapping in sulfopeptides as niECD is able to retain this highly labile modification.²⁴ Gas-phase zwitterionic structures appear essential for niECD.²³ Similar to peptides, nucleic acids have the ability to form zwitterions in the gas phase due to the acidic nature of the phosphate backbone and the basic nature of the nitrogenous nucleobases.^{25,26} A previous Håkansson lab member, Hangtian Song, showed that oligonucleotides can capture electrons but that limited fragmentation occurs, likely due to intramolecular salt bridges preventing the product ion pairs from separating.²⁷

RNAs are typically highly negatively charged in the gas phase. As the number of residues increases, so does the number of phosphates along the RNA backbone and,

as a result, the number of possible negatively charged sites also increases. Increased charge is problematic when attempting niECD, due to increased Coulomb repulsion. Thus, low charge states are preferred. It has been shown that, by altering solvent composition (i.e., organic composition and pH), oligonucleotide charge states can be reduced.^{28,29} An alternate means of charge reduction is gas-phase proton transfer reactions (PTR).³⁰⁻³² PTR involves gas-phase reactions between anions and a reagent ion carrying a positive charge (i.e., protonated fluoranthene). Protonated fluoranthene can be formed via chemical ionization (CI) in an external CI source. Recently, Brodbelt and co-workers have shown the utility of PTR for charge state manipulation prior to UVPD of intact proteins.^{33,34} Bush and co-workers coupled PTR with ion mobility spectrometry to probe the charge state dependence of protein gas-phase conformation.³⁵⁻³⁷

In this Chapter, we extend niECD to additional RNA oligonucleotides, investigate the nucleobase dependency of niECD electron capture efficiency. A series of RNA hexamers; the homopolymers rA₆, rG₆, rU₆, rC₆, and the mono-substituted hexamers rAUUUUU, rUUAUUU, and rUUUUUA, were subjected to electron irradiation and evaluated for their propensities for gas-phase electron capture. Furthermore, we propose a mechanism for electron capture (and dissociation) by RNA anions. Finally, we employ PTR as a means for charge state reduction prior to niECD of a mixed sequence hexamer, rGCAUAC and an eleven-mer sequence.

2.2 Experimental

2.2.1 Reagents

All oligonucleotides were purchased from Integrated DNA Technologies, Inc. (Coralville, IA). Six-mer and 11-mer RNAs were dissolved in electrospray solution (1% triethylamine in 50% (v/v) H₂O, 50% methanol) and electrosprayed at 1 μ M to 5 μ M concentrations. C-18 ZipTips were used for further desalting, if needed.

2.2.2 Mass Spectrometry

All mass spectra were acquired with a 7-T quadrupole-FT-ICR mass spectrometer (Solarix, Bruker Daltonics, Billerica, MA). Oligonucleotides were infused into an Apollo II electrospray ionization source at an ESI Flow rate of 100 $\mu\text{L/h}$. The capillary voltages ranged from 3,500 to 3,800 V for negative-ion mode analysis. The drying gas flow rate and drying gas temperature were set to 4.0 L/min and 180°C, respectively, for all experiments. Ions were selected by the external quadrupole, accumulated in a hexapole for 1.0 to 5.0 seconds and transported to the ICR cell for further activation and dissociation. For niECD experiments, the cathode bias was set to - 4.0 to - 6.0 V with the ECD lens ranging from - 2.5 to - 4.5 V. Time domain data were Fourier transformed and resulting frequencies corresponding to m/z 200 to 2000 were displayed via ftmsControl software (version 2.1, Bruker Daltonics) at 1M data points, summed over 64–128 scans. The data were analyzed by Compass DataAnalysis software (version 4.4 Bruker, Daltonics). Calculated m/z values for oligonucleotides and their product ions were obtained from Mongo Oligo Mass Calculator v2.08 (<http://mods.rna.albany.edu/masspec/Mongo-Oligo>). All product ion peaks were manually assigned within 10 ppm mass accuracy.

2.3 Results and Discussion

2.3.1 niECD of RNA Hexamers and Mechanism of Fragmentation

Within a narrow range of electron irradiation energy (4.0 to 6.0 eV), electron-capture is observed for singly deprotonated RNA anionic hexamers. For rA_6 (Figure 2.1a) and rG_6 , the only observed products were the charge increased species, $[M - H]^{2-}$, whereas, for rC_6 , the dominant peaks were $[M - H]^{2-}$ and $[M - H - H_2O]^{2-}$. For rC_6 , d_2/w_2 , d_3/w_3 , and d_5/w_5 ions from backbone cleavage were also observed at lower abundances. For rU_6 (Figure 2.1b), the dominant product ion was $d_5/w_5^{2''}$ (the double prime denotes the addition of two hydrogen radicals)³⁸ in addition to less abundant d_2/w_2 , d_3/w_3 , d_4/w_4 , and d_5/w_5 ions. The charge-increased species was also observed but at significantly lower ion abundance compared to its purine counterparts. For these homopolymers, d and w

ions are isomeric and thus indistinguishable because of the symmetry of the sequences. Similar results were previously reported by Hangtian Song;²⁷ however, a mechanism for niECD of RNA oligonucleotides was not proposed in that work. Previous density functional theory (DFT) calculations revealed that electron capture at protonated purines is more exothermic than their pyrimidine counterparts.¹⁹ Furthermore, purine radical species are stabilized by the delocalized environment between the fused imidazole and pyrimidine rings, thus radical migration to the phosphate backbone is less likely, which may explain the limited backbone fragmentation observed. Alternatively, as proposed by Hangtian Song,²⁷ the greater stability of purine-containing ions may be due to intramolecular hydrogen bonds between nucleobases and phosphate groups, preventing the product ions from separating.^{18,39}

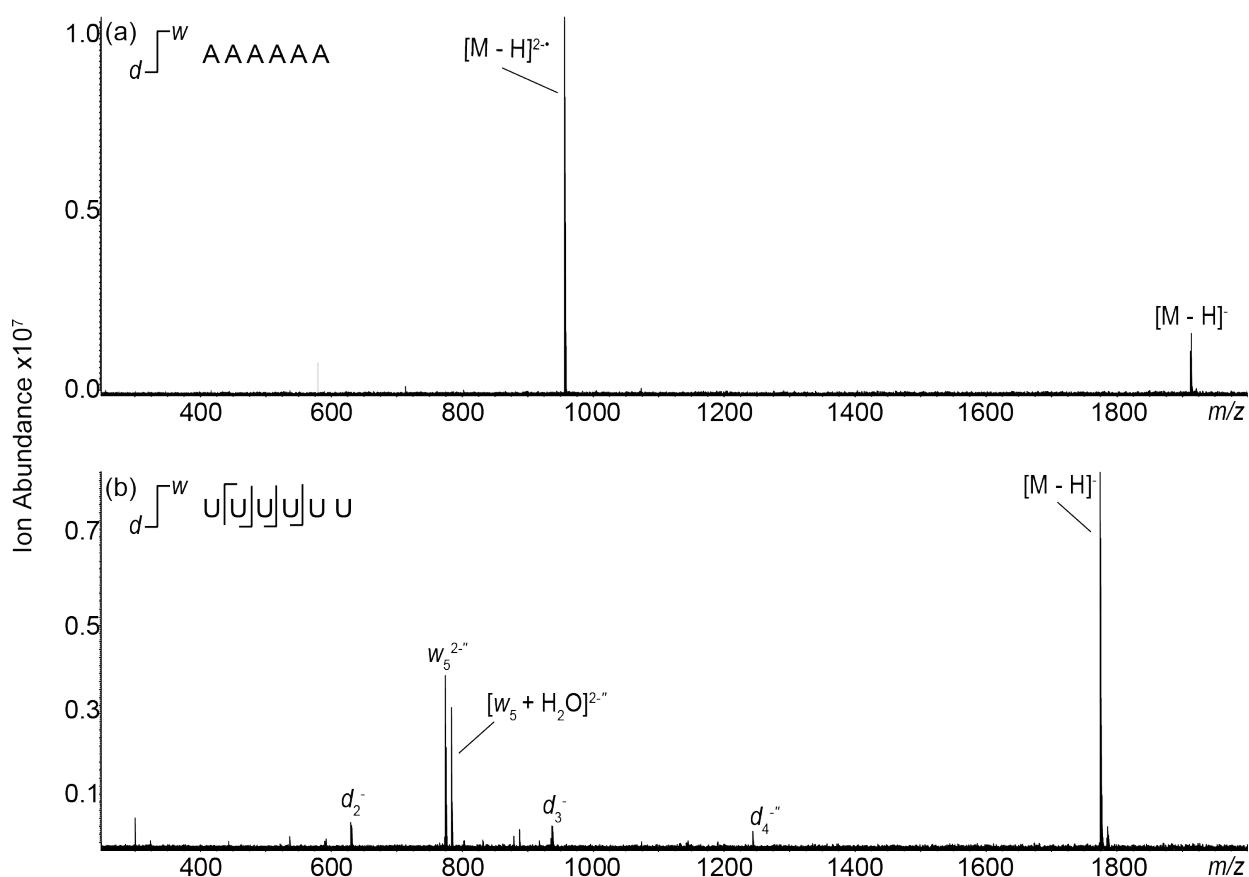


Figure 2.1. Representative niEC(D) spectra of the homopolymers (a) rA₆ and (b) rU₆.

In order to further investigate the nucleobase effect on electron capture behavior, single uridines were substituted for adenosine at different positions along the poly-uridine hexamer chain. Singly deprotonated rAUUUUU, rUUAUUU, and rUUUUUA were subjected to electron irradiation at 4.2-4.5 V cathode bias (Figure 2.2a-c). For all these sequences, charge increased electron capture species were observed at roughly the same or higher magnitude compared with the most abundant fragment ion. Because the polyU hexamer did not show a charge increased electron capture species, it appears that the presence of a single adenine has a profound effect on electron capture behavior.

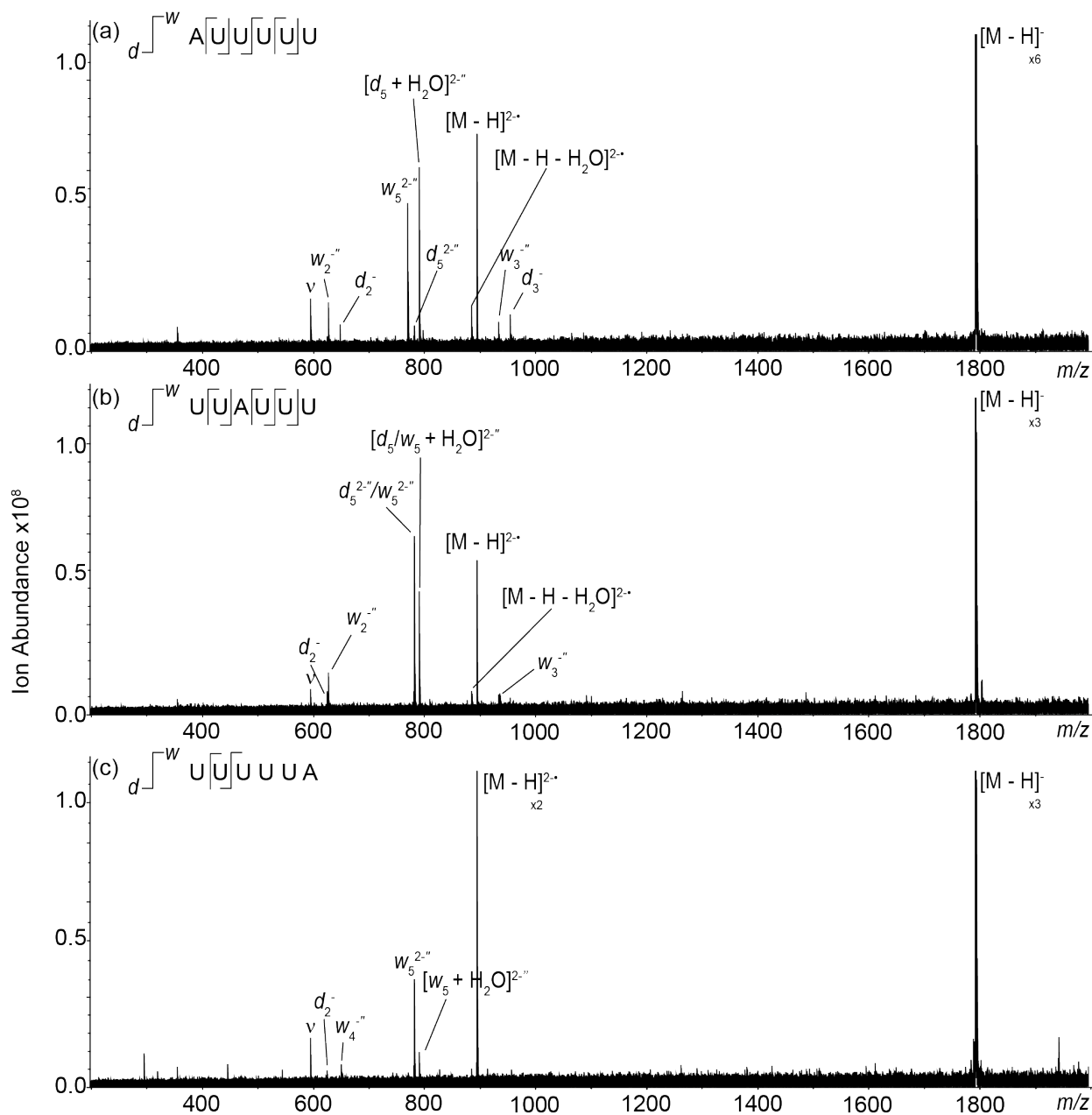


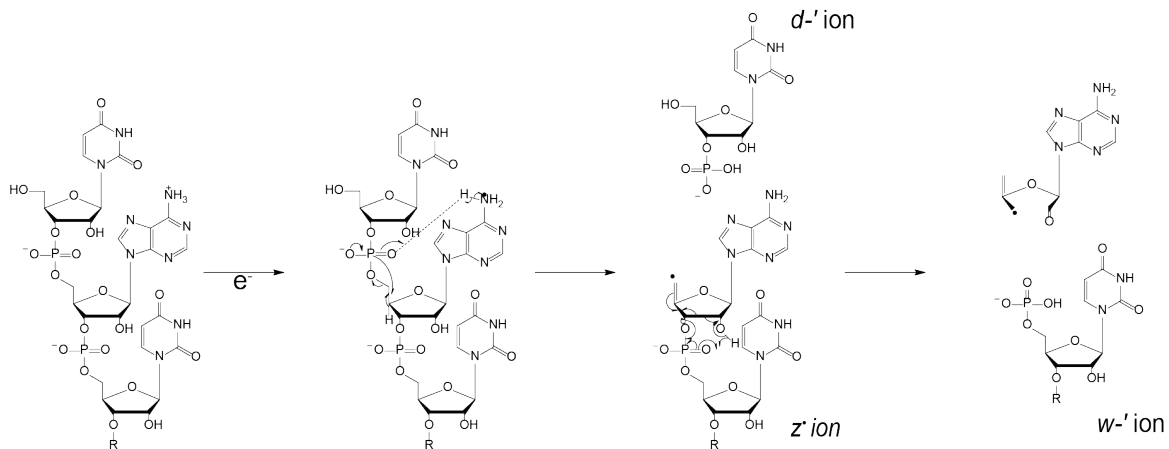
Figure 2.2. niECD of singly deprotonated (a) rAUUUUU, (b) rUUAUUU, and (c) rUUUUUA. Precursor anions were irradiated with 4.2–4.5 eV electrons for 5 seconds.

For the rAUUUUU hexamer, fragment ions include d_2^- , d_3^- and $d_5^{2--'}$ ions from the 5' terminus of the RNA sequence. w_2^- , w_3^- and $w_5^{2--'}$ ions from the 3' end are also observed. Full sequence coverage was obtained. niECD of rUUAUUU also resulted in full sequence coverage. For the latter hexamer, the d_5^- and w_5^- ions are isomeric and

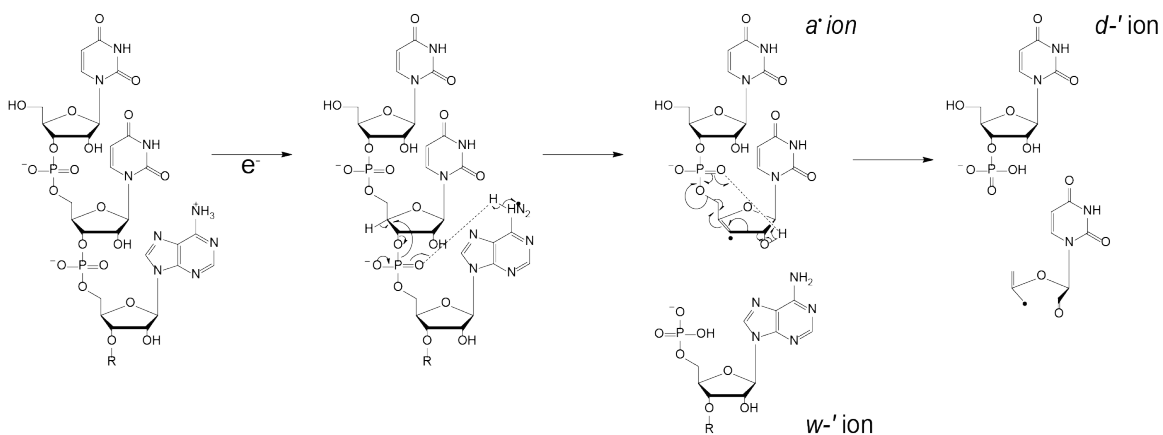
thus indistinguishable from one another. For rUUUUUA full sequence coverage was not obtained, however. Observed ions were d_2^- , w_4^{2-} and w_5^{2-} . The position of the adenine within the rAUUUUU and rUUAUUU sequences, respectively, did not have an effect on the niECD fragmentation behavior. Placing the adenine at the 3' end, however, reduced fragmentation compared with the other two sequences. Furthermore, the abundance of the electron capture species was significantly higher for the rUUUUUA sequence than for rAUUUUU and rUUAUUU, perhaps because a terminal adenosine can more easily hydrogen bond with a backbone phosphate group and thus prevent separation of product ion pairs.

Zwitterions are hypothesized to be a prerequisite for niECD to occur, i.e., in order for gas-phase anions to capture electrons, they must have a protonated site.²³ Nucleic acids have been shown to be zwitterionic in the gas phase with the phosphate backbones deprotonated and the nucleobases protonated.²⁵ In previous ECD (positive-ion mode) of nucleic acids, it was proposed that nucleobases are the primary sites of electron capture.^{18,19} Similar to positive-ion ECD,¹⁵ the major products observed in niECD are *d* and *w*-type ions. These data suggest that the niECD mechanism of fragmentation is ECD-like. We propose that the formation of *d* and *w* fragment ions is initiated by hydrogen radical migration from the protonated amine group of the adenine base to the phosphate moiety of closest proximity via gas-phase hydrogen bonding. Backbone fragmentation is further promoted in this rearranged radical species as shown in Schemes 2.1 and 2.2. For *d* ion formation (Scheme I) the O–C5' bond is cleaved, resulting in a pair of complementary *d'* and *z'* ions. However, because *z'* ions are not observed and are likely unstable, they further dissociate to yield an even-electron non-complementary *w* ion and a neutral radical. An alternative pathway for generation of semi-complementary *d* and *w* ions is shown in Scheme II where the O–C3' bond is cleaved, resulting in a complementary *w/a'* ion pair. The *a'* radical further dissociates into a *d* ion and a neutral radical species. Taucher and Breuker proposed a similar mechanism for the production of *d* and *w*-type ions in EDD.²² Formation of [$d_5 + H_2O$] ions upon electron irradiation of rAUUUUU, rUUAUUU and rUUUUUA is proposed to be due to an intramolecular hydrogen bond between the terminal 3' hydroxyl hydrogen and the neighboring neutral phosphate group (Scheme 2.3), similar to conventional ECD.¹⁵

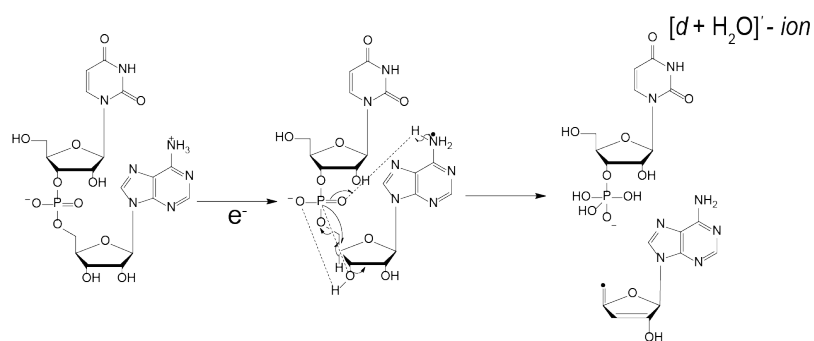
In the case of the mono-substituted sequences, the adenine is likely the site of electron capture as adenine has a higher proton affinity compared with uracil.⁴⁰



Scheme 2.1. Proposed mechanism for the formation of d' / w' ions in niECD.



Scheme 2.2. Proposed mechanism for the formation of w' / d' ions in niECD.



Scheme 2.3. Proposed mechanism for the formation of $[d + H_2O]^-$ ions in niECD.

2.3.2 Effect of Nucleobase Composition on Electron Capture and niECD Fragmentation Efficiency

To determine the optimum electron energy for the electron capture (and dissociation) process, singly deprotonated RNA homopolymers were irradiated with energies ranging from 0 to 20 eV and the niEC(D) efficiencies were calculated and plotted as a function of electron energy (Figure 2.3). The niEC(D) efficiencies were calculated as the ratio between the summed abundance of the charge-increased species ($[M - H]^{2-}$) plus any fragment ions and the precursor ion abundance prior to electron irradiation (all abundances were corrected for charge state):

$$\text{niEC(D) Efficiency} = \frac{\text{Abundance of } [M-H]^{2-} + \text{Abundance of Fragment Ions}}{\text{Abundance of } [M-H]^- \text{ Prior to Electron Irradiation}}$$

$$\text{niEC(D) Efficiency} = \frac{\text{Abundance of } [M-H]^{2-} + \text{Abundance of Fragment Ions}}{\text{Abundance of } [M-H]^- \text{ Prior to Electron Irradiation}} \quad (\text{Equation 2.1})$$

For rA_6 , maximum niEC(D) efficiency was achieved at 5.75 V cathode bias with a full width at half maximum (FWHM) of 1.02 eV. For rG_6 , rC_6 , and rU_6 , maximum electron capture efficiencies were achieved at 5.50, 5.25, and 5.25 V cathode bias, respectively. A comparison of these maximum efficiencies is shown in Figure 2.4a. All maximum electron capture efficiencies occur around 5.50 eV and the differences are within the FWHM, indicating that optimum electron irradiation energy does not have a significant

nucleobase dependence (Figure 2.4a). However, the base composition does indeed have an effect on the sequences' fragmentation behavior, as described above.

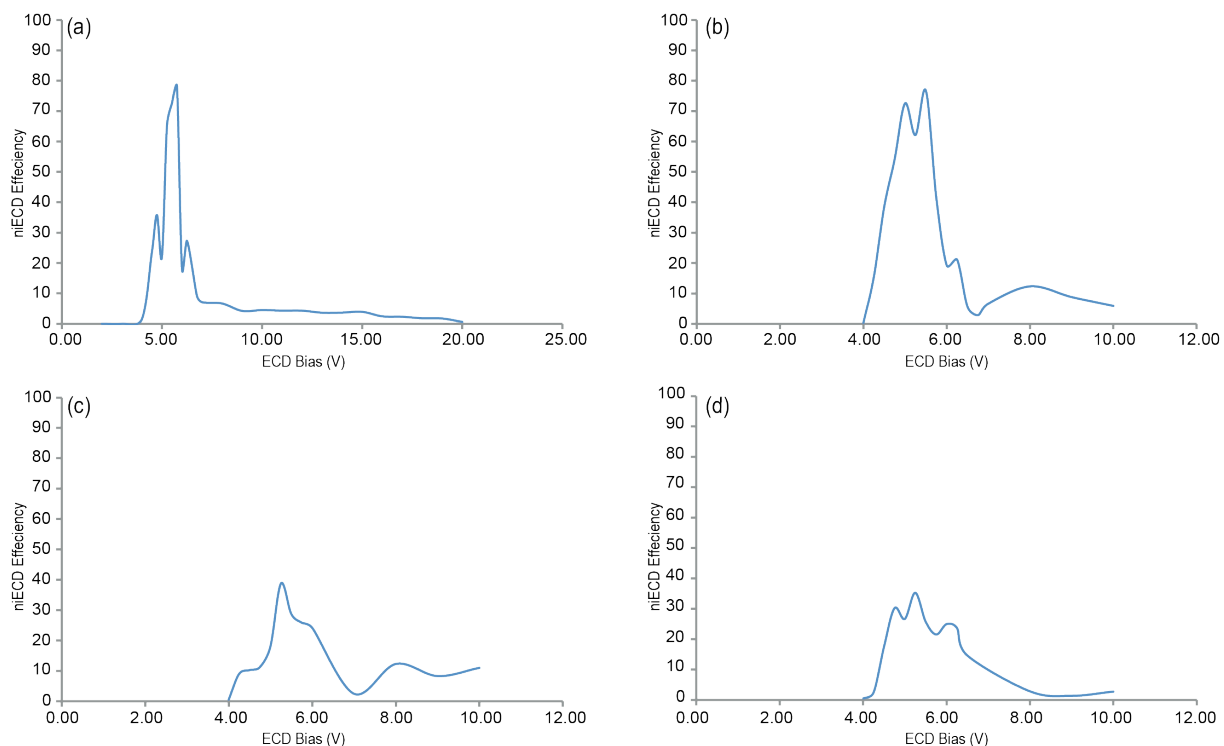


Figure 2.3. niEC(D) efficiency as a function of ECD cathode bias for the homopolymers (a) rA₆, (b) rG₆, (c) rC₆, and (d) rU₆. Data obtained on an Apex Q FT-ICR instrument (Bruker Daltonics, Billerica, MA).²⁷

In order to better understand the observed nucleobase dependence, electron capture efficiency, fragmentation efficiency, and overall niEC(D) efficiency were calculated and plotted as a function of sequence (**Figure 2.4b**). Electron capture efficiencies were calculated as the ratio between the abundance of the charge-increased species ($[M - H]^{2-\bullet}$) and the precursor ion abundance prior to electron irradiation (corrected for charge state):

$$\text{Electron-capture Efficiency} = \frac{\text{Abundance of } [M-H]^{2-\bullet}}{\text{Abundance of } [M-H]^- \text{ Prior to Electron Irradiation}}$$

$$\text{Electron-capture Efficiency} = \frac{\text{Abundance of } [M-H]^{2-\bullet}}{\text{Abundance of } [M-H]^- \text{ Prior to Electron Irradiation}} \quad (\text{Equation 2.2})$$

Fragmentation efficiencies were calculated as the ratio between the abundance of all fragment ions (d , d'' , $[d + H_2O]$, w and w'' ions) and the precursor ion abundance prior to electron irradiation (corrected for charge state):

$$\text{Fragmentation Efficiency} = \frac{\text{Abundance of Fragment Ions}}{\text{Abundance of } [M-H]^+ \text{ Prior to Electron Irradiation}}$$

$$\text{Fragmentation Efficiency} = \frac{\text{Abundance of Fragment Ions}}{\text{Abundance of } [M-H]^+ \text{ Prior to Electron Irradiation}} \quad (\text{Equation 2.3})$$

The oligonucleotides rA_6 and rG_6 showed niEC(D) efficiencies of 78% and 76%, respectively, with 0% fragmentation for both sequences. For rC_6 , the overall niEC(D) efficiency was 35% with the electron capture efficiency being 28%. Meanwhile, rU_6 showed an niEC(D) efficiency of 38% with an electron capture efficiency of 1%. A possible rationale for the higher niEC(D) efficiency of rA_6 and rG_6 is that purines are more likely to have zwitterionic structures in the gas phase because of their greater nucleobase proton affinities as compared to their pyridine counterparts.⁴⁰⁻⁴²

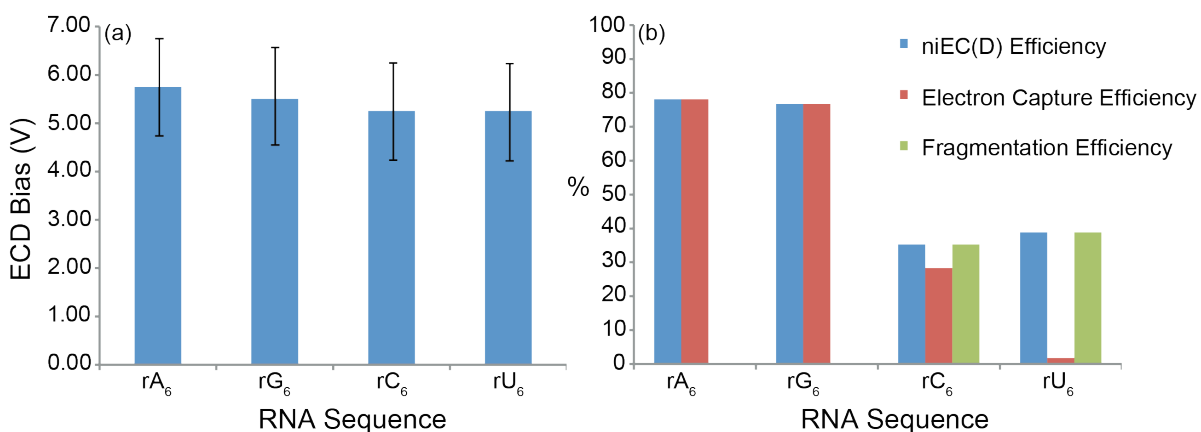


Figure 2.4. (a) Comparison of electron energies for which maximum electron capture efficiency was observed for rA_6 , rG_6 , rC_6 , and rU_6 . (b) niEC(D), electron capture, and fragmentation efficiencies calculated for each RNA oligonucleotide. Error bars correspond to half of the FWHM of the total energy distribution.

2.3.3 PTR-assisted niECD of RNA Hexamers and an 11-mer

Under typical negative ion mode electrospray conditions, a single charge state distribution spanning the 2- to 5- charge states is observed for the RNA hexamer rGCAUAC (Figure 2.5). Singly deprotonated RNA is not observed.

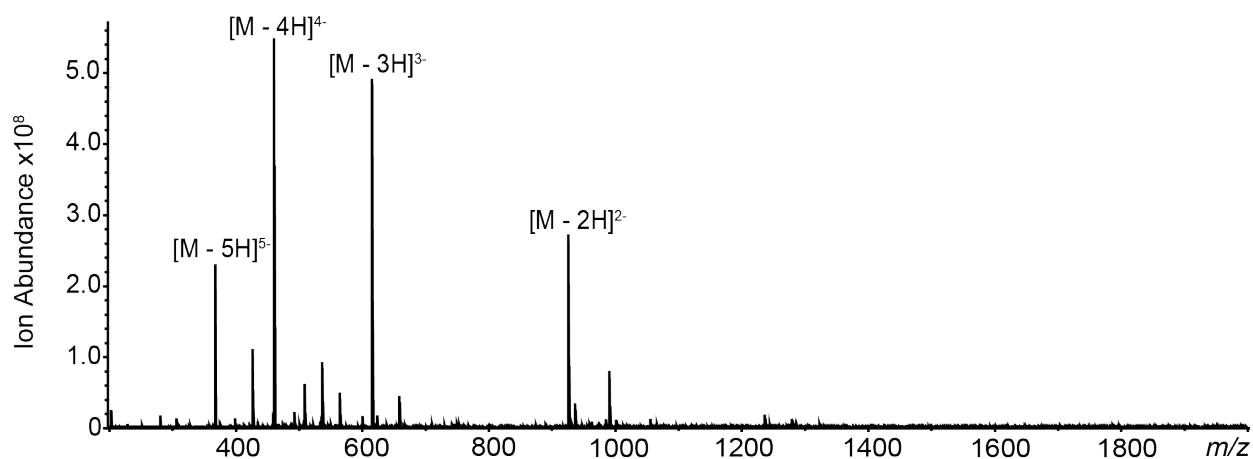


Figure 2.5. Negative-ion mode electrospray mass spectrum of rGCAUAC.

The doubly deprotonated rGCAUAC species was quadrupole isolated and subjected to electron irradiation (6.0 V cathode bias) for 5 seconds. No electron capture was observed (Figure 2.4a). We hypothesize that, at the m/z value of the 2- charge state, the total charge density is too high for favorable electron capture.

In order to reduce the charge density of rGCAUAC, protonated fluoranthene ions were reacted with the doubly deprotonated oligonucleotide in the collision cell for 3 seconds. As shown in Figure 2.6b, the 2- charge state is depleted and a charge reduced singly deprotonated species is formed. This 1- species was then isolated in the ICR cell and subjected to electron irradiation under similar conditions as the doubly deprotonated species. As shown in Figure 2.6c, the electron capture species $[M - H]^{2-}$ is observed in addition to two sequence informative fragments, d_5^{2-} and w_4^- .

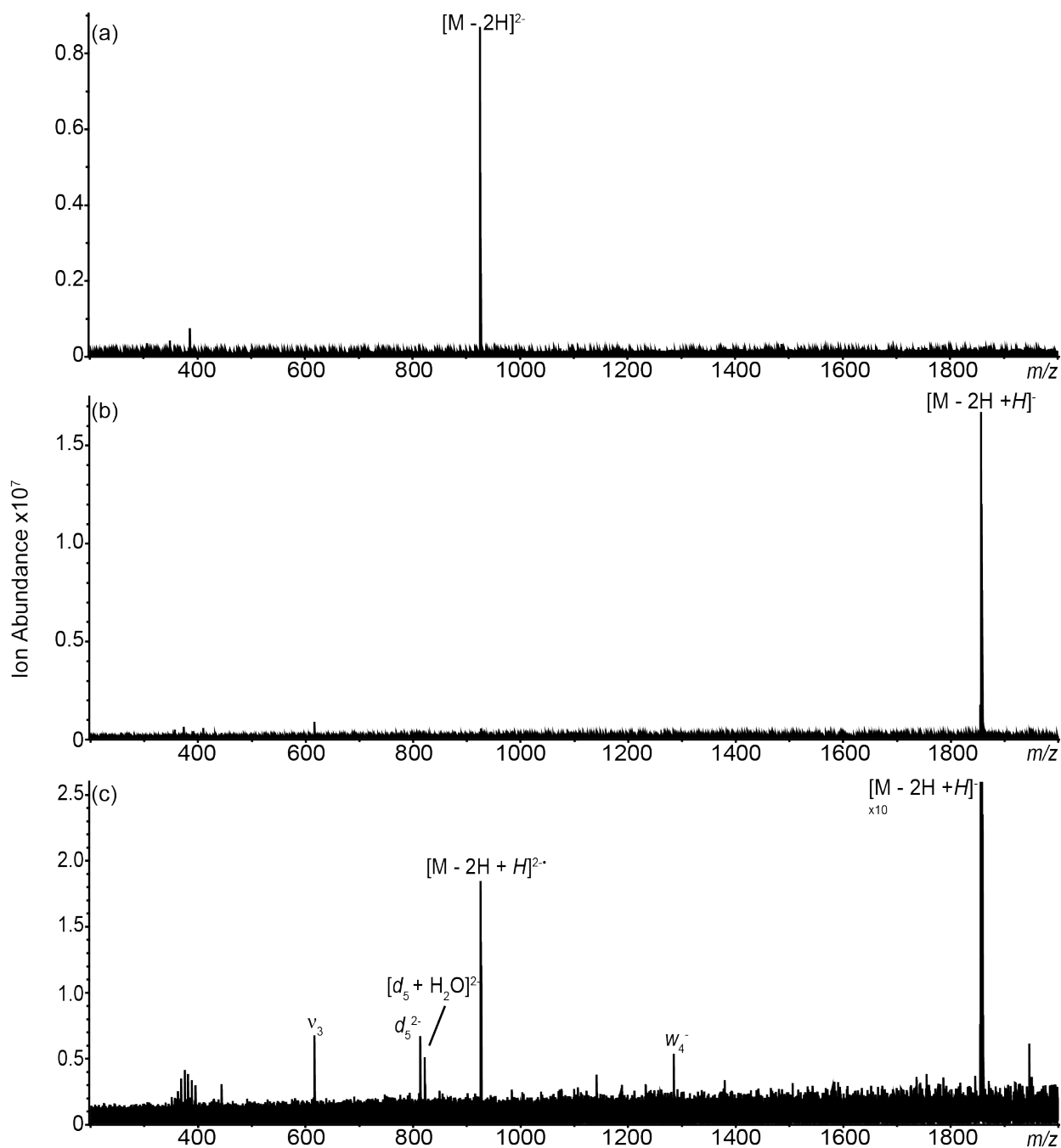


Figure 2.6. (a) niECD spectrum of doubly deprotonated rGCAUAC, 6.0 V cathode bias for 5 seconds, (b) PTR of doubly deprotonated rGCAUAC, (c) PTR-niECD of in-cell isolated singly deprotonated rGCAUAC.

As RNA molecules become larger, more negative charge is present due to the increasing number of phosphates. As a result, it becomes increasingly difficult to generate low charged RNA species. As shown in Figure 2.7, an electrospray mass

spectrum of an 11-mer oligonucleotide contains charge states spanning from 3- to 8- with the 6- charge state being most abundant.

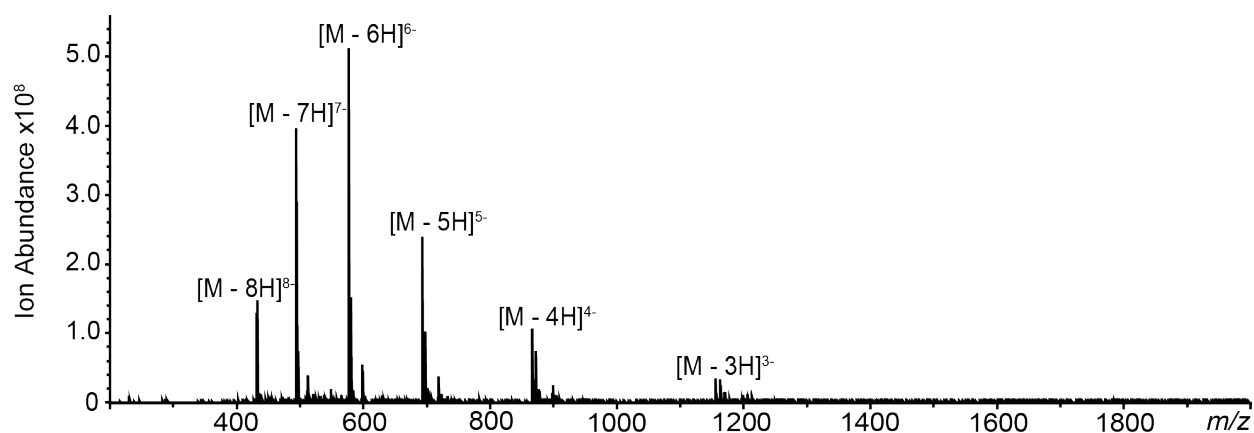


Figure 2.7. Negative-ion mode ESI mass spectrum of an 11-mer RNA oligonucleotide, rUAACUAUGACG.

The triply deprotonated species was isolated in the quadrupole and subjected to electron irradiation under similar conditions as the hexamers above (6.0 V cathode bias, 5 seconds). Electron capture was not observed upon exposure to electrons as shown in Figure 2.8a. Proton transfer to the same triply deprotonated species resulted in a charged reduced 2- charge state (Figure 2.8b). This 2- charge state was then subjected to electron irradiation and an electron capture species was observed (Figure 2.6c). These results further support the hypothesis that, as charge density increases, the probability of electron-capture decreases rapidly. Hence, PTR is a useful analytical tool to reduce the charge of highly charged species and facilitate or improve niECD performance.

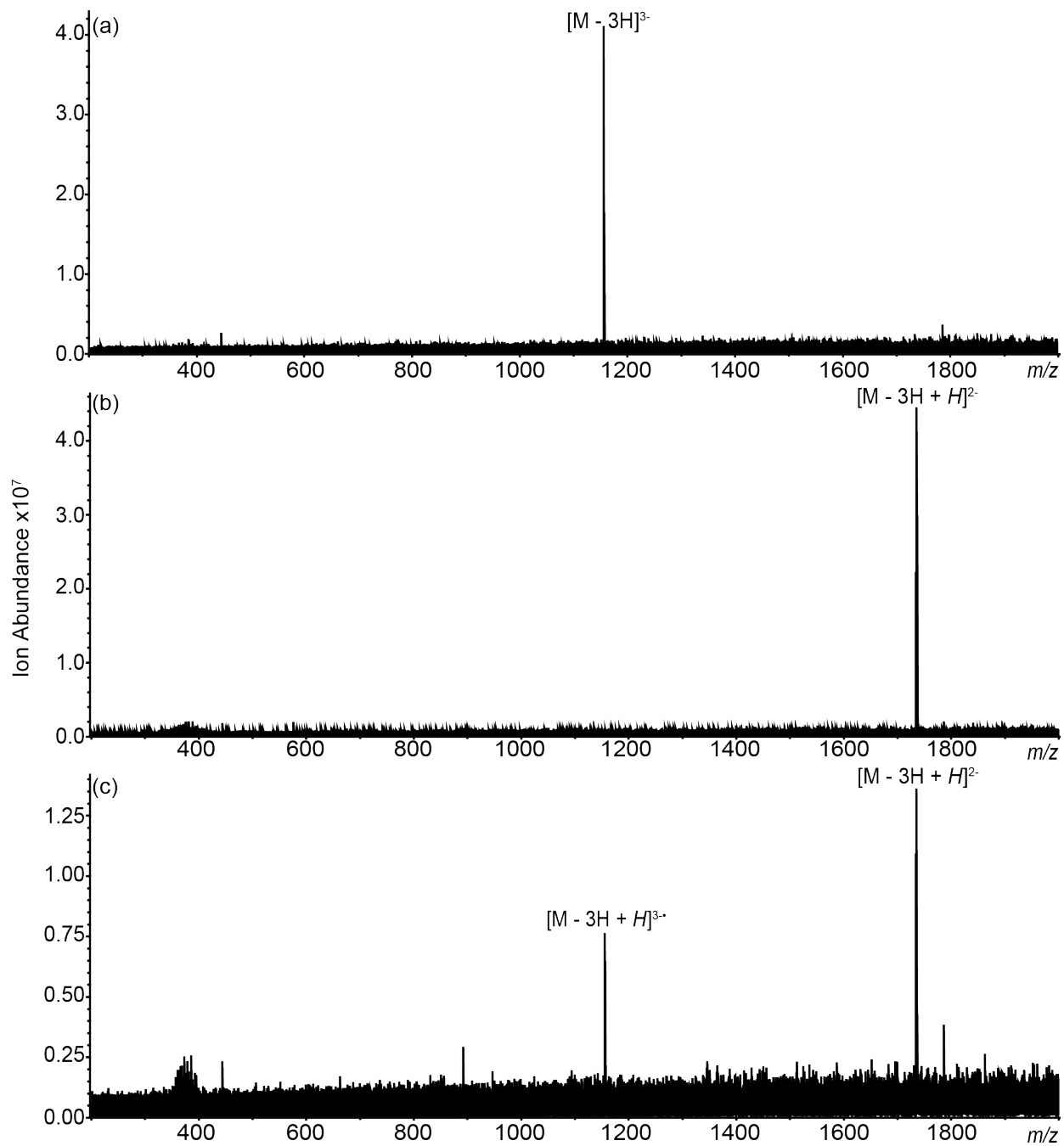


Figure 2.8. (a) niECD spectrum of a triply deprotonated 11-mer, 6.0 V cathode bias for 5 seconds, (b) PTR of the triply deprotonated 11-mer, (c) PTR-niECD of in-cell isolated doubly deprotonated 11-mer.

2.4 Conclusion

Electron irradiation of anionic RNA oligonucleotides produces charge-increased radical ions, that undergo a radical driven fragmentation process. Purine-containing homopolymers captured electrons to yield stable charge increased radical species ($[M - H]^{2-\bullet}$), with no fragmentation observed. By contrast, pyrimidine-containing homopolymers produced charge-increased species at lower (~50%) ion abundances and more extensive fragmentation was observed. Purines form stable intramolecular salt bridges, that can prevent fragmentation.³⁹ Supplemental activation may therefore be necessary to promote fragmentation of purine-containing oligonucleotides. Incorporating single adenosines within a polyU chain increases the yield of the charge-increased species, indicating that purine-containing oligonucleotides form more stable radicals than uridine-containing ones. The latter data suggest that intramolecular interactions may not be the only factor in stabilizing purine-containing sequences. Characteristic “ECD-like” radical fragment ions suggest similarities between niECD and positive ion ECD due to RNA zwitterionic structures in negative ion mode. We propose that niECD proceeds via hydrogen radical migration from the electron capture site, on a nucleobase, to the phosphate backbone at which fragmentation occurs. The resulting hydrogen migration results in semi-complementary d' and/or w' ion pairs. PTR reduces the overall charge of gas-phase RNA species, thus reducing total charge density and promoting electron capture. PTR-niECD shows promise for top-down analysis of larger RNA molecules or analysis of “native-like” charge states.

2.5 References

- (1) Cooper, T. A.; Wan, L.; Dreyfuss, G. RNA and disease. *Cell* **2009**, *136*, 777-793.
- (2) Bothe, J. R.; Nikolova, E. N.; Eichhorn, C. D.; Chugh, J.; Hansen, A. L.; Al-Hashimi, H. M. Characterizing RNA dynamics at atomic resolution using solution-state NMR spectroscopy. *Nat. Methods* **2011**, *8*, 919-931.
- (3) Al-Hashimi, H. M. Dynamics-based amplification of RNA function and its characterization by using NMR spectroscopy. *ChemBioChem*. **2005**, *6*, 1506-1519.
- (4) Rueda, D.; Bokinsky, G.; Rhodes, M. M.; Rust, M. J.; Zhuang, X.; Walter, N. G. Single-molecule enzymology of RNA- Essential functional groups impact catalysis from a distance. *PNAS* **2004**, *101*, 10066-10071.

- (5) Schurch, S. Characterization of Nucleic Acids by Tandem Mass Spectrometry - The Second Decade (2004-2013): From DNA to RNA and Modified Sequences. *Mass Spectrom. Rev.* **2016**, *35*, 483-523.
- (6) Smith, S. I.; Brodbelt, J. S. Characterization of Oligodeoxynucleotides and Modifications by 193 nm Photodissociation and Electron Photodetachment Dissociation. *Anal. Chem.* **2010**, *82*, 7218-7226.
- (7) Wu, J.; McLuckey, S. A. Gas-phase Fragmentation of Oligonucleotide Ions. *Int. J. Mass. Spectrom.* **2004**, *237*, 197-241.
- (8) Wan, K. X.; Gross, J.; Hillenkamp, F.; Gross, M. L. Fragmentation Mechanisms of Oligodeoxynucleotides Studied by H/D Exchange and Electrospray Ionization Tandem Mass Spectrometry. *J. Am. Soc. Mass Spectrom.* **2001**, *12*, 193-205.
- (9) Wan, K. X.; Gross, M. L. Fragmentation Mechanisms of Oligodeoxynucleotides: Effects of Replacing Phosphates with Methylphosphonates and Thymines with Other Bases in T-rich Sequences. *J. Am. Soc. Mass Spectrom.* **2001**, *12*, 580-589.
- (10) Harper, B.; Neumann, E. K.; Solouki, T. DNA Oligonucleotide Fragment Ion Rearrangements Upon Collision-Induced Dissociation. *J. Am. Soc. Mass Spectrom.* **2015**, *26*, 1404-1413.
- (11) Huang, T. Y.; Kharlamova, A.; Liu, J.; McLuckey, S. A. Ion Trap Collision-induced Dissociation of Multiply Deprotonated RNA: c/y-ions versus (a-B)/w-ions. *J. Am. Soc. Mass Spectrom.* **2008**, *19*, 1832-1840.
- (12) Schneeberger, E. M.; Breuker, K. Native Top-Down Mass Spectrometry of TAR RNA in Complexes with a Wild-Type tat Peptide for Binding Site Mapping. *Angew. Chem. Int. Ed.* **2017**, *56*, 1254-1258.
- (13) Huang, T.; Liu, J.; Liang, X.; Hodges, B. D. M.; McLuckey, S. A. Collision-Induced Dissociation of Intact Duplex and Single-Stranded siRNA Anions. *Anal. Chem.* **2008**, *80*, 8501-8508.
- (14) Monn, S. T.; Schurch, S. New Aspects of the Fragmentation Mechanisms of Unmodified and Methylphosphonate-modified Oligonucleotides. *J. Am. Soc. Mass Spectrom.* **2007**, *18*, 984-990.
- (15) Hakansson, K.; Hudgins, R. R.; O'Hair, R. A. J.; Marshall, A. G. Electron Capture Dissociation and Infrared Multiphoton Dissociation of Oligodeoxynucleotide Dications. *J. Am. Soc. Mass Spectrom.* **2003**, *14*, 23-41.
- (16) Schultz, K. N.; Håkansson, K. Rapid electron capture dissociation of mass-selectively accumulated oligodeoxynucleotide dications. *Int. J. Mass Spectrom.* **2004**, *234*, 123-130.
- (17) Yang, J.; Mo, J.; Adamson, J. T.; Hakansson, K. Characterization of Oligodeoxynucleotides by Electron Detachment Dissociation Fourier Transform Ion Cyclotron Resonance Mass Spectrometry. *Anal. Chem.* **2005**, *77*, 1876-1882.
- (18) Yang, J.; Hakansson, K. Fragmentation of oligoribonucleotides from gas-phase ion-electron reactions. *J. Am. Soc. Mass Spectrom.* **2006**, *17*, 1369-1375.
- (19) Chan, T. W.; Choy, M. F.; Chan, W. Y.; Fung, Y. M. A Mechanistic Study of the Electron Capture Dissociation of Oligonucleotides. *J. Am. Soc. Mass Spectrom.* **2009**, *20*, 213-226.

- (20) Krivos, K. L.; Limbach, P. A. Sequence Analysis of Peptide: Oligonucleotide Heteroconjugates by Electron Capture Dissociation and Electron Transfer Dissociation. *J. Am. Soc. Mass. Spectrom.* **2010**, *21*, 1387-1397.
- (21) Taucher, M.; Breuker, K. Characterization of modified RNA by top-down mass spectrometry. *Angew Chem. Int. Ed. Engl.* **2012**, *51*, 11289-11292.
- (22) Taucher, M.; Breuker, K. Top-down mass spectrometry for sequencing of larger (up to 61 nt) RNA by CAD and EDD. *J. Am. Soc. Mass Spectrom.* **2010**, *21*, 918-929.
- (23) Yoo, H. J.; Wang, N.; Zhuang, S.; Song, H.; Hakansson, K. Negative-ion electron capture dissociation: radical-driven fragmentation of charge-increased gaseous peptide anions. *J. Am. Chem. Soc.* **2011**, *133*, 16790-16793.
- (24) Hersberger, K. E.; Hakansson, K. Characterization of O-sulfopeptides by negative ion mode tandem mass spectrometry: superior performance of negative ion electron capture dissociation. *Anal. Chem.* **2012**, *84*, 6370-6377.
- (25) Gidden, J.; Bowers, M. T. Gas-Phase Conformations of Deprotonated Trinucleotides (dGTT⁻, dTGT⁻, and dTTG⁻): The Question of Zwitterion Formation. *J. Am. Soc. Mass Spectrom.* **2003**, *14*, 161-170.
- (26) Guo, X.; Bruist, M. F.; Davis, D. L.; Bentzley, C. M. Secondary Structural Characterization of Oligonucleotide Strands Using Electrospray Ionization Mass Spectrometry. *Nucleic Acids Res.* **2005**, *33*, 3659-3666.
- (27) Song, H., Ph.D. Dissertation, University of Michigan, 2011.
- (28) Cheng, X.; Gale, D. C.; Udseth, H. R.; Smith, R. D. Charge State Reduction of Oligonucleotide Negative Ions from Electrospray Ionization. *Anal. Chem.* **1995**, *67*, 586-593.
- (29) Muddiman, D. C.; Cheng, X.; Udseth, H. R.; Smith, R. D. Charge-State Reduction with Improved Signal Intensity of Oligonucleotides in Electrospray Ionization Mass Spectrometry. *J. Am. Soc. Mass Spectrom.* **1996**, *7*, 697-706.
- (30) Herron, W. J.; Goeringer, D. E.; McLuckey, S. A. Ion-ion Reactions in the Gas Phase: Proton Transfer Reactions of Protonated Pyridine with Multiply Charged Oligonucleotide Anions. *J. Am. Soc. Mass Spectrom.* **1995**, *6*, 529-532.
- (31) Stephenson, J. L.; McLuckey, S. A. Ion/Ion Proton Transfer Reactions for Protein Mixture Analysis. *Anal. Chem.* **1996**, *68*, 4026-4032.
- (32) Martens, J.; Berden, G.; Oomens, J. Structures of Fluoranthene Reagent Anions Used in Electron Transfer Dissociation and Proton Transfer Reaction Tandem Mass Spectrometry. *Anal. Chem.* **2016**, *88*, 6126-6129.
- (33) Holden, D. D.; Brodbelt, J. S. Ultraviolet Photodissociation of Native Proteins Following Proton Transfer Reactions in the Gas Phase. *Anal. Chem.* **2016**, *88*, 12354-12362.
- (34) Holden, D. D.; McGee, W. M.; Brodbelt, J. S. Integration of Ultraviolet Photodissociation with Proton Transfer Reactions and Ion Parking for Analysis of Intact Proteins. *Anal. Chem.* **2016**, *88*, 1008-1016.
- (35) Laszlo, K. J.; Munger, E. B.; Bush, M. F. Folding of Protein Ions in the Gas Phase after Cation-to-Anion Proton-Transfer Reactions. *J. Am. Chem. Soc.* **2016**, *138*, 9581-9588.
- (36) Laszlo, K. J.; Buckner, J. H.; Munger, E. B.; Bush, M. F. Native-Like and Denatured Cytochrome c Ions Yield Cation-to-Anion Proton Transfer Reaction

- Products with Similar Collision Cross-Sections. *J. Am. Soc. Mass Spectrom.* **2017**, *28*, 1382-1391.
- (37) Laszlo, K. J.; Munger, E. B.; Bush, M. F. Effects of Solution Structure on the Folding of Lysozyme Ions in the Gas Phase. *J. Phys. Chem. B.* **2017**, *121*, 2759-2766.
- (38) Kjeldsen, F.; Haselmann, K. F.; Budnik, B. A.; Jensen, F.; Zubarev, R. A. Dissociative capture of hot (3–13 eV) electrons by polypeptide polycations- an efficient process accompanied by secondary fragmentation. *Chem. Phys. Lett.* **2002**, *356*, 201-206.
- (39) Green-Church, K. B.; Limbach, P. A.; Freitas, M. A.; Marshall, A. G. Gas-phase Hydrogen:deuterium Exchange of Positively Charged Mononucleotides by use of Fourier-transform Ion Cyclotron Resonance Mass Spectrometry. *J. Am. Soc. Mass Spectrom.* **2000**, *12*, 268-277.
- (40) Hunter, E. P. L.; Lias, S. G. Evaluated Gas Phase Basicities and Proton Affinities of Molecules: An Update. *J. Phys. and Chem. Ref. Data* **1998**, *27*, 413-656.
- (41) Wolken, J. K.; Turecek, F. Proton Affinity of Uracil. A Computational Study of Protonation Sites. *J. Am. Soc. Mass Spectrom.* **2000**, *11*, 1065-1071.
- (42) Green-Church, K. B.; Limbach, P. A. Mononucleotide Gas-Phase Proton Affinities as Determined by the Kinetic Method. *J. Am. Soc. Mass Spectrom.* **2000**, *11*, 24-32.

Chapter 3

Traveling-wave Ion Mobility Mass Spectrometry and Molecular Dynamic Simulations Reveal the Effects of Solution on a Gas-phase RNA Hairpin and its Small Molecule Complexes

3.1 Introduction

Ribonucleic acids (RNAs) are involved in key functions in all living cells, including coding (and decoding), regulation, and expression of genes. For RNAs to perform their various cellular functions, they form complexes with proteins, other RNA/DNAs, and small molecules. RNA molecules must adopt specific secondary folds to form complexes with other molecules. RNA misfolding has been linked to neurodegenerative disorders such as Hutchinson's and Alzheimer's disease.^{1,2} For these reasons, RNA has been the target of new therapeutics.³ RNA hairpins constitute the major secondary structure amongst RNAs. Proper hairpin folds are essential for a variety of functions: ribozyme activity, protection of messenger RNA (mRNA), and recognition by proteins in the cell, to name a few.⁴⁻⁷ Thus, it is vital to develop analytical techniques that can probe RNA higher order structure and RNA interaction sites.

Electrospray ionization (ESI), being a "soft" ionization technique has the ability of preserving non-covalent interactions during the transfer from solution to gas phase, thus fully or partially preserving higher order structure.⁸⁻¹⁵ RNA complexes, such as RNA-DNA, RNA-protein, and RNA-small molecule complexes can also be conserved in a solvent free environment.¹⁶⁻²¹ For this reason, ESI-mass spectrometry (MS) is widely used in multiplexing analyses for potential drug targets and corresponding drug candidates.²² Mass spectrometry is also a powerful technique used to probe interaction sites within RNA complexes. Because of the negatively charged phosphate backbone of RNA, operation in negative-ion mode is favored. Breuker and co-workers have shown

the utility of negative-ion mode collision-induced dissociation (CID) to elucidate interaction sites in RNA-peptide complexes.¹⁷ Electron based techniques such as electron detachment dissociation (EDD)²³ and negative-ion electron capture dissociation (niECD)^{24,25} provide complementary sequence informative fragments compared with the aforementioned CID technique. niECD may be particularly suited for probing structured RNAs due to its requirement for low charge-state species. Nucleic acids has been shown to be more “native-like” at lower charge states.²⁶ Coulomb repulsion at higher charge states leads to much more extended or denatured gas-phase structures. The drawback of electron based fragmentation techniques, however, is the low fragmentation efficiencies. One way to circumvent this drawback is to ensure that there is sufficient precursor ion abundances by varying ESI solvent content.

Conventional electrospray solutions include organic solvents (typically at a concentration of 50/50, vol/vol), such as methanol, isopropyl alcohol, or acetonitrile. Such organic solvents are utilized because of their ability to lower surface tension of the solution, thus aiding the ESI process.^{27,28} High concentrations of organic additives, however, have been shown to denature nucleic acid secondary structure,²⁹⁻³¹ making probing RNA native structure by mass spectrometry difficult. Spraying from physiological ionic strength environments (i.e., >100 mM ammonium acetate) has been shown to maintain native structure through the desolvation process.³² Potential RNA targets require proper secondary and tertiary folds for function and thus their structural characterization is of utmost importance. Spectral quality, however, is often compromised because of the high salt concentration suppressing ion signal,³³ which becomes problematic when attempting to employ MS/MS techniques, particularly for relatively low efficiency processes.

Ion-mobility mass spectrometry (IM-MS) is a powerful technique for determining overall size and conformation of nucleic acid complexes in gas-phase measurements.^{10,34-40} Because mass spectrometers operate in vacuum, it is essential to first understand the correlation between RNA solution conditions and gas-phase structure. This Chapter combines traveling-wave IM-MS (TWIMS) and replica-exchange molecular dynamics (REMD) simulations to investigate structural effects of ESI solution content on a model RNA hairpin, a bacterial ribosomal RNA A-site construct (16S). This

particular 27-nt RNA model has been extensively studied in the literature and, therefore, serves as an ideal model system for understanding solvent effects on gaseous RNA hairpin structure.⁴¹⁻⁴⁹ Also, we employ mass spectrometric competitive ligand binding assays as a function of solution content to explore the effects of solvent on binding site specificity.

3.2 Experimental

3.2.1 Reagents

Calibrant proteins insulin, cytochrome c, β -lactoglobulin and ubiquitin were purchased from Sigma-Aldrich (St. Louis, MO). Prior to mass spectrometry analysis, protein samples were diluted to 10–15 μ M in 100–200 mM NH_4OAc as previously described by Bush and co workers.⁵⁰ RNA oligonucleotides were purchased from Integrated DNA Technologies (Coralville, IA). Prior to analysis, dried 16S RNA model (GGCGUCACACCUUCGGGUGAAGUCGCC), and modified 16S sequence (Δ 1492A) (GGCGUCACACCUUCGGGUGAGUCGCC) samples were re-suspended in water at concentrations of 100 μ M. RNA samples were desalted by ethanol precipitation.¹² Prior to analysis, samples were annealed by heating at 95°C and allowed to cool on ice. Samples were analyzed at final concentrations of 1–5 μ M in 10-100 mM NH_4OAc . The aminoglycoside antibiotics paromomycin (PM), kanamycin B (BK), apramycin (AP), and ribostamycin (RM) were purchased from Sigma-Aldrich (St. Louis, MO).

3.2.2 Traveling Wave Mass Spectrometry

Protein calibrants were analyzed on a quadrupole ion-mobility time-of-flight mass spectrometer (The Synapt (G1) HDMS, Waters Corporation, Milford, MA). Negatively charged gaseous ions were generated via a nano-electrospray (nESI) source. A capillary voltage of 1.3 kV was applied with a cone voltage of 40 V. The T-wave mobility region was operated at an IMS wave height of 10.0 V and IMS wave velocity of 250 m/s. The instrument was calibrated for experimental CCS measurements based on

previously described protocols.⁵¹ Briefly, the arrival times were recorded by DriftScope (Waters Corporations, Milford, MA) and extracted by fitting the arrival time distributions via a Gaussian distribution function (OriginPro). Arrival time distributions were corrected for their m/z dependent flight time and the corresponding literature CCS values were corrected for charge and mass. A logarithmic plot of the corrected CCS plotted as a function of corrected arrival times generates a linear regression calibration curve. CCS_{EXP} values for the 16S RNA ions were estimated by fitting arrival times of such ions to the calibration curve.

3.2.3 Circular Dichroism Spectroscopy

Circular dichroism (CD) spectra were obtained on a Jasco CD Spectropolarimeter from 220 to 320 nm at 50 nm/min.

3.2.4 Molecular Modeling

3.2.4.1 Replica-Exchange Molecular Dynamics Simulations

Gas-phase Replica Exchange Molecular Dynamics (REMD)⁵² simulations of the ribosomal A-site RNA (PDB ID - 1A3M) were carried out at different charge states. Net charges ranging from 5- to 9- were assigned via an in-house R script to the model 1 of the 27-mer NMR decoy of the RNA structure following Orozco and co-workers.⁵³ REMD simulations for the structures at each of the charge states were performed with the ENSEMBLE module implemented in the molecular modeling suite CHARMM.⁵⁴ The CHARMM36 nucleic acid force field was used.⁵⁵

In REMD, multiple simulations of a molecular system are run at different temperatures in replicate. The success rate of temperature exchange between two replicas, i and j , is evaluated based on a Metropolis Monte Carlo move with the exchange probability:

$$p_{i,j} = \min \{1, e^{-(\beta_i - \beta_j)(E_j - E_i)}\} \quad (\text{Equation 3.1})$$

In which $\beta = 1/k_B T$, k_B is the Boltzmann constant, T is the absolute temperature, and E is the potential energy.¹ For an allowed exchange, the temperatures between the replicas are swapped and the velocities of each replica are assigned by applying the scaling factor $(T_{new}/T_{old})^{1/2}$, where T_{old} and T_{new} are the temperatures before and after exchange, respectively. In our study, 100 ns REMD calculations were carried out at 10 different temperature (T) windows at $T = 280.0, 300.0, 320.0, 340.0, 360.0, 380.0, 400.0, 420.0, 440.0$ and 460.0 K with an attempt to exchange temperature every 100 ps. The average exchange ratio ranged from 0.13 to 0.16. Prior to starting the REMD simulations, structures were energy-minimized by 100 steps of Steepest Descent (SD) method followed by 100 steps of Adopted Basis Newton-Raphson (ABNR) method with minimization step size of 0.005 and harmonic restraints, applying a force constant of $10 \text{ kcal/mol/\AA}^2$, on the heavy atoms. Infinite cutoff was used to generate the non-bonded atom pair list. Trajectories were propagated with a time step of 2 fs and snapshots were saved every 100 ps.

3.4.2.2 Clustering Analysis

Clustering analyses were conducted for the 1000 snaps saved from the 300 K trajectory. The K-means clustering algorithm, implemented in the Multiscale Modeling Tools for Structural Biology (MMTSB) interface, was used with K-means radius of 3.0 \AA and selecting the heavy atoms only.⁵⁶ RMSD based clusters of structures were generated after least-square superposition. Theoretical CCS values were calculated via the IMoS software using the trajectory method algorithm.⁵⁷

3.2.5 Competitive Ligand Binding K_D Measurements

Aminoglycoside concentration ranged from 100 nM to 2 \mu M with a constant RNA concentration of 1 \mu M . RNA/ligand complexes were directly infused via an ESI ionization source into a 7-Tesla Q-FT-ICR mass spectrometer (SolariX, Bruker Daltonics, Billerica, MA). The spectra were results of a co-addition of 32 scans. K_D values for the RNA/ligand complexes were calculated by measuring the relative peak

magnitudes of the free RNA to the RNA ligand complex within a given mass spectrum (all peaks with mass spectrum were normalized for charge).^{58,59} The equilibrium binding of A (RNA) and a single B (a ligand/aminoglycoside) is given by:



$$R = \frac{[AB]_{\text{eq}}}{[A]_{\text{eq}}} \quad (\text{Equation 3.3})$$

in which R is the equilibrium ratio between the bound form of the RNA when interacting with B and the free RNA. We assume that the spray and detection efficiencies are the same for all species. As a result, R must be equivalent to the ratio of the concentration in solution at equilibrium. The equilibrium concentration, $[AB]_{\text{eq}}$, can be determined from the value of R and $[A]_0$ (or the initial RNA concentration) using Equation 3.4. K_D values are then readily calculated from ESI mass spectra using Equation 3.5:

$$[AB]_{\text{eq}} = \frac{R[A]_0}{1+R} \quad (\text{Equation 3.4})$$

$$K_D = \frac{[A]_{\text{eq}}([B]_0 - [AB]_{\text{eq}})}{[AB]_{\text{eq}}} \quad (\text{Equation 3.5})$$

3.3 Results and Discussion

3.3.1 Solvent Effects on A-site Conformation

Canonical Watson-Crick (GC and AU) and non-canonical (GU) base pairing form RNA secondary structure. Base pairing is a thermodynamically driven process that results from hydrogen bonding between complementary bases. There are several factors that influence the stability of such interactions, including ionic strength of the buffer solution, organic solvent content, and pH. Increasing the salt concentration (which increases ionic strength of buffer solutions) helps stabilize RNA secondary structure due to

shielding of the electrostatic repulsion between negatively charged phosphate groups of adjacent nucleotides. Physiological buffer solutions include Na^+ , K^+ , Mg^{2+} , and Cl^- salts at the 10^{-1} M range.^{32,60,61} Because of their non-volatility, such salts are not suitable for ESI-MS analysis. Because of its volatility, ammonium acetate (NH_4OAc) buffer is typically used as a substitute.

We first examined the effect of ionic strength on both RNA conformation and mass spectral quality (Figure 3.1). Increasing the NH_4OAc concentration to 100 mM has a drastic effect on spectral quality as the resulting mass spectrum is dominated by salt adduction.

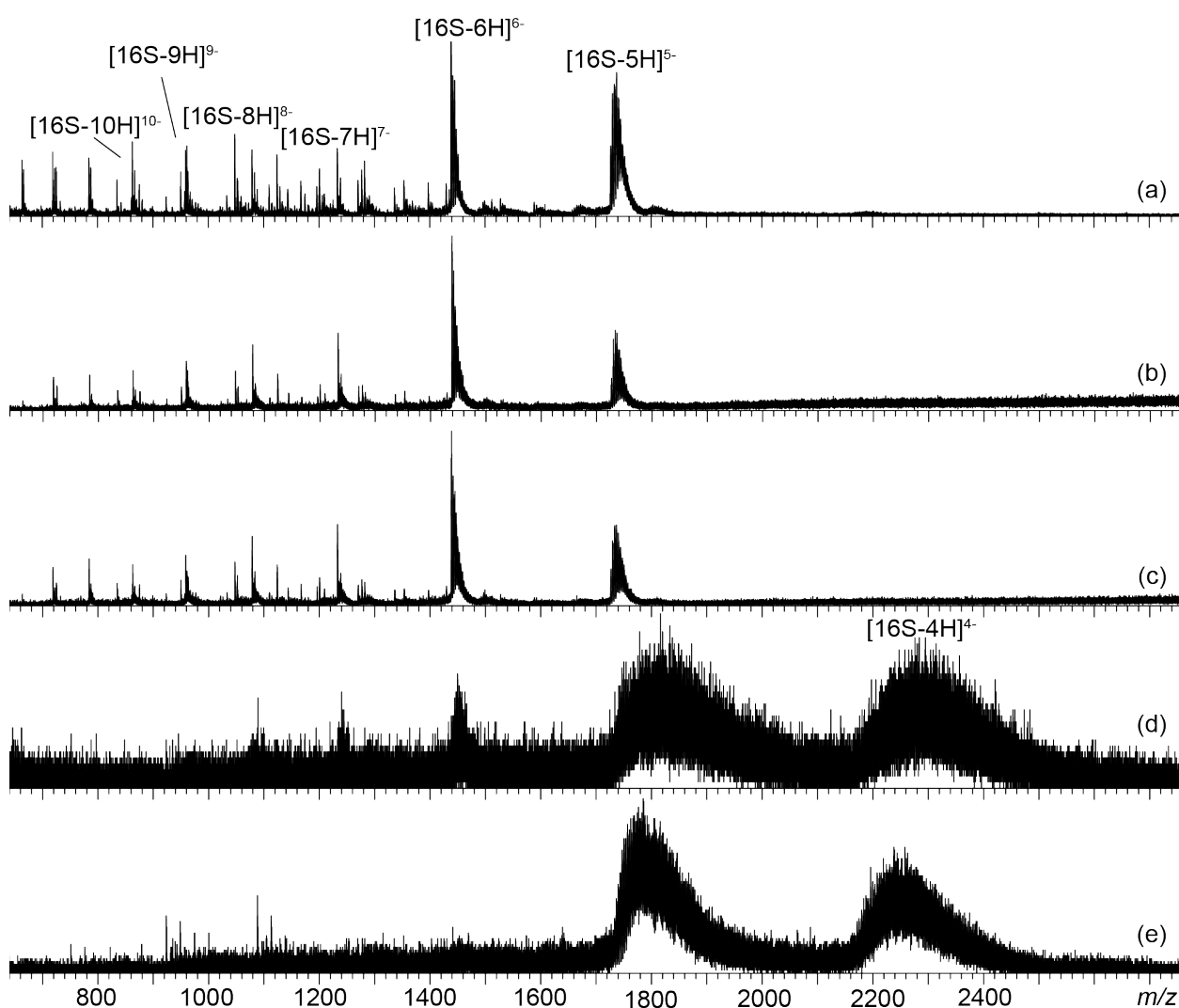


Figure 3.1. nESI mass spectra of a 27-mer A-site RNA construct as function of NH_4OAc concentration: (a) 10 mM, (b) 20 mM, (c) 50 mM, (d) 75 mM and (e) 100 mM.

The calibrated RNA CCS values (Table 3.1), on the other hand, remain constant from 10 mM to 100 mM NH₄OAc, suggesting that varying the ionic strength within this range does not have a major effect on overall ion conformation.

Table 3.1 | Calibrated CCS values for charge states 5- to 9- as function of NH₄OAc concentration in solution

Charge State	10 mM	20 mM	50 mM	75 mM	100 mM
5-	788 ± 43	791 ± 44	794 ± 44	813 ± 52	803 ± 48
6-	842 ± 46	845 ± 46	846 ± 47	850 ± 47	N/A
7-	1010 ± 57	1019 ± 56	1021 ± 56	1034 ± 65	N/A
8-	1186 ± 66	1196 ± 66	1197 ± 66	N/A	N/A
9-	1311 ± 72	1316 ± 72	1320 ± 73	N/A	N/A

Least square analysis CCS error is the result of triplicate measurements

We then examined the charge state distribution as a function of MeOH percentage in solution. From a “native-like” solvent (10 mM ammonium acetate), a unimodal abundance profile is observed for the generated RNA charge states, with charge states spanning from 5- to 12-, as shown in Figure 3.2a.

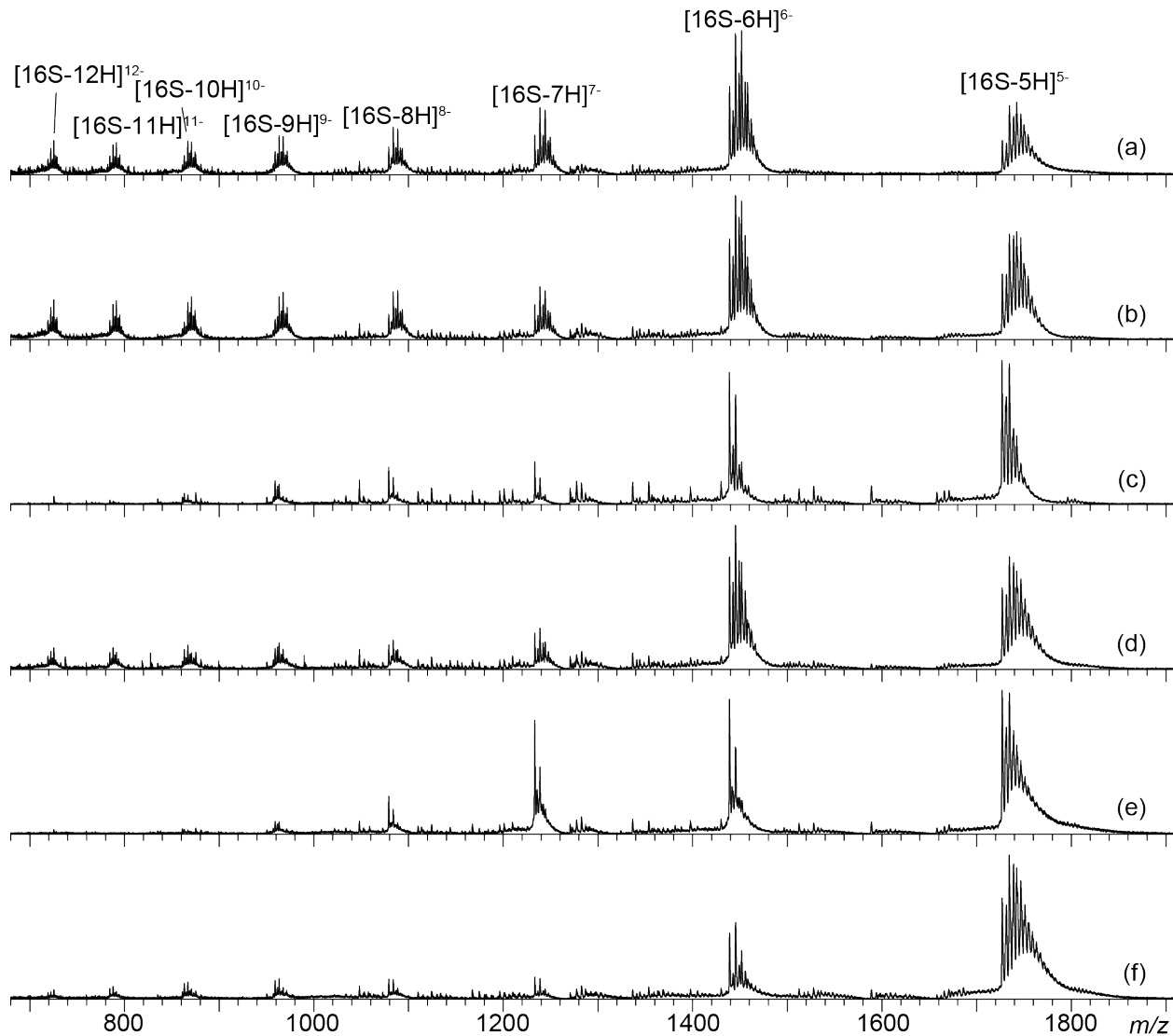


Figure 3.2. nESI mass spectra of a 27-mer A-site RNA construct as function of MeOH content (vol/vol): (a) 0%, (b) 10%, (c) 20%, (d) 30%, (e) 40%, and (f) 50%.

As shown in Figure 3.2, upon addition of MeOH up to 50% (vol/vol), there is no major shift in the average charge state. There is, however, a tendency for the charge state distribution to slightly shift to lower charge at higher MeOH concentrations. Because the addition of MeOH lowers the surface tension of the droplet, less charge is maintained resulting in lower-charged species. The unimodal charge state distribution is indicative of a single dominant gas-phase conformer. Furthermore, these data suggest that, upon addition of MeOH (up to 50%), no major change in RNA gas-phase conformation

occurs, further supported by the measured CD spectra (Figure 3.3). The CD profiles are indicative of an A-form helix, which RNA hairpins adopt in solution.

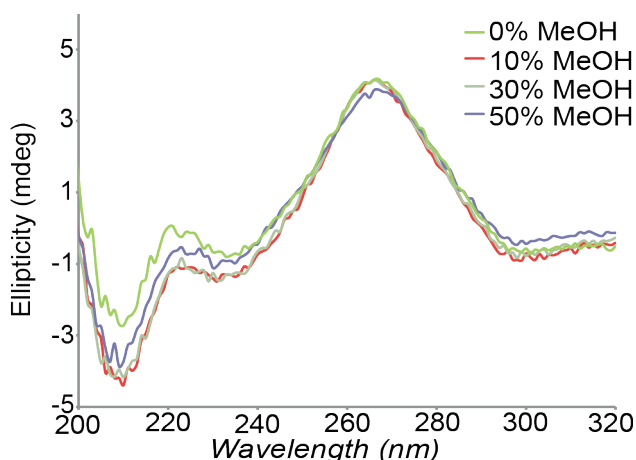


Figure 3.3. Circular dichroism spectra of the A-site RNA construct in different concentrations of MeOH; 0% (green), 10% (red), 30% (blue), and 50% (purple).

The average measured IM drift time for the 5- charge state was 6.58 ms across all solvent conditions, with a standard deviation of 0.13 ms (the mean and standard deviation is the result of triplicate measurements). The drift times remain constant, within standard error, for each charge state across the various MeOH concentrations with the 7- charge state showing the largest deviation of 2.2% (Figure 3.4).

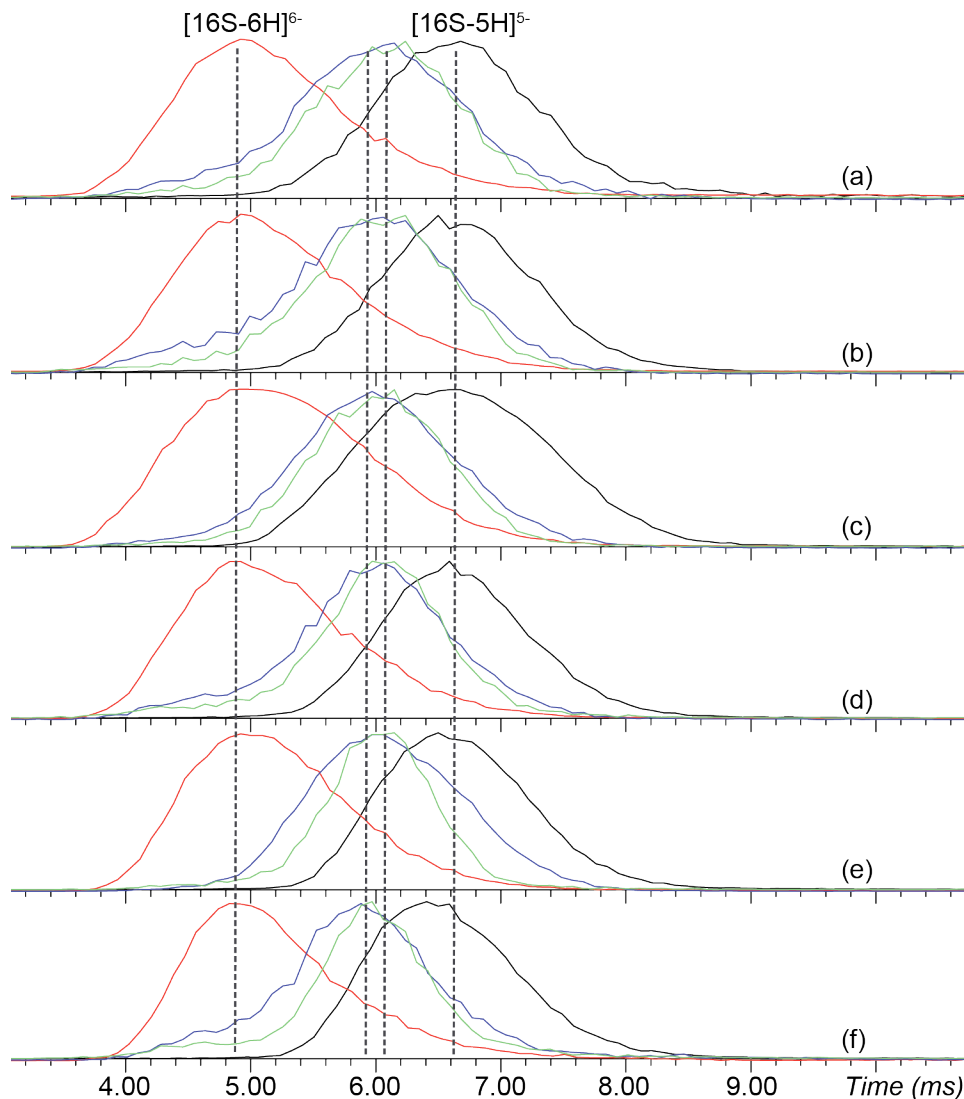


Figure 3.4. Arrival time distributions of A-site charge states; 5- charge state (black line), 6- charge state (red line), 7- charge state (blue line) and 8- charge state (green line) plotted as a function of MeOH content: (a) 0%, (b) 10%, (c) 20%, (d) 30%, (e) 40%, and (f) 50%.

Calibrating the measured drift times to CCS values provides improved insight into the overall A-site RNA conformation. A sigmoidal distribution is observed for the calibrated CCS value as function of anion charge state (Figure 3.5). The 7- charge state appears to represent a conformational transition between more collapsed conformations, adopted by the lower 5- and 6- charge states, and more extended conformations formed by the higher charge states. Compared with the drift time data, the CCS values remain constant (within error) across all solution conditions (up to 90% MeOH).

CCSs were previously measured as 988 and 1,008 Å² for the 5- and 6- charge states, respectively, of the same 27-mer RNA in a custom built ion mobility drift cell.⁴² The calibrated TWIMS-derived CCS values presented here for the same charge states are 779 and 824 Å² on average, respectively. These values are 24% and 20% lower than the values measured from the Bowers drift cell.⁴² The difference in CCS may be due to differences in ion source and ion transmission conditions between these instruments.⁶² For our TWIMS analysis, RNA anions were generated via a nanoESI source whereas the custom ion mobility mass spectrometer used by Bowers and co-workers was equipped with a conventional ESI source. The reduced capillary inner diameter in nESI results in much smaller initial droplets (~10⁻⁹ m diameter) than those generated in conventional ESI (~10⁻⁶ m diameter).⁶³ Consequently, the droplets generated via nESI experience much fewer droplet fission events prior to gaseous ion generation, thus improving the conservation of non-covalent interactions to maintain native-like conformations into the gas phase. Another difference in instrumentation is that the custom ion mobility system was equipped with ion funnels at the front end. As ions are focused passing through ion funnels, they experience collisions with background gases, which can cause heating and disruption of intramolecular interactions, thus generating gas-phase conformations with higher CCS values.⁶⁴

3.3.2 Molecular Modeling

Replica-exchange molecular dynamics simulations were utilized to further examine the charge state dependence of the gaseous RNA hairpin structure. Because neighboring temperatures are exchanged, we are able to sample a wide conformational space. A total of 1,000 structures for every charge state were saved and clustered based on RMSD of the structural families. We then used the trajectory method algorithm within the IMoS Software, with helium as background gas, to calculate CCS values. As shown in Figure 3.5, CCS and potential energy both increase as charge state of the molecule increase. The relative sigmoidal trend mirrors the experimental CCS measurements.

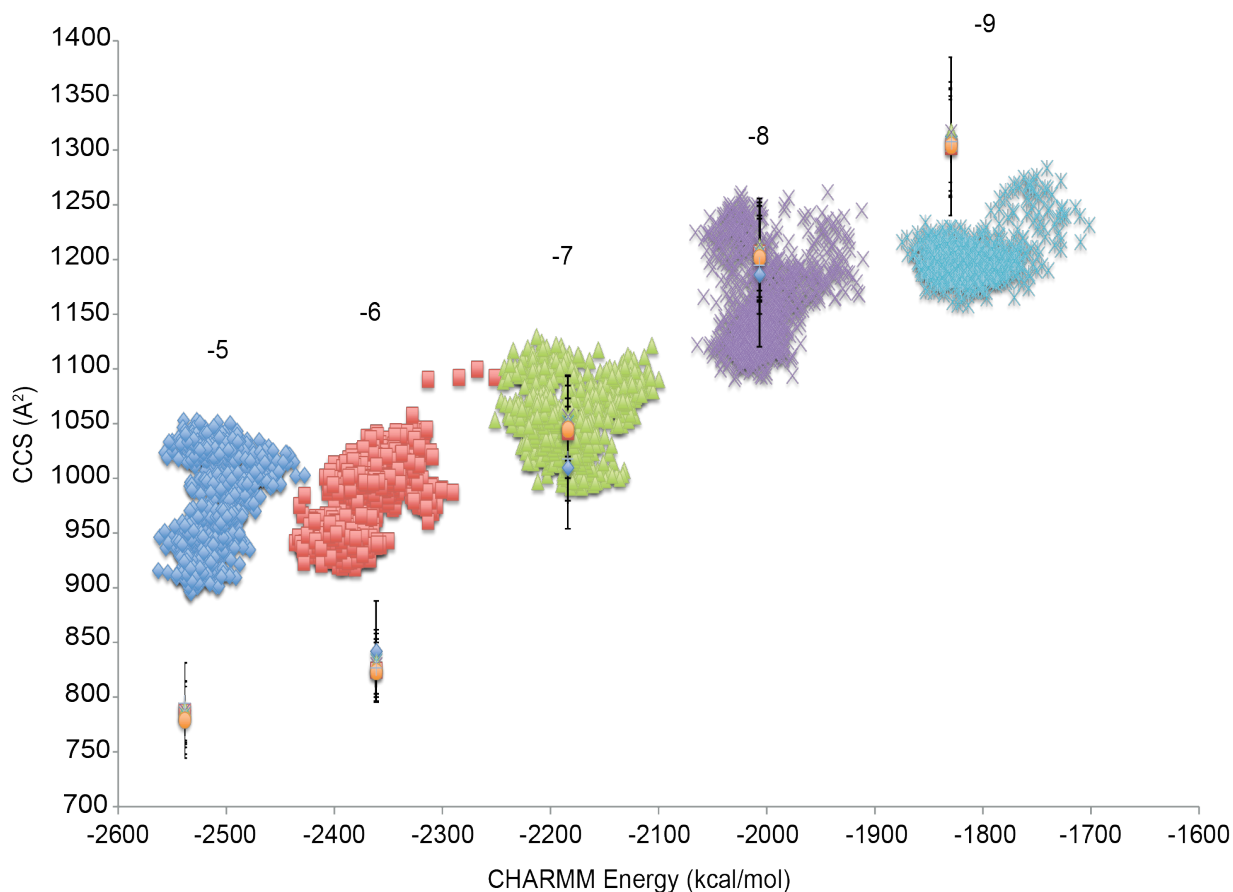


Figure 3.5. Replica-exchange molecular dynamics structures of different RNA hairpin charge states; 5- charge state (blue), 6- charge state (red), 7- charge state (green), 8- charge state (purple), and 9- charge state (teal). Structures are sorted by calculated CCS (from IMoS software) and plotted as a function of CHARMM energy. Experimental calibrated CCSs (from TWIMS) are also plotted. Error bars are the least square analysis from triplicate experimentally measured CCS values.

The modeled cross sections for the lower charge states, 5- and 6-, do not overlap with the experimentally determined values (Figure 3.5). The smallest average difference between modeled and experimentally determined CCS values for these two charge states is 15% and 10%, respectively (Figures 3.6a and 3.6b). On the other hand, the modeled 7- and 8- charge state ensembles do overlap with the experimentally determined CCS values (Figures 3.6c and 3.6d). For the 9- charge state the smallest difference between the modeled and experimentally derived CCS values is 0.75% (Figure 3.6e). One possible rationale for this divergence is that the charge locations used for modeling the gas-phase structures of lower charge states may differ from experiment. Charge location affects structural energetics and thus gas-phase

conformation. For example, nucleic acids have been shown to be zwitterionic in the gas phase with purine nucleobases having a propensity to be protonated.⁶⁵ Although quite computationally expensive, additional experiments need to be performed to account for other potential protonation and deprotonation sites. The current modeling did not include zwitterionic structures.

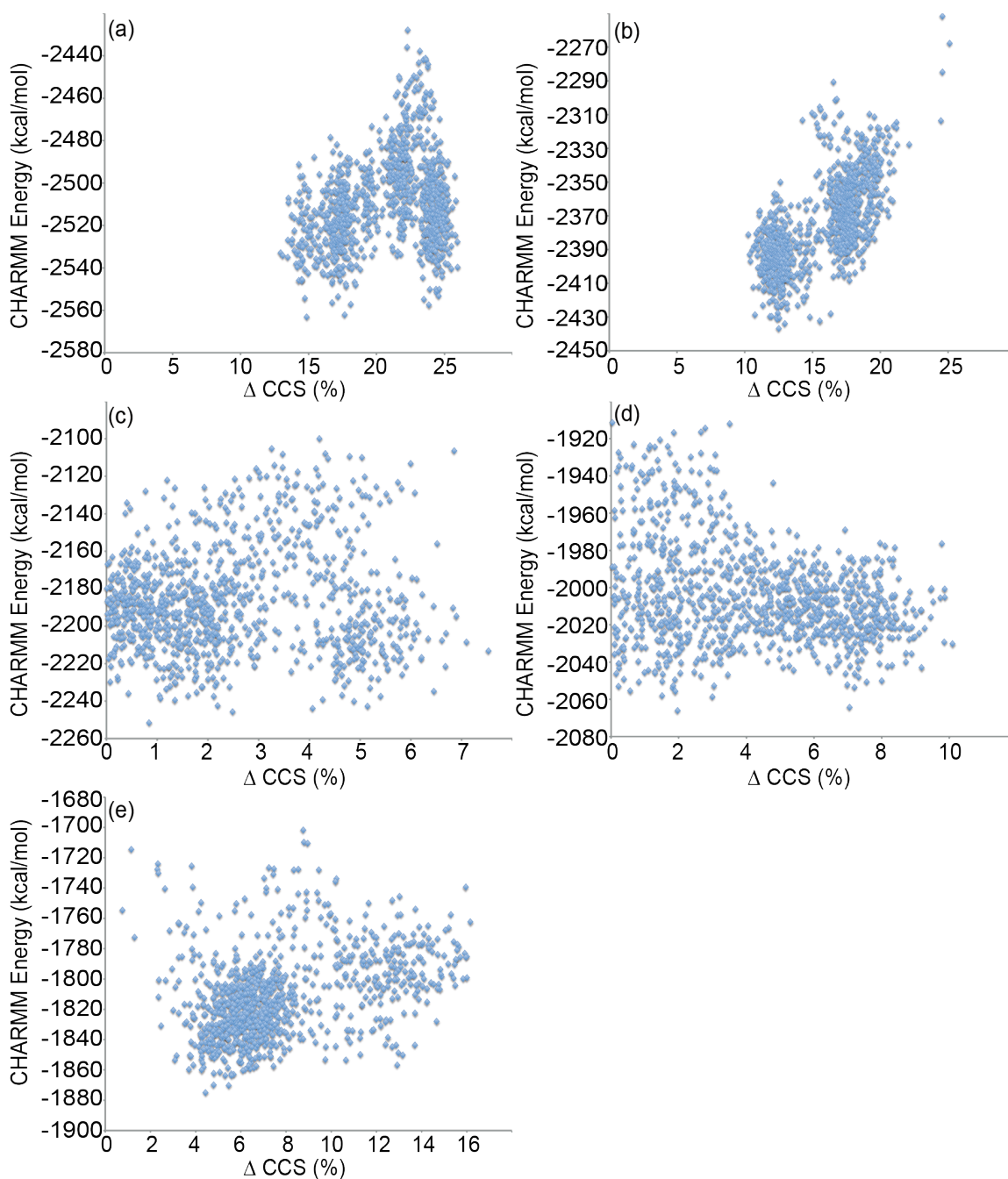


Figure 3.6. Computationally modeled structures sorted by CHARMM energy as a

function of the percent CCS difference from the mean experimentally determined CCS values; (a) 5- charge state, (b) 6- charge state, (c) 7- charge state, (d) 8- charge state, and (e) 9- charge state.

The 1,000 structures for each charge state were clustered based on RMSD of the RNA structure (Figure 3.7). The structures within cluster 8 (arbitrary value), pink data points, match closely with the mean experimentally determined CCS value. In a solvent free environment, gas-phase nucleic acids self-solvate, resulting in a slightly more compact conformation compared with their solution phase structure (Figure 3.7b).⁶⁶ Most of the contacts (i.e., base pairing) appear to remain intact. These results suggest that the 7- charge state of the RNA hairpin is most “native-like”. The lower charge states form much more globular structures, not observed in solution, whereas the higher charge states are more extended. One possible rationale for the much higher experimental CCS (compared to the computationally derived CCS) of the 9- charge state is that the computationally derived models represent structures that maintain hairpin-like features, which may not be representative of what is observed experimentally. The experimental 9- charge state may represent a denatured RNA strand. Thus, computational experiments under a wider range of starting conditions and constraints are needed.

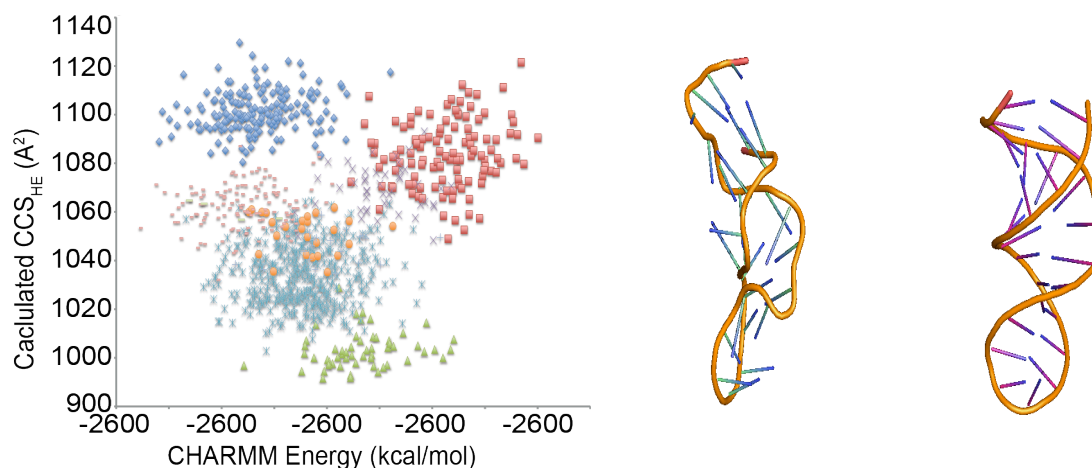
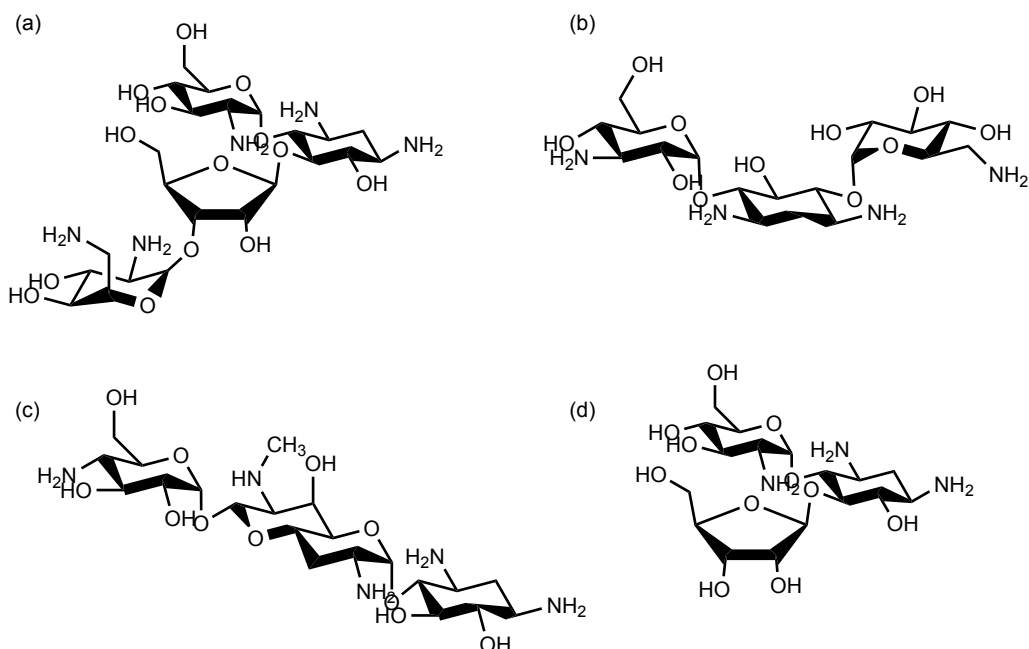


Figure 3.7. (Left) 1,000 computationally generated structures of the 7- charge state of the model A-site RNA. The structures are clustered (9 total clusters) based on RMSD of the RNA structure. (Middle) representative structure from the lowest energy cluster (pink data points). (Right) NMR derived structure, PDB ID: 1A3M.

3.3.3 MeOH and pH Effects on RNA-ligand Binding

MeOH, similar to a number of organic additives, has been shown to destabilize RNA secondary structure in solution at high concentrations. When mixed with MeOH, the activity of water is decreased, affecting the equilibrium of interactions between water molecules and the nucleic acid. The organic additives form hydrophobic interactions with the nucleobases, resulting in the destabilization of nucleic RNA helices.^{67,68} Other organic additives, such as dimethyl sulfoxide (DMSO) at low concentrations, have been shown to decrease ligand-binding affinities of A-site RNA complexes.⁴⁸ To investigate the effect of solution on ligand binding, we determined the dissociation constant (from MS data) as a function of solution content for aminoglycosides (Figure 3.8) in different K_D regimes. To rule out non-specific ligand binding resulting from the nESI process, we included an RNA sequence without the bulging adenine residue (16S*), Figure 3.8. The bulging A residue is essential for aminoglycoside binding.^{45,69} Therefore, any binding observed should be an nESI artifact.



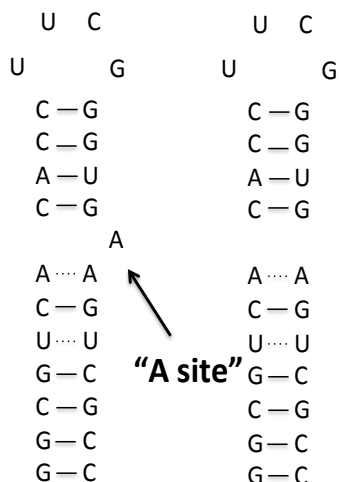


Figure 3.8. (Top) Aminoglycoside ligands; (a) paromomycin, (b) kanamycin B (c) apramycin and (d) ribostamycin. (Bottom Left) 16S sequence, (Right) 16* sequence.

Figure 3.9 shows mass spectra corresponding to 16S and 16S* paromomycin complexes as a function of MeOH concentration. Expected single binding events are observed for 16S complexes. The measured K_D value (extracted from MS data utilizing Equations 3.3-3.5) from a native-like solution (10 mM NH_4OAc) is $0.06 \mu\text{M}$ ($\pm 0.01 \mu\text{M}$). The K_D values agree with previously determined K_D measurements derived from mass spectrometry and solution phase experiments.^{41,46,47} The K_D remains constant (within error) up to 25% MeOH, suggesting that MeOH as an organic additive does not significantly alter A-site RNA local structure below that concentration. As the MeOH concentration increases further, starting from 50%, the binding strength gradually decreases. A similar trend is observed for other aminoglycosides of different known dissociation constants (Figure 3.10).

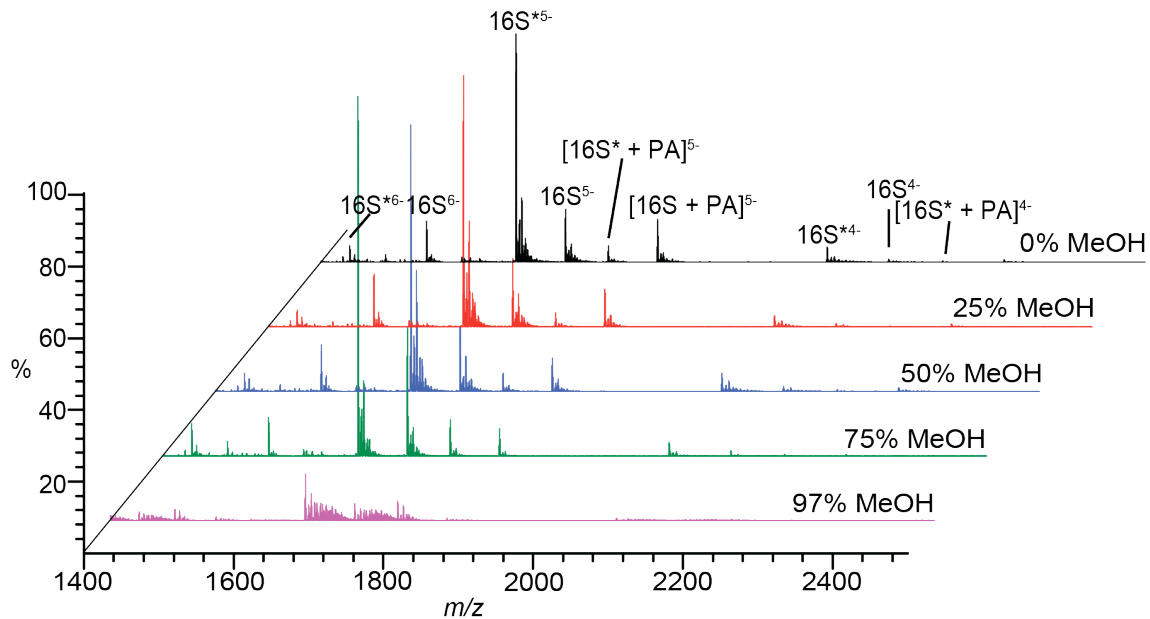


Figure 3.9. Mass spectra of 16S/16S* - paromomycin complexes plotted as a function of MeOH content.

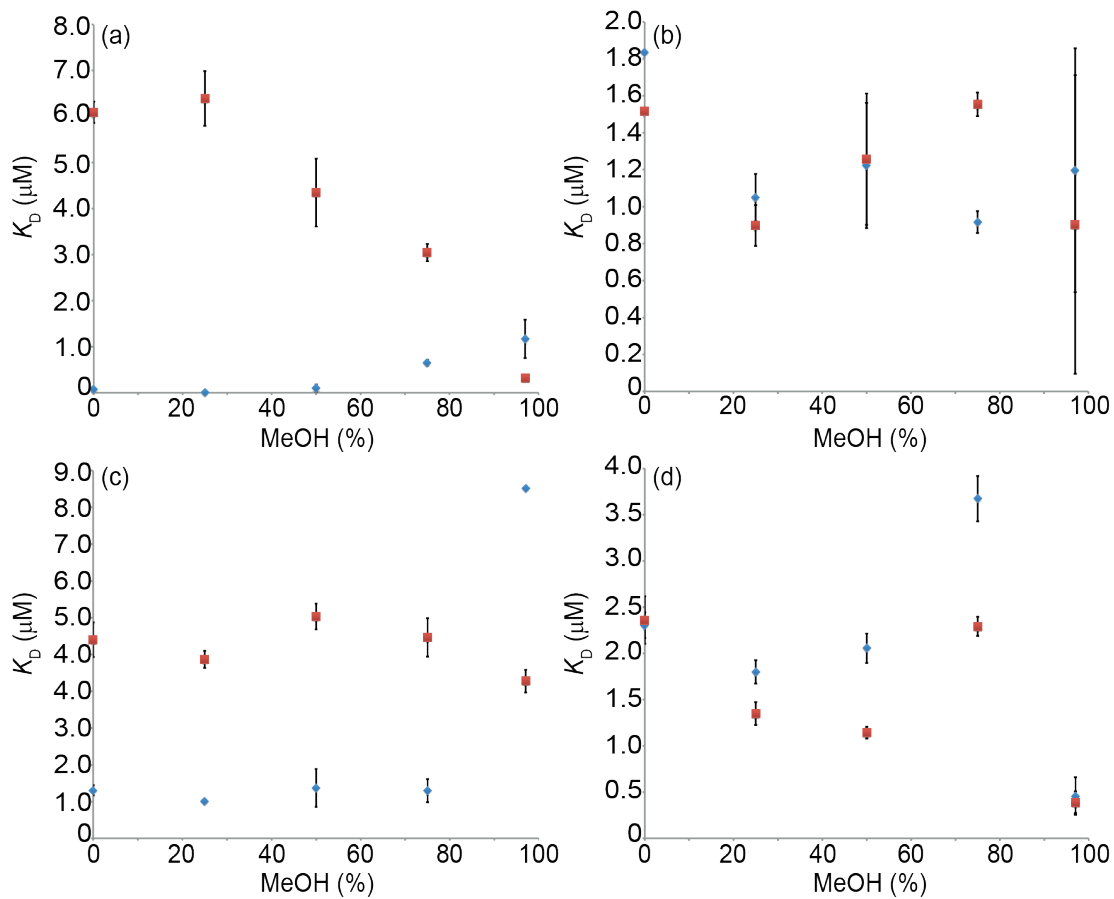


Figure 3.10. 16S (blue diamonds) and 16S* (red squares) / aminoglycoside complex K_D values as a function of MeOH content; (a) paromomycin, (b) kanamycin B, (c) apramycin, and (d) ribostamycin. Error bars are the result of triplicate measurements.

Table 3.2 | K_D values of aminoglycosides bound to 16s A-site construct as a function of MeOH content

Ligand	0% MeOH	25% MeOH	50% MeOH	75% MeOH	97% MeOH	Ref ⁴⁶
Paromomycin	0.06 ± 0.01	0.04 ± 0.02	0.10 ± 0.08	0.60 ± 0.06	1.17 ± 0.42	0.2
Kanamycin B	1.83	1.05 ± 0.13	1.22 ± 0.33	0.92 ± 0.06	1.20 ± 0.66	1.4
Apramycin	1.31 ± 0.14	1.00 ± 0.04	1.37 ± 0.51	1.30 ± 0.32	13.55 ± 5.72	6.3
Ribostamycin	2.30 ± 0.14	1.80 ± 0.13	2.10 ± 0.16	3.67 ± 0.24	0.46 ± 0.20	25

Standard error is the result of triplicate measurements.

Other factors that may affect RNA-ligand binding include temperature, ionic strength, and pH. Binding of aminoglycosides to the RNA A-site region is primarily electrostatically driven. At neutral pH, because of their basic nature, aminoglycosides are positively charged. Acids or bases are typically added to ESI solutions to facilitate protonation or deprotonation in positive and negative ion mode, respectively. RNA oligonucleotides are inherently negatively charged in solution because of the highly negatively charged phosphate backbone. Therefore, addition of bases to the ESI solution enhances deprotonation, thus improving ionization efficiency. Here, we investigate the effect of pH on RNA-aminoglycoside binding, ranging from acidic to basic pH.

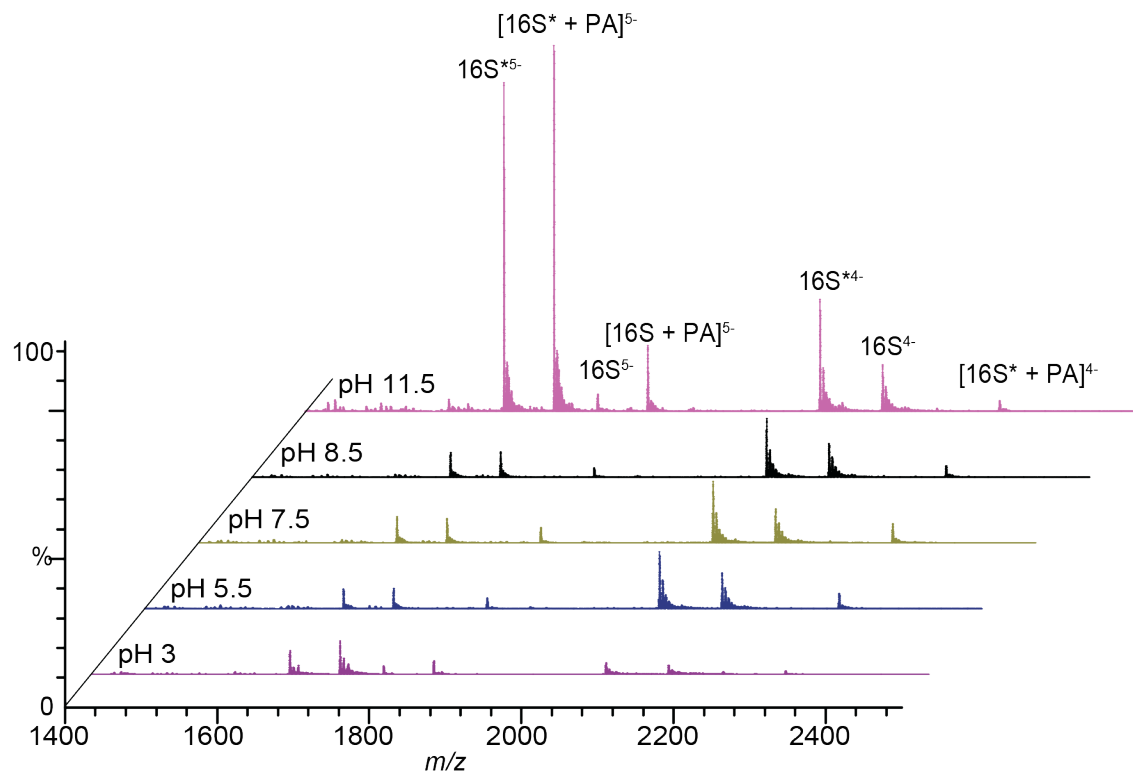


Figure 3.11. Mass spectra of 16S/16S* - paromomycin complexes plotted as a function of solution pH.

Figure 3.11 shows representative mass spectra of 16S/16S* - paromomycin complexes as a function of pH from pH 3.0 to pH 11.5. Formic acid (FA) and triethylamine (TEA) were used as the acid and base in these experiments. Not surprisingly, as the pH increases, so does the ionization efficiency. However, the charge state distribution shifts to higher charge states and, due to Coulomb repulsion, secondary structure is likely destabilized. Also, weakest binding of paromomycin to the A-site is observed at pH 11.5 (1.71 μ M). At elevated pH, the sugar moieties of the aminoglycosides are likely not protonated. The interactions with the RNA are, therefore, weakened, resulting in a higher K_D value. As shown in Figure 3.12, optimal ligand-binding occurs at neutral pH, 7.5.

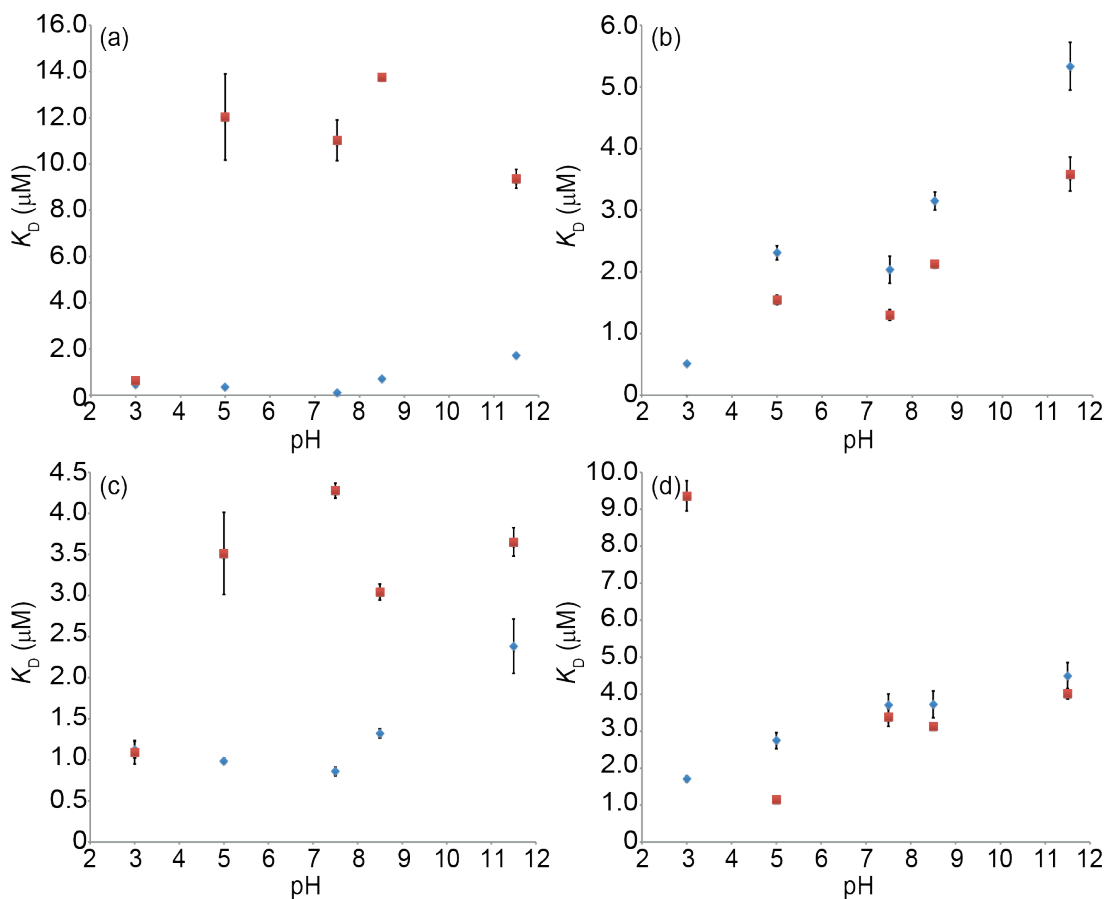


Figure 3.12. 16S (blue diamonds) and 16S* (red squares) / aminoglycoside complex K_D values as a function of solution pH; (a) paromomycin, (b) kanamycin B, (c) apramycin, and (d) ribostamycin. Error bars are the result of triplicate measurements.

Table 3.3 | K_D values of aminoglycosides bound to 16s A-site construct as a function of pH

Ligand	pH 3.0	pH 5.0	pH 7.5	pH 8.5	pH 11.5	Ref ⁴⁶
Paromomycin	0.45 ± 0.09	0.36 ± 0.05	0.10 ± 0.08	0.71 ± 0.07	1.71 ± 0.08	0.2
Kanamycin B	0.51 ± 0.01	2.31 ± 0.12	2.03 ± 0.22	3.15 ± 0.15	5.34 ± 0.39	1.4
Apramycin	1.13 ± 0.10	0.99 ± 0.03	0.86 ± 0.05	1.32 ± 0.06	2.38 ± 0.33	6.3
Ribostamycin	1.71 ± 0.08	2.74 ± 0.22	3.70 ± 0.30	3.72 ± 0.36	4.01 ± 0.14	25

Standard error is the result of triplicate measurements.

3.4 Conclusion

We examined the effect of ESI solution conditions on the confirmation and ligand binding of A-site RNA/aminoglycoside complexes via ion mobility mass spectrometry and ligand binding assays, respectively. For a given charge state, solvent conditions

(ionic strength and organic content) does not alter the CCS of the ion. The data suggest that ESI solution conditions do not have a major effect on RNA hairpin conformation on the timescale of the given experiment. REMD simulations produced a plethora of candidate gas-phase structures, owing to the heterogeneity of RNA conformations. The 7- charge state most closely resembles the native solution-phase structure. Further computational charge localization experiments are needed to sample a wider range of gas-phase structures. Binding strength remains constant (within error) up to ~ 50% MeOH and optimal binding occurs at neutral pH, suggesting that the A-site hairpin is not greatly disrupted under such conditions and allowing for native top-down experiments (e.g., via niECD). The combination of IMMS and REMD provides insight into RNA hairpin behavior in both solution and gas-phase and constitutes a potential approach for studying native RNA interactions.

3.5 References

- (1) Cooper, T. A.; Wan, L.; Dreyfuss, G. RNA and disease. *Cell* **2009**, *136*, 777-793.
- (2) Ding, Q.; Markesbery, W. R.; Chen, Q.; Li, F.; Keller, J. N. Ribosome Dysfunction is an Early Event in Alzheimer's Disease. *J. Neurosci.* **2005**, *25*, 9171-9175.
- (3) Sahin, U.; Kariko, K.; Tureci, O. mRNA-based therapeutics--developing a new class of drugs. *Nat. Rev. Drug Discov.* **2014**, *13*, 759-780.
- (4) Chow, C. S.; Bogdan, F. M. A Structural Basis for RNA-Ligand Interactions. *Chem. Rev.* **1997**, *97*, 1489-1513.
- (5) Svoboda, P.; Di Cara, A. Hairpin RNA: a secondary structure of primary importance. *Cell Mol. Life Sci.* **2006**, *63*, 901-908.
- (6) Daher, M.; Mustoe, A. M.; Morriss-Andrews, A.; Brooks Iii, C. L.; Walter, N. G. Tuning RNA folding and function through rational design of junction topology. *Nucleic Acids Res.* **2017**, *45*, 9706-9715.
- (7) Adams, C. C.; Stern, D. B. Control of mRNA stability in chloroplasts by 3' inverted repeats- effects of stem and loop mutations on degradation of psbA mRNA in vitro. *Nucleic Acids Res.* **1990**, *18*, 6003-6010.
- (8) Yu, E.; Fabris, D. Direct Probing of RNA Structures and RNA-Protein Interactions in the HIV-1 Packaging Signal by Chemical Modification and Electrospray Ionization Fourier Transform Mass Spectrometry. *J. Mol. Biol.* **2003**, *330*, 211-223.
- (9) Scalabrin, M.; Siu, Y.; Asare-Okai, P. N.; Fabris, D. Structure-specific Ribonucleases for MS-based Elucidation of Higher-order RNA Structure. *J. Am. Soc. Mass Spectrom.* **2014**, *25*, 1136-1145.
- (10) Abi-Ghanem, J.; Gabelica, V. Nucleic acid Ion Structures in the Gas Phase. *Phys. Chem. Chem. Phys.* **2014**, *16*, 21204-21218.

- (11) Arcella, A.; Dreyer, J.; Ippoliti, E.; Ivani, I.; Portella, G.; Gabelica, V.; Carloni, P.; Orozco, M. Structure and Dynamics of Oligonucleotides in the Gas Phase. *Angew. Chem. Int. Ed. Engl.* **2015**, *54*, 467-471.
- (12) Limbach, P. A.; Crain, P. F.; McCloskey, J. A. Molecular Mass Measurement of Intact Ribonucleic Acids via Electrospray Ionization Quadrupole Mass Spectrometry. *J. Am. Soc. Mass Spectrom.* **1994**, *6*, 27-39.
- (13) Guo, X.; Bruist, M. F.; Davis, D. L.; Bentzley, C. M. Secondary Structural Characterization of Oligonucleotide Strands Using Electrospray Ionization Mass Spectrometry. *Nucleic Acids Res.* **2005**, *33*, 3659-3666.
- (14) Hofstadler, S. A.; Griffey, R. H. Analysis of Noncovalent Complexes of DNA and RNA by Mass Spectrometry. *Chem. Rev.* **2001**, *101*, 377-390.
- (15) Kieltyka, J. W.; Chow, C. S. Probing RNA Hairpins with Cobalt(III)hexammine and Electrospray Ionization Mass Spectrometry. *J. Am. Soc. Mass Spectrom.* **2006**, *17*, 1376-1382.
- (16) Hagan, N.; Fabris, D. Direct Mass Spectrometric Determination of the Stoichiometry and Binding Affinity of the Complexes between Nucleocapsid Protein and RNA Stem-Loop Hairpins of the HIV-1 Ψ -Recognition Element. *Biochemistry* **2003**, *42*, 10736-10745.
- (17) Schneeberger, E. M.; Breuker, K. Native Top-Down Mass Spectrometry of TAR RNA in Complexes with a Wild-Type tat Peptide for Binding Site Mapping. *Angew. Chem. Int. Ed.* **2017**, *56*, 1254-1258.
- (18) Rosu, F.; Pirotte, S.; de Pauw, E.; Gabelica, V. Positive and Negative Ion Mode ESI-MS and MS/MS for Studying Drug-DNA Complexes. *Int. J. Mass Spectrom.* **2006**, *253*, 156-171.
- (19) Rosu, F.; De Pauw, E.; Gabelica, V. Electrospray Mass Spectrometry to Study Drug-nucleic Acids Interactions. *Biochimie.* **2008**, *90*, 1074-1087.
- (20) Beck, J. L.; Colgrave, M. L.; Ralph, S. F.; Shell, M. M. Electrospray Ionization Mass Spectrometry of Oligonucleotide Complexes with Drugs, Metals, and Proteins. *Mass Spectrom. Rev.* **2001**, *20*, 61-87.
- (21) Kapur, A.; Beck, J. L.; Brown, S. E.; Dixon, N., E.; Shell, M. M. Use of electrospray ionization mass spectrometry to study binding interactions between a replication terminator protein and DNA. *Protein Sci.* **2002**, *11*, 147-157.
- (22) Hofstadler, S. A.; Sannes-Lowery, K. A.; Crooke, S. T.; Ecker, D. J.; Sasmor, H.; Manalili, S.; Griffey, R. H. Multiplexed Screening of Neutral Mass-Tagged RNA Targets against Ligand Libraries with Electrospray Ionization FTICR MS: A Paradigm for High-Throughput Affinity Screening. *Anal. Chem.* **1999**, *71*, 3436-3440.
- (23) Taucher, M.; Breuker, K. Characterization of modified RNA by top-down mass spectrometry. *Angew Chem. Int. Ed. Engl.* **2012**, *51*, 11289-11292.
- (24) Yoo, H. J.; Wang, N.; Zhuang, S.; Song, H.; Hakansson, K. Negative-ion electron capture dissociation: radical-driven fragmentation of charge-increased gaseous peptide anions. *J. Am. Chem. Soc.* **2011**, *133*, 16790-16793.
- (25) Hersberger, K. E.; Hakansson, K. Characterization of O-sulfopeptides by negative ion mode tandem mass spectrometry: superior performance of negative ion electron capture dissociation. *Anal. Chem.* **2012**, *84*, 6370-6377.

- (26) Baker, E. S.; Bowers, M. T. B-DNA helix stability in a solvent-free environment. *J. Am. Soc. Mass Spectrom.* **2007**, *18*, 1188-1195.
- (27) Kebarle, P.; Verkerk, U. H. Electrospray: From Ions in Solution to Ions in the Gas Phase, What We Know Now. *Mass Spectrom. Rev.* **2009**, *28*, 898-917.
- (28) Konermann, L.; Ahadi, E.; Rodriguez, A. D.; Vahidi, S. Unraveling the Mechanism of Electrospray Ionization. *Anal. Chem.* **2013**, *85*, 2-9.
- (29) Herskovits, T. T.; Singer, S. J.; Geiduschek, E. P. Nonaqueous Solutions of DNA. Denaturation in Methanol and Ethanol. *Arch. Biochem. Biophys.* **1961**, *94*, 99-114.
- (30) Geiduschek, E. P.; Herskovits, T. T. Nonaqueous Solutions of DNA. Reversible and Irreversible Denaturation in Methanol. *Arch. Biochem. Biophys.* **1961**, *95*, 114-129.
- (31) Herskovits, T. T. Nonaqueous Solutions of DNA: Factors Determining the Stability of the Helical Configuration in Solution. *Arch. Biochem. Biophys.* **1962**, *97*, 474-484.
- (32) Marchand, A.; Gabelica, V. Native electrospray mass spectrometry of DNA G-quadruplexes in potassium solution. *J. Am. Soc. Mass Spectrom.* **2014**, *25*, 1146-1154.
- (33) Metwally, H.; McAllister, R. G.; Konermann, L. Exploring the mechanism of salt-induced signal suppression in protein electrospray mass spectrometry using experiments and molecular dynamics simulations. *Anal. Chem.* **2015**, *87*, 2434-2442.
- (34) Shvartsburg, A. A.; Smith, R. D. Fundamentals of Traveling Wave Ion Mobility Spectrometry. *Anal. Chem.* **2008**, *80*, 9689-9699.
- (35) Balthasart, F.; Plavec, J.; Gabelica, V. Ammonium ion binding to DNA G-quadruplexes: do electrospray mass spectra faithfully reflect the solution-phase species? *J. Am. Soc. Mass Spectrom.* **2013**, *24*, 1-8.
- (36) Ferreira, R.; Marchand, A.; Gabelica, V. Mass Spectrometry and Ion Mobility Spectrometry of G-quadruplexes. A study of Solvent Effects on Dimer Formation and Structural Transitions in the Telomeric DNA Sequence d(TAGGGTTAGGGT). *Methods* **2012**, *57*, 56-63.
- (37) Gabelica, V.; Baker, E. S.; Teulade-Fichou, M. P.; Pauw, E.; Bowers, M. T. Stabilization and Structure of Telomeric and c-myc Region Intramolecular G-Quadruplexes The Role of Central Cations and Small Planar Ligands. *J. Am. Chem. Soc.* **2007**, *129*, 895-904.
- (38) Marchand, A.; Ferreira, R.; Tateishi-Karimata, H.; Miyoshi, D.; Sugimoto, N.; Gabelica, V. Sequence and Solvent Effects on Telomeric DNA Bimolecular G-quadruplex Folding Kinetics. *J. Phys. Chem. B.* **2013**, *117*, 12391-12401.
- (39) Balbeur, D.; Widart, J.; Leyh, B.; Cravello, L.; De Pauw, E. Detection of Oligonucleotide Gas-phase Conformers: H/D Exchange and Ion Mobility as Complementary Techniques. *J. Am. Soc. Mass Spectrom.* **2008**, *19*, 938-946.
- (40) Burmistrova, A.; Gabelica, V.; Duwez, A. S.; De Pauw, E. Ion Mobility Spectrometry Reveals Duplex DNA Dissociation Intermediates. *J. Am. Soc. Mass Spectrom.* **2013**, *24*, 1777-1786.

- (41) Griffey, R. H.; Hofstadler, S. A.; Sannes-Lowery, K. A.; Ecker, D. J.; Crooke, S. T. Determinants of Aminoglycoside-Binding Specificity for rRNA by Using Mass Spectrometry. *Proc. Natl. Acad. Sci.* **1999**, *96*, 10129-10133.
- (42) Baker, E. S.; Dupuis, N. F.; Bowers, M. T. Aminoglycoside antibiotics: A-site Specific Binding to 16S. *Int. J. Mass Spectrom.* **2009**, *283*, 105-111.
- (43) Recht, M. I.; Fourmy, D.; Blanchard, S. C.; Dahlquist, K. D.; Puglisi, J. D. RNA Sequence Determinants for Aminoglycoside Binding to an A-site rRNA Model Oligonucleotide. *J. Mol. Biol.* **1996**, *22*, 421-436.
- (44) Fourmy, D.; Yoshizawa, S.; Puglisi, J. D. Paromomycin Binding Induces a Local Conformational Change in the A-site of 16 S rRNA. *J. Mol. Biol.* **1998**, *277*, 333-345.
- (45) Wong, C. H.; Hendrix, M.; Priestley, E. S.; Greenberg, W. A. Specificity of aminoglycoside antibiotics for the A-site of the decoding region of ribosomal RNA. *Chem. Biol.* **1998**, *7*, 397-406.
- (46) Sannes-Lowery, K. A.; Griffey, R. H.; Hofstadler, S. A. Measuring dissociation constants of RNA and aminoglycoside antibiotics by electrospray ionization mass spectrometry. *Anal. Biochem.* **2000**, *280*, 264-271.
- (47) Ryu, D. H.; Rando, R. R. Aminoglycoside Binding to Human and Bacterial A-Site rRNA Decoding Region Constructs. *Bioorg. Med. Chem.* **2001**, *9*, 2601-2608.
- (48) Lee, J.; Vogt, C. E.; McBairty, M.; Al-Hashimi, H. M. Influence of dimethylsulfoxide on RNA structure and ligand binding. *Anal. Chem.* **2013**, *85*, 9692-9698.
- (49) Griffey, R. H.; Sannes-Lowery, K. A.; Drader, J. J.; Mohan, V.; Swayze, E. E.; Hofstadler, S. A. Characterization of low-affinity complexes between rna and small molecules using electrospray ionization mass spectrometry. *J. Am. Chem. Soc.* **2000**, *122*, 9933-9938.
- (50) Allen, S. J.; Schwartz, A. M.; Bush, M. F. Effects of polarity on the structures and charge states of native-like proteins and protein complexes in the gas phase. *Anal. Chem.* **2013**, *85*, 12055-12061.
- (51) Ruotolo, B. T.; Benesch, J. L.; Sandercock, A. M.; Hyung, S. J.; Robinson, C. V. Ion Mobility-mass Spectrometry Analysis of Large Protein Complexes. *Nat. Protoc.* **2008**, *3*, 1139-1152.
- (52) Sugita, Y.; Okamoto, Y. Replica-Exchange Molecular Dynamics Method for Protein Folding. *Chem. Phys. Lett.* **1999**, *314*, 141-151.
- (53) Rueda, M.; Kalko, S. G.; Luque, J.; Orozco, M. The Structure and Dynamics of DNA in the Gas Phase. *J. Am. Chem. Soc.* **2003**, *125*, 8007-8014.
- (54) Brooks, B. R.; Brooks, C. L., 3rd; Mackerell, A. D., Jr.; Nilsson, L.; Petrella, R. J.; Roux, B.; Won, Y.; Archontis, G.; Bartels, C.; Boresch, S.; Caflisch, A.; Caves, L.; Cui, Q.; Dinner, A. R.; Feig, M.; Fischer, S.; Gao, J.; Hodoscek, M.; Im, W.; Kuczera, K.; Lazaridis, T.; Ma, J.; Ovchinnikov, V.; Paci, E.; Pastor, R. W.; Post, C. B.; Pu, J. Z.; Schaefer, M.; Tidor, B.; Venable, R. M.; Woodcock, H. L.; Wu, X.; Yang, W.; York, D. M.; Karplus, M. CHARMM: the biomolecular simulation program. *J. Comput. Chem.* **2009**, *30*, 1545-1614.
- (55) Foloppe, N.; Mackerell, A. D., Jr. All-atom Empirical Force Field for Nucleic Acids- I. Parameter Optimization Based on Small Molecule and Condensed Phase Macromolecular Target Data. *J. Comput. Chem.* **2000**, *21*, 86-104.

- (56) Feig, M.; Karanicolas, J.; Brooks, C. L., 3rd MMTSB Tool Set: enhanced sampling and multiscale modeling methods for applications in structural biology. *J. Mol. Graph Model* **2004**, *22*, 377-395.
- (57) Larriba, C.; Hogan, C. J. Free molecular collision cross section calculation methods for nanoparticles and complex ions with energy accommodation. *J. Comput. Phys.* **2013**, *251*, 344-363.
- (58) Wang, W.; Kitova, E. N.; Klassen, J. S. Influence of Solution and Gas Phase Processes on Protein-Carbohydrate Binding Affinities Determined by Nanoelectrospray Fourier Transform Ion Cyclotron Resonance Mass Spectrometry. *Anal. Chem.* **2003**, *75*, 4945-4955.
- (59) Soper-Hopper, M. T.; Eschweiler, J. D.; Ruotolo, B. T. Ion Mobility-Mass Spectrometry Reveals a Dipeptide That Acts as a Molecular Chaperone for Amyloid beta. *ACS Chem. Biol.* **2017**, *12*, 1113-1120.
- (60) Turner, K. B.; Monti, S. A.; Fabris, D. Like polarity ion:ion reactions enable the investigation of specific metal interactions in nucleic acids and their noncovalent assemblies. *J. Am. Chem. Soc.* **2008**, *130*, 13353-13363.
- (61) Gray, R. D.; Chaires, J. B. Kinetics and Mechanism of K⁺- and Na⁺-Induced Folding of Models of Human Telomeric DNA into G-quadruplex Structures. *Nucleic Acids Res.* **2008**, *36*, 4191-4203.
- (62) Wyttenbach, T.; Kemper, P. R.; Bowers, M. T. Design of a new electrospray ion mobility mass spectrometer. *Int. J. Mass Spectrom.* **2001**, *212*, 13-23.
- (63) El-Faramawy, A.; Siu, K. W.; Thomson, B. A. Efficiency of Nano-electrospray Ionization. *J. Am. Soc. Mass Spectrom.* **2005**, *16*, 1702-1707.
- (64) Kelly, R. T.; Tolmachev, A. V.; Page, J. S.; Tang, K.; Smith, R. D. The Ion Funnel: Theory, Implementations, and Applications. *Mass Spectrom. Rev.* **2010**, *29*, 294-312.
- (65) Gidden, J.; Bowers, M. T. Gas-Phase Conformations of Deprotonated Trinucleotides (dGTT, dTGT, and dTTG): The Question of Zwitterion Formation. *J. Am. Soc. Mass Spectrom.* **2003**, *14*, 161-170.
- (66) Porrini, M.; Rosu, F.; Rabin, C.; Darre, L.; Gomez, H.; Orozco, M.; Gabelica, V. Compaction of Duplex Nucleic Acids upon Native Electrospray Mass Spectrometry. *ACS Cent. Sci.* **2017**, *3*, 454-461.
- (67) Nakano, S. I.; Sugimoto, N. The structural stability and catalytic activity of DNA and RNA oligonucleotides in the presence of organic solvents. *Biophys. Rev.* **2016**, *8*, 11-23.
- (68) Lambert, D.; Draper, D. E. Effects of osmolytes on RNA secondary and tertiary structure stabilities and RNA-Mg²⁺ interactions. *J. Mol. Biol.* **2007**, *370*, 993-1005.
- (69) Recht, M. I.; Douthwaite, S.; Dahlquist, K. D.; Puglisi, J. D. Effect of mutations in the A site of 16S rRNA on aminoglycoside antibiotic-ribosome interaction. *J. Mol. Biol.* **1999**, *286*, 33-43.

Chapter 4

Negative-Ion Mode Mass Spectrometry for Revealing Interaction sites within RNA-Protein Complexes and Selective Infrared Multiphoton Dissociation of RNA-peptide Crosslinks Species

4.1 Introduction

Ribonucleic acids (RNAs) often form complexes with proteins (e.g., ribonuclease P) to perform various cellular functions.¹ Detailed knowledge of such interaction sites provides a basis for understanding RNA functions. The RNA world hypothesis states that the current world was originated from early RNA catalysis. Throughout time, however, structural evidence has supported the central dogma of biology and RNAs serve mainly as genetic transfer molecules.² One exception is ribonuclease P (RNase P), which is an enzyme that catalyzes the maturation of the 5' end of tRNA precursors by cleaving extra nucleotides at the 5' end. Until recently, all known RNase P enzymes are composed of RNA and one or more protein components. However; Holzmann et al. showed evidence of a protein-only (or proteinaceous) RNase P (PRORP) in human mitochondria.³⁻⁵ One question is whether the PRORP evolved independently from the RNA-RNase P. Knowledge of PRORP interaction sites with tRNA will help gain additional mechanistic and evolutionary understanding of the PRORP enzyme family. With few available high-resolution RNA-protein complex structures, crosslinking techniques and non-covalent interaction mapping coupled with mass spectrometry (MS) provide an alternative tool for identifying interaction sites.⁶⁻¹⁰

Chemical and photochemical crosslinking techniques have emerged as the gold standard for locking interactions between nucleic acids and neighboring proteins of interest.¹¹ One example of a chemical crosslinking method is utilization of formaldehyde as the crosslink.^{12,13} Formaldehyde readily permeates cell walls and membranes, which

results in efficient crosslinks between proteins, DNAs, RNAs and other reactive molecules. A drawback of this approach is that formaldehyde can also induce protein–protein crosslinking, which compounds the difficulty in identifying direct protein–RNA interactions and yields generally low crosslinking yields, a particular problem for identification of nucleic acids that are expressed at low levels in cells. Another method of crosslinking is by chemically modifying the RNA backbone via acidophenacyl (AzP). AzP is introduced at a single position in the RNA, typically at the 5' or 3' ends. This method of crosslinking provides a broader view of proteins in the direct vicinity of the particular position of the crosslink (~9 Å). AzP reacts with primary amines, inserting into C-H and N-H bonds. This method, however, is undesirable for protein-RNA complexes with numerous interaction sites across the entire molecule because the position of the crosslink is fixed. Incorporating this type of crosslink at other regions of the RNA molecule must be done with great care as to not jeopardize the secondary or tertiary structure of the entire molecule.

RNA-protein crosslinks can also be established by UV irradiation at 254 nm. This method takes advantage of the naturally occurring UV reactivity of the RNA nucleobases at 254 nm.¹⁴ Crosslinking specificity, in this manner, may not be easily controlled, however. One way to better control specificity and also enhance crosslinking efficiency is by incorporating chromophores, such as a thio- or bromo groups, that react at significantly longer wavelengths.¹⁵ UV irradiation of 5-bromouridine (5-BrU) substituted RNA, for example, leads to the production of highly reactive uracyl radicals.^{16,17} As a result, proteins in the vicinity of RNA readily covalently binds to BrU substituted RNA. 5-BrU reacts most readily with sulfur- and aromatic-containing amino acids. It is worth noting, however, that 5-BrU can also react with other amino acids, although less readily, except for proline. Once a crosslink has been established, identification of crosslinked species is the next challenge. Crosslinking methods suffer from their potentially low yield for protein-RNA crosslinks, making it difficult to identify crosslinks in an excess of non-crosslinked species. Enrichment of crosslinked species over non-crosslinked species as well as identification of crosslinked species can be employed to circumvent these issues. For example, taking advantage of the similarities between protein-RNA crosslinks and phosphorylated peptides, enrichment strategies

used in phosphoproteomics can be employed:¹⁸ Immobilized metal affinity chromatography (IMAC) separates peptides based on their ability to interact with metal ions (Fe, Co, Cd, Ni, or Zn).¹⁹ Titanium dioxide (TiO₂) enrichment also utilizes interactions with the negatively charged sites of the crosslinked species.^{18,20} A complementary approach to the aforementioned chemical methods is taking advantage of the physical properties of the RNA phosphate group(s). Irradiation with 10.6 μm infrared (IR) photons has been shown to selectively dissociate phosphorylated peptides.²¹⁻²³ However, to our knowledge, this approach has not previously been extended to RNA-peptide crosslinks.

Significant attention has been devoted to identifying peptides directly interacting with RNA via conventional bottom-up liquid chromatography (LC) combined with RNA digestion (e.g., with RNase A, T1, or a combination of both enzymes) into mono-, di-, or tri-nucleotides.^{18,24-27} Such workflows, however, are typically unable to determine the crosslinking site within the RNA. Complementary tandem mass spectrometric techniques allow for a broader range of sequence information because multiple fragmentation pathways are accessed.²⁸ Here, we explore an RNA-centric approach with the goal to elucidate the binding sites between PRORP and pre-tRNA. We employ various negative ion mode MS/MS techniques (both slow-heating and electron-based) on RNA-peptide models, which are either crosslinked or non-covalently linked. Finally we introduce an alternative technique for crosslink identification via selective dissociation in IRMPD.

4.2 Experimental

4.2.1 Reagents

HPLC grade water and methanol (MeOH), formic acid (FA), triethylamine (TEA), and oxidized insulin chain A (GIVEQC[SO₃H]C[SO₃H]ASVC[SO₃H]SLYQLENYC[SO₃H]N) were purchased from Sigma-Aldrich (St. Louis, MO). The peptides angiotensin I (DRVHHPFHL), substance P (RPKPQQFFGLM), and ACTH 1-10 (SYSMEHFRWG), was purchased from BaChem (Bubendorf, Switzerland). Cholecystokinin (CCK) was

purchased from Abcam (Cambridge, MA). RNA oligonucleotide (rGCAUAC) was purchased from Integrated DNA Technologies Inc. (Coralville, IA). All peptides and oligonucleotides were dissolved in 50/50 water/MeOH electrospray solution and directly infused at 1-5 μ M concentrations. C-18 ZipTips were used for further desalting, if necessary. Dr. Michael Howard from the Fiecke Lab provided the proteinaceous RNase P 1 (PRORP1), from *Arabidopsis thaliana*, for LC/MS analysis. For the click-chemistry reaction, the synthetic peptide (RGDFIF*KQ), in which F* is 4-azidophenylalanine, was purchased from Eurogentec, UK. The 11-mer oligonucleotide (UAACUAUCAU*G-Biotin-TEG3'), in which U* is 5-ethynyl-2'deoxyuridine (5EdU), was purchased from BaseClick, Germany.

4.2.2 Non-Covalent Complex

RNA oligonucleotide (rGCAUAC)/peptide (angiotensin I (DRVHPFHL) and substance P (RPKPQQFFGLM)), complexes were prepared by mixing the peptide at 2:1 molar excess with the RNA. The solution was left to sit at 37 ° C for 30 minutes. The resulting complexes were diluted into ESI solution (50/50 water/methanol) without further purification. All proteins and oligonucleotides were diluted to a final concentration of 1-2 μ M.

4.2.3 Tandem Mass Spectrometry

All mass spectra were acquired with a 7-T quadrupole-FT-ICR mass spectrometer (SolariX, Bruker Daltonics, Billerica, MA) retrofitted with a Synrad Firestar 25 W, 10.6 μ m infrared laser. Peptides and oligonucleotides were infused into an Apollo II electrospray ionization source at an ESI Flow rate of 100 μ L/h. The capillary voltages ranged from 3,500 to 3,800 V for negative-ion mode analysis. The drying gas flow rate and temperature were 4.0 L/min and 180°C, respectively, for all experiments. Ions were selected by the external quadrupole selected, accumulated in a hexapole for 1.0 to 5.0 seconds, and transported to the ICR cell for further activation and dissociation. CID experiments were performed in the collision cell at energies ranging from 15 to 20 V.

For niECD experiments, the cathode bias was set to - 4.0 to - 6.0 V with the ECD lens ranging from - 2.5 to - 4.5 V. Time domain data were Fourier transformed and resulting frequencies corresponding to m/z 200 to 2000 were displayed via ftmsControl software (version 2.1, Bruker Daltonics) at a data acquisition size of 1M summed over 64–128 scans. The data were analyzed by Compass DataAnalysis software (version 4.4 Bruker, Daltonics). Calculated m/z values for oligonucleotides and their product ions were obtained from Mongo Oligo Mass Calculator v2.08 (<http://mods.rna.albany.edu/masspec/Mongo-Oligo>). Calculated peptide mass lists were obtained from Protein Prospector v5.20.0 (<http://prospector.ucsf.edu/prospector/mshome.htm>).

4.2.4 Protein Digestion and LC/MS Separation

PRORP1 was first buffered exchanged into 50 mM NH_4CO_3 . 0.1 M dithiothreitol (DTT) was used to reduce possible disulfide bonds, the reaction was left to incubate for 45 minutes at 55° C. Alkylating agent iodoacetamide (IAA) was added to inhibit disulfide bond reformation, the reaction was left to react for 45 minutes. Finally, trypsin was added at a concentration of 1:100 trypsin:protein and was left to incubate overnight at 37° C. The reaction was quenched with 1 μL FA prior to LC/MS analysis. The sample was injected onto an Agilent 1100 HPLC system (Agilent, Wilmington, DE) via an Eclipse XDB reversed-phase C-18 column (2.1 x 150 mm, 5 μm particle size; Agilent) with a linear gradient from 2-98% B (95/5 acetonitrile/water with 0.1% formic acid) over 50 minutes. The eluent was introduced into the mass spectrometer and analyzed in positive-ion mode.

4.2.5 Click-Chemistry Reaction and LC/MS/MS via Data Independent Acquisition

The reaction was performed as described in the Oligo-Click-M-Reload Kit and as previously described.²⁹ 5 μL of the activator solution was added to the vial of catalyst beads. 40 μL of 300 μM RNA and 10 μL of 10 μM peptide solution were added to the reaction vial. The reaction was left to react on a water bath at 45° C for 4 hours. The

samples were then diluted to 10 μ M in 10 mM ETDA prior to analysis. Standard peptide mix (ACTH, CCK, rCGAUAC, insulin chain A, and Angiotensin I) was injected into an Agilent 1100 HPLC system (Agilent) via a Luna C18 reversed-phase column (25 cm x 1 cm, 5 μ m particle size; Phenomenex, Torrance, CA). Peptides were separated via a step-wise gradient, %B (95/5 acetonitrile/water with 0.1% FA) was increased from 1.0% to 15% over 10 minutes followed by an increase of 15-38% over 40 minutes. The eluent was introduced into the mass spectrometer and analyzed in negative-ion mode in Auto MS/MS serial mode without quadrupole isolation. In every other scan, the peptides were irradiated at 6.25 W for 150 ms. All product ion peaks were manually assigned within 10 ppm mass accuracy.

4.3 Results and Discussion

4.3.1 MS/MS of Non-covalent RNA-peptide Complexes

Upon negative-ion mode ESI of a substance P and rGCAUAC mixture, a 1:1 stoichiometric complex is observed at relatively high ion abundance (Figure 4.1), owing to the stability of salt bridges in the gas phase. Polarity and solution pH both have an effect on complex observation in the gas phase. The percentage of complex formation is given by:

$$\% \text{ Complex} = \left(\frac{\sum \text{Ion abundances corresponding to RNA-peptide complex}}{\sum \text{Ion abundances in spectrum}} \right) \times 100 \quad (\text{Equation 4.1})$$

All peaks are corrected for charge. At acidic pH, 3 and 5, only 0.8% and 0.7% complex is observed in positive ion mode, respectively. On the other hand, in negative-ion mode, 21% and 2% complex is seen. Optimal complex detection occurs at neutral pH; 27% complex is observed in negative-ion mode and 0.1 % in positive-ion mode. At basic pH, 8.5 and 11.5, 9% and 10% complex was observed in negative-ion mode whereas, in positive-ion mode, only 1% and 0.3% complex was detected. These data show the utility of negative-ion mode for probing non-covalent RNA-peptide complexes. In

positive-ion mode, the phosphates along the RNA backbone are protonated, thus hindering salt bridge formation with basic peptide side chains such as arginine.³⁰ Therefore, negative-ion mode fragmentation techniques are preferred.

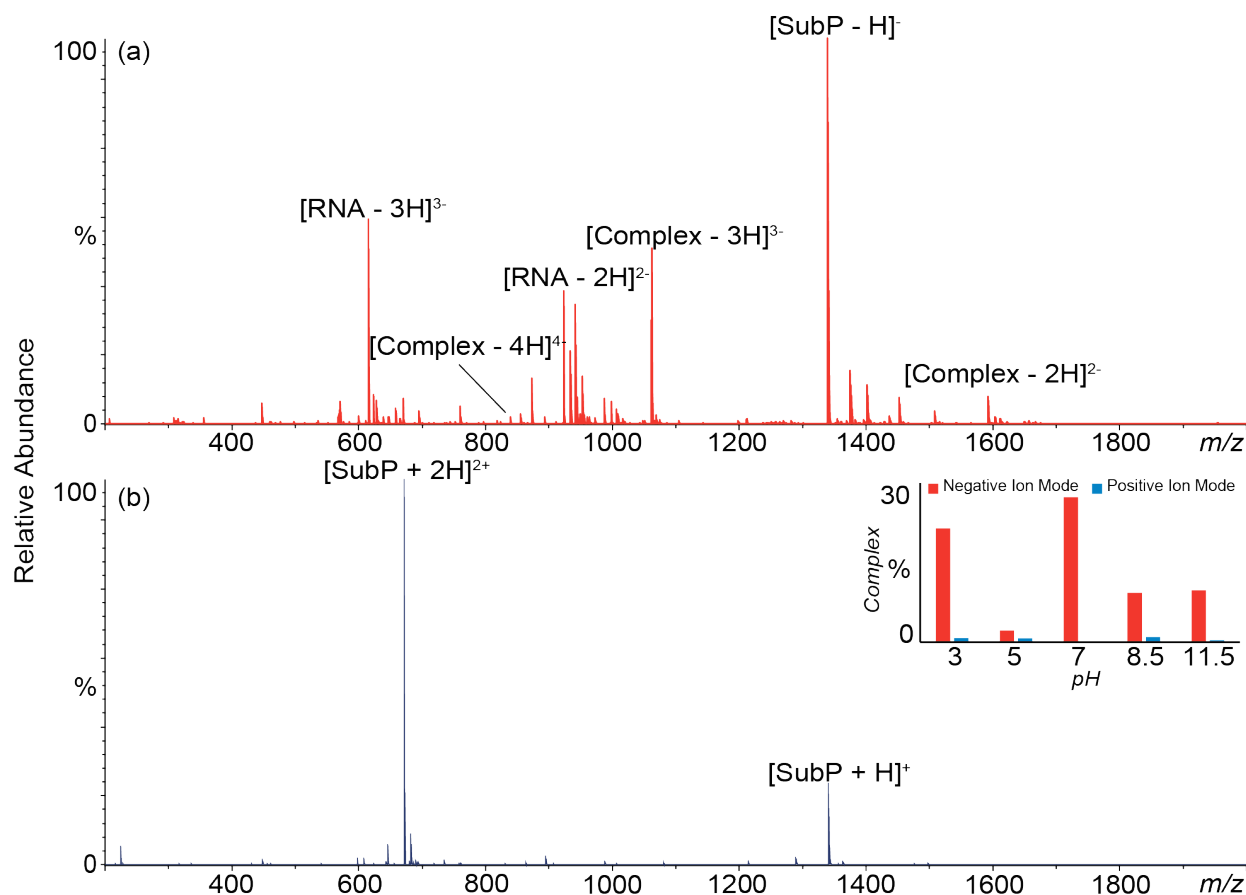


Figure 4.1. A. ESI mass spectrum of a non-covalent RNA-substance P complex in negative-ion mode (pH 7); B. positive-ion mode (pH 7). The percent RNA-peptide complex is significantly increased in negative ion-mode at neutral pH.

Upon collisional activation (15 V) of the RNA-angiotensin I complex, preferential disruption of the non-covalent interaction is observed (Figure 4.2a). The CID spectrum also shows extensive *c* and *y*-type fragmentation, corresponding to full sequence coverage of the RNA. However, limited fragmentation of the peptide moiety is observed with only *b*₈ and *y*₈ fragment ions produced. CID is a high-energy process, typically cleaving the most labile bonds within a molecule. In this case, the salt-bridge(s) formed between the peptide and the RNA was not sufficiently strong to survive collisional activation. Electron-based fragmentation techniques have been shown to retain labile

groups in the gas phase. The complex was subjected to electron irradiation (6.5 V cathode bias), Figure 4.2 B. The charge-increased species ($[\text{Complex} - 2\text{H}]^{2-\cdot}$) is observed but no fragments are generated.

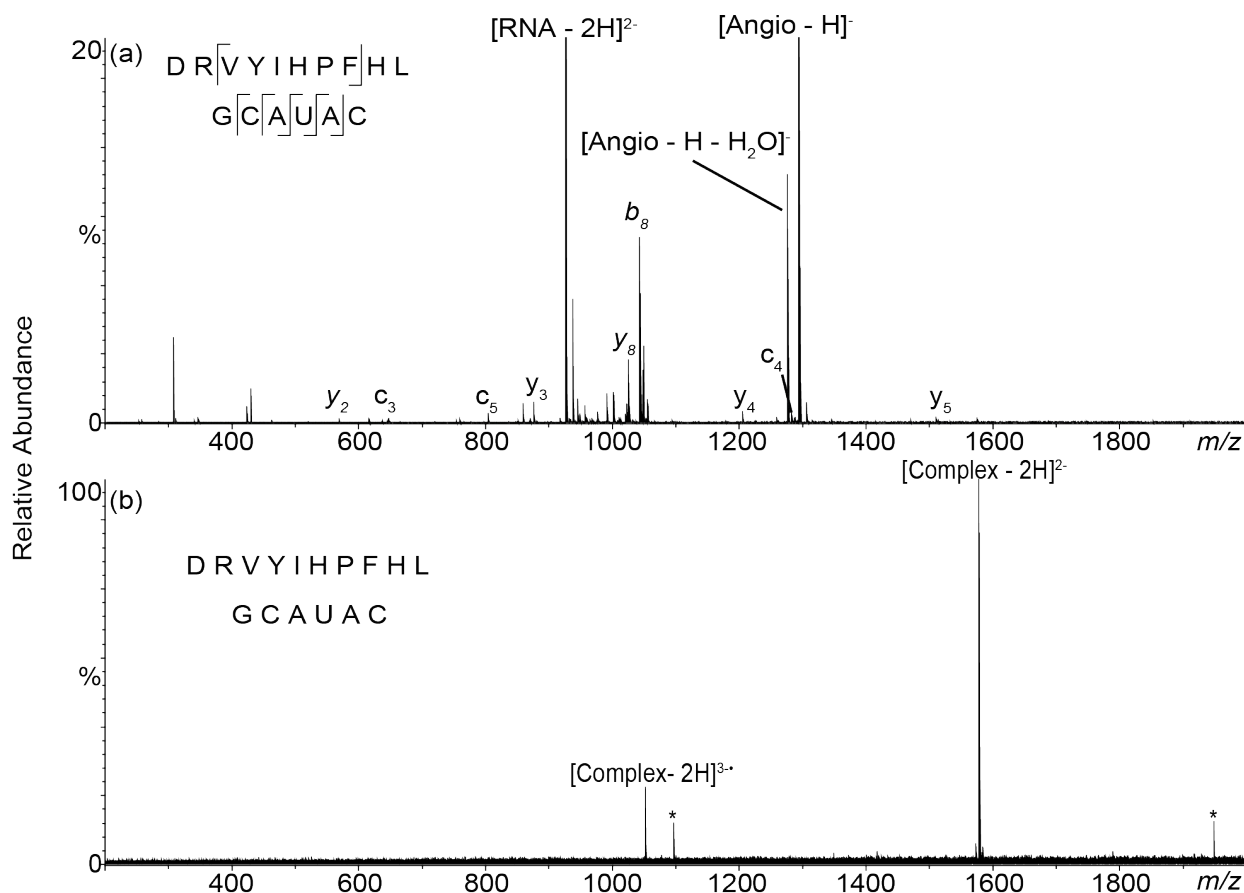


Figure 4.2. (a) CID (15 V) MS/MS of RNA-angiotensin I complex. Extensive fragmentation of the RNA moiety is observed with very limited fragmentation of the peptide; (b) niEC(D) spectrum of the doubly deprotonated RNA-angiotensin I complex. Electron capture is observed but no fragments are generated.

CID (20 V) of the RNA-substance P complex resulted in full sequence coverage of the RNA moiety via *c* and *y* ion series (Figure 4.3 A). The peptide moiety did not fragment. As in the previous example, the major fragmentation pathway is the dissociation of the RNA-peptide non-covalent interaction. niECD with supplemental IR activation (200 ms prior to electron irradiation) was able to preserve the intact complex. As shown in Figure 4.3 B, electron capture (to yield $[\text{Complex} - 2\text{H}]^{2-\cdot}$) is observed, along with y_2 , y_3 , and y_4 fragment ions from the RNA. Also observed are c_8 , c_{10} and y_9 fragment ions from the peptide. The site of interaction, however, is not elucidated.

Collisional activation is not a reliable technique for probing interaction sites within non-covalent RNA-peptide complexes in the absence of mostly basic residues, such as for the arginine rich tat peptide.²⁸ A possible rationale for the preferential dissociation of the RNA-peptide complex is that the utilized model peptides contain only a single arginine residue. As a result, there are limited charge-charge interactions holding the complex together compared with HIV TAR-tat non-covalent complex.

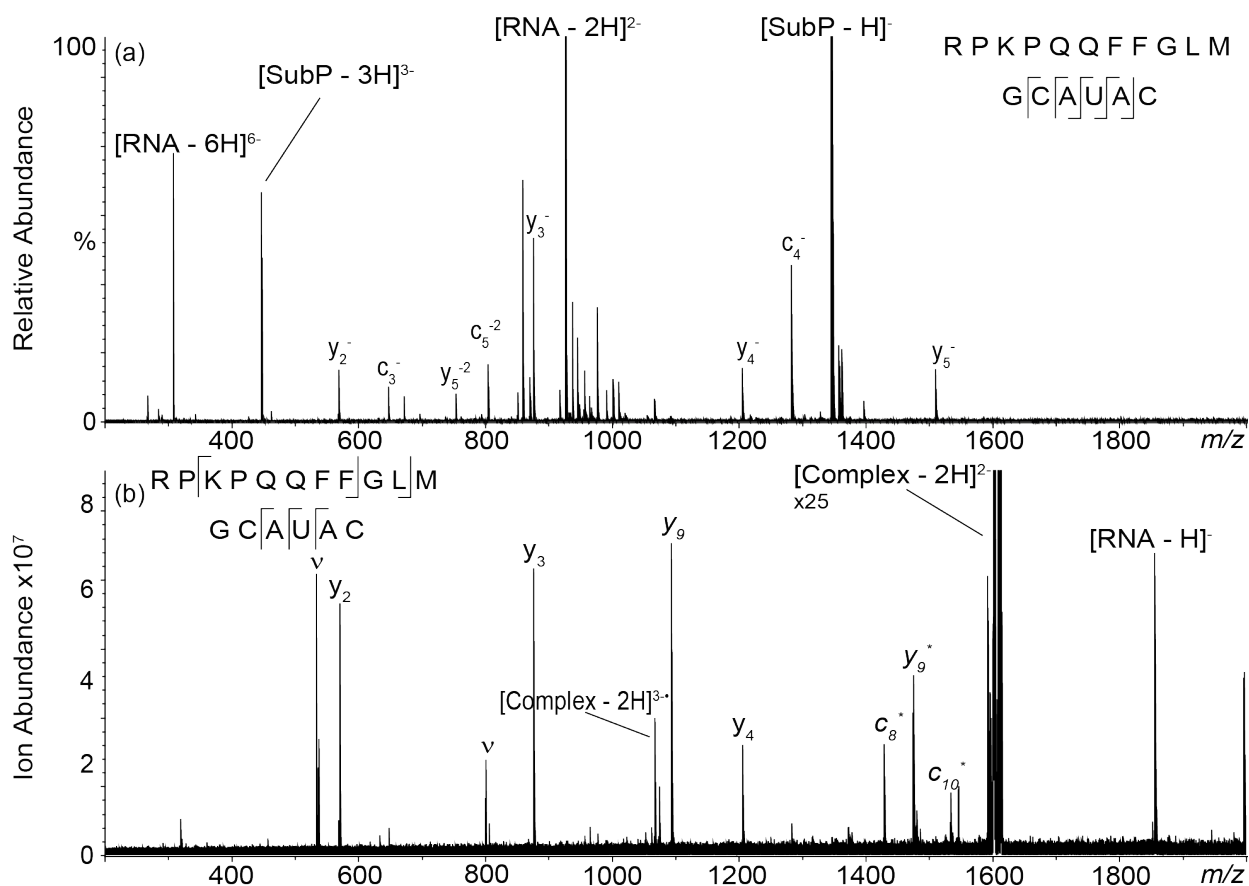


Figure 4.3. (a) CID (20 V) MS/MS spectrum of RNA-substance P complex. Extensive fragmentation of the RNA moiety is observed (blue) with no fragmentation of the peptide; (b) AI-niECD spectrum of the doubly deprotonated RNA-substance P complex.

4.3.2 Selective IRMPD of RNA-peptide Crosslinks

A PRORP enzyme from *Arabidopsis thaliana* (PRORP1), which localizes to mitochondria and catalyzes pre-tRNA processing similar to the human mitochondrial PRORP, has been crystallized.⁵ In order to build relevant RNA-peptide model systems,

mimicking RNA-peptide crosslinks for MS analysis of PRORP, a trypsin digest of the PRORP1 protein was first performed to identify candidate peptides (Figure 4.4). 90% sequence coverage was obtained from LC/MS analysis. The PRORP 1 derived peptide RGFDIFKQ was chosen for click chemistry.

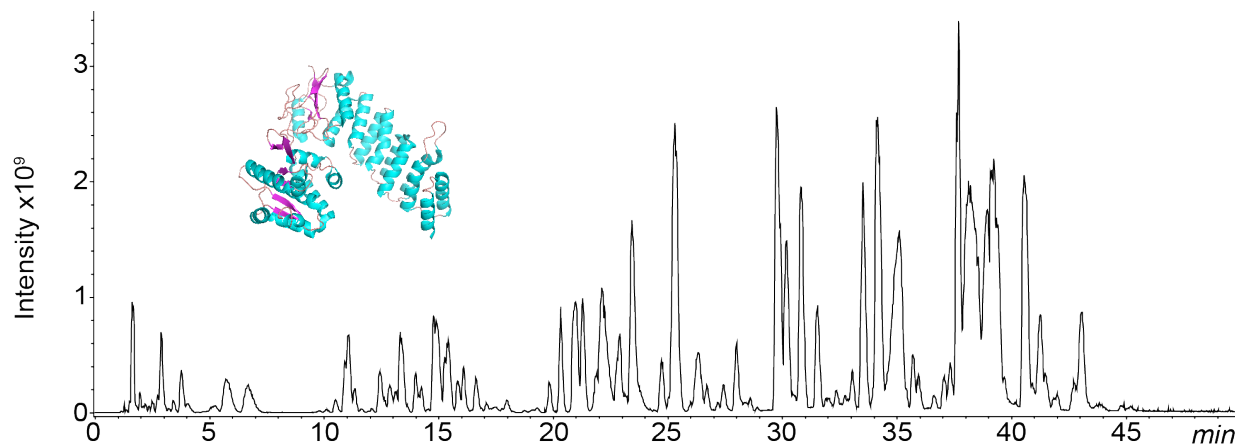
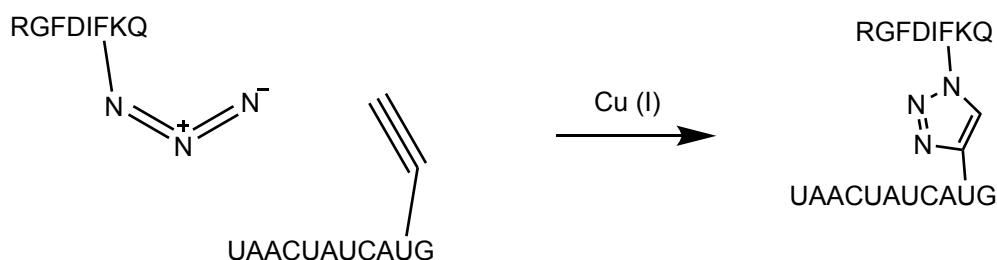


Figure 4.4. Total ion chromatogram of trypsin digested PRORP1 protein. About 90% sequence coverage was obtained following LC/MS of trypsin-digested protein (Inset) The crystal structure of proteinaceous RNase P 1 (PRORP1) from *A. thaliana*. PDB ID: 4G26.⁵

The PRORP1 derived peptide was synthesized with a 4-azidophenylalanine at position 8 and an alkyne modified 11-mer RNA sequence, containing 5EdU at position 10, was purchased. These two analytes were subjected to copper mediated click-chemistry to form a triazole linkage (Scheme 4.1). Confirmation of this linkage was performed via HPLC separation as shown in the extracted-ion chromatograms in Figure 4.5. The crosslinked species eluted at 19.7 minutes whereas the unreacted peptide eluted at 24.6 minutes. The free RNA (at lower concentration) was not observed. These conditions resulted in low crosslinking yield because there was an insufficient amount of starting RNA. Further investigation of reaction conditions is needed to optimize the crosslinking yield.



Scheme 4.1. Schematic of the click chemistry reaction for formation of a model RNA-peptide crosslink. 4-azidophenylalanine reacts with 5EdU via a copper mediated reaction to form a triazole linkage.²⁹

In order to differentiate crosslinked peptides from non-crosslinked peptides within a peptide mixture, five standard peptides and an RNA oligonucleotide were prepared at equimolar concentrations, separated by LC and introduced into a mass spectrometer equipped with IRMPD. The IR laser fired in every other scan at 6.25 W for 150 ms. Figure 4.5 shows the extracted ion chromatograms for each peptide before (black) and after (red) IR irradiation.

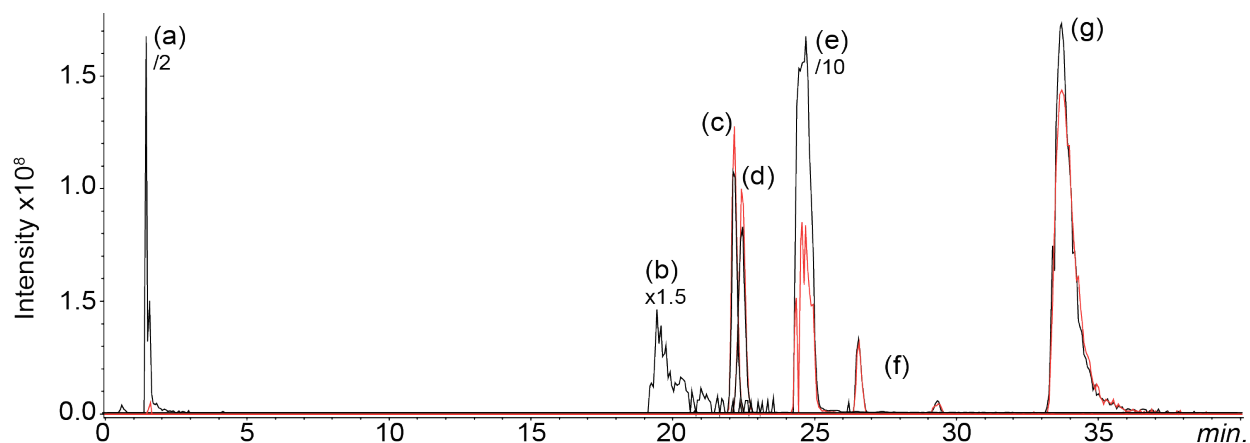


Figure 4.5. Extracted ion chromatograms for (a) rGCAUAC, (b) the synthetic crosslink, (c) ACTH 1-10, (d) angiotensin I, (e) 4-azidophenylalanine-containing PRORP1 tryptic peptide, (f) CCK, and (g) oxidized insulin chain A before (black) and after (red) IR irradiation for 150 ms at 6.25 W.

Peaks (a) and (b) correspond to the RNA oligonucleotide rGCAUAC and the crosslink, respectively. Upon IR irradiation, the abundance of Peaks (a) and (b) decreased by 96 and 88%, respectively. These two peaks correspond to the only phosphate containing species in the mixture. The observed selective dissociation is the result of the P-O stretching frequency being in resonance with the 10.6 μm photons.^{31,32} As shown in

Figure 4.6, upon IR irradiation, the RNA oligonucleotide fragments resulting in full sequence coverage.

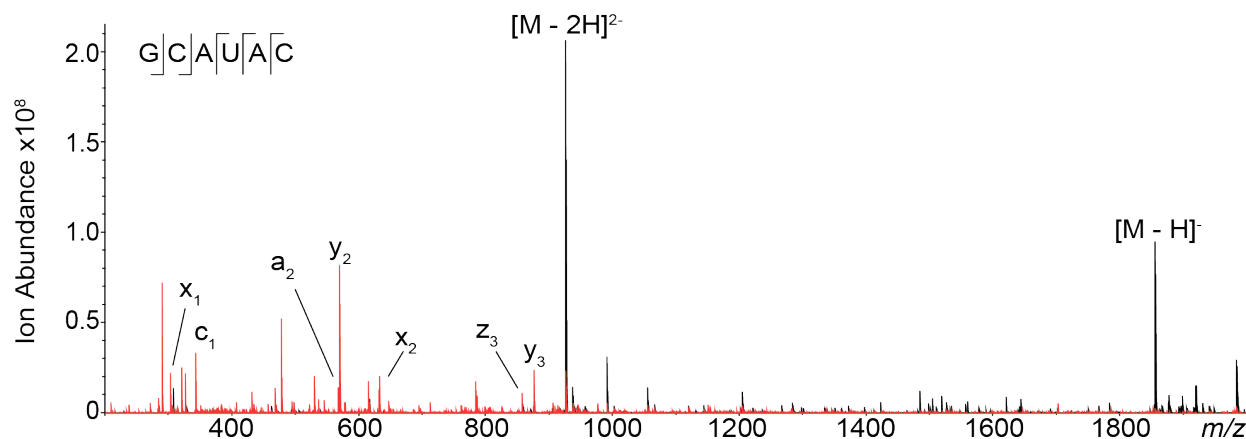


Figure 4.6. Mass spectrum of RNA hexamer, rGCAUAC, before (black) and after (red) IR irradiation.

For the RNA-peptide crosslink species (Fig. 4.6), c_1 , c_2 , c_3 , and c_4 product ions are observed from the RNA moiety but only a b_5 ion for the peptide moiety, demonstrating the utility of IR irradiation to sequence RNA-peptide crosslink species in an RNA-centric manner.

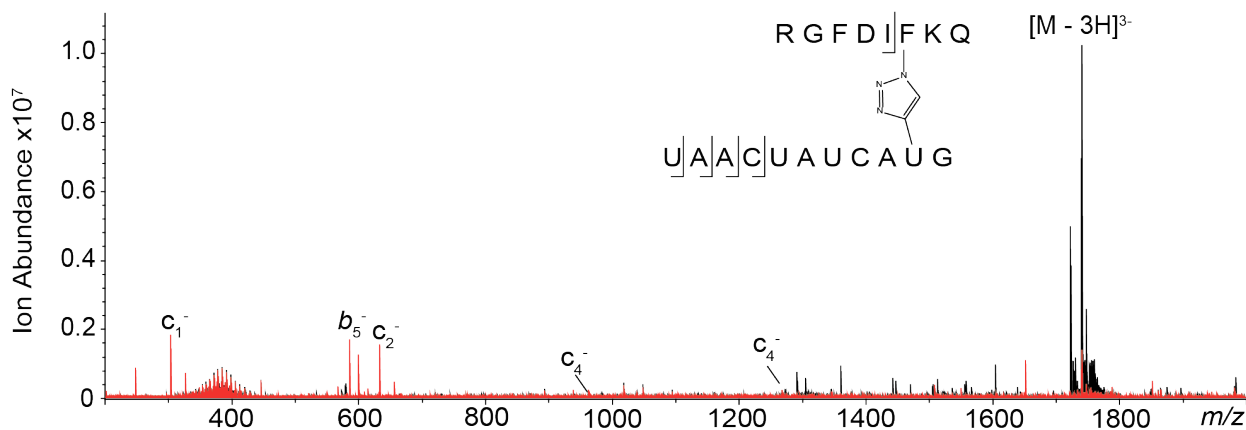


Figure 4.7: Mass spectrum of RNA-PRORP1 peptide crosslink species before (black) and after (red) IR irradiation. Peaks that are not annotated do not correspond to any sequence informative ions from the heteroconjugate.

Peptide ions lacking phosphates required ~six times longer IR irradiation times for similar degrees of dissociation. Peaks (c), (d) and (f) (Fig. 4.5), corresponding to the

peptides ACTH 1-10, angiotensin I, and CCK, changed by 12, 9.4, and 8%, respectively, upon IR irradiation. The absence of fragmentation for these peptides further demonstrates that non-phosphate containing peptides are not affected by IR irradiation at the current experimental conditions (6.25 W, 150 ms).

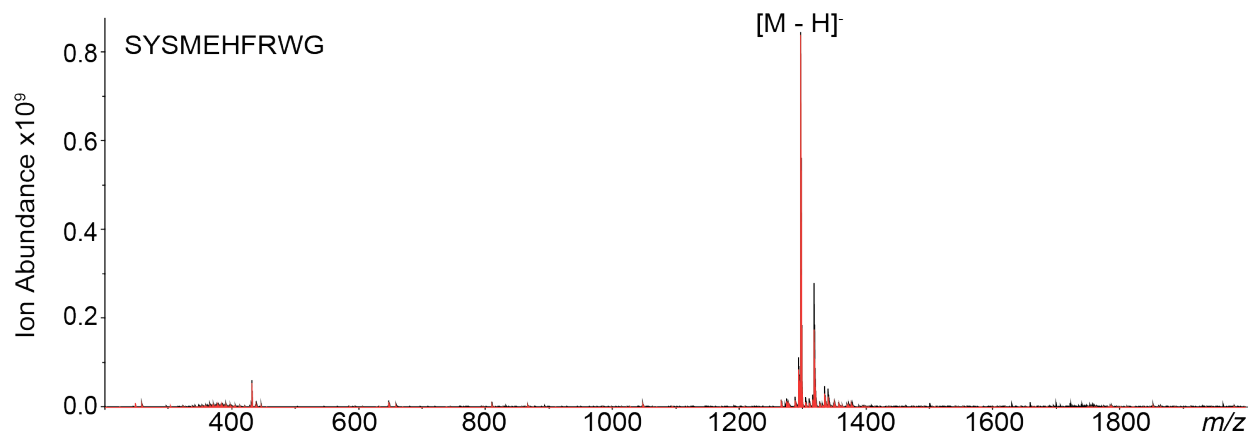


Figure 4.8. Mass spectrum of ACTH 1-10 peptide before (black) and after (red) IR irradiation.

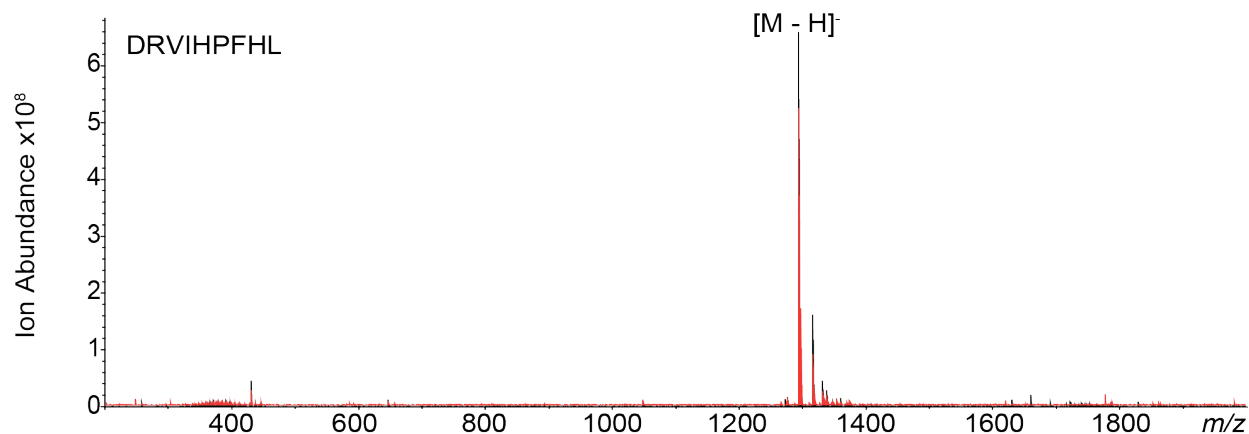


Figure 4.9. Mass spectrum of angiotensin I peptide before (black) and after (red) IR irradiation.

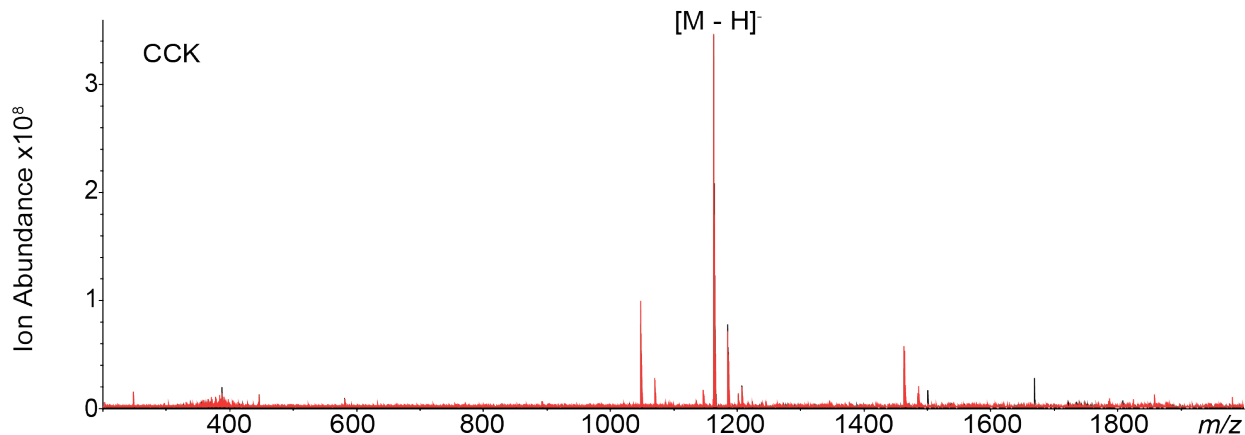


Figure 4.10. Mass spectrum of CCK peptide before (black) and after (red) IR irradiation.

Peak (g) (Fig. 4.5) corresponds to oxidized insulin chain A and decreased by 13%. In positive-ion mode, RSO_3H containing species have been shown to highly selectively absorb $10.6\ \mu\text{m}$ photons.^{33,34} This effect is not observed in negative-ion mode because the sulfate group is deprotonated (e.g., RSO_3^-), which changes the absorbance maximum.

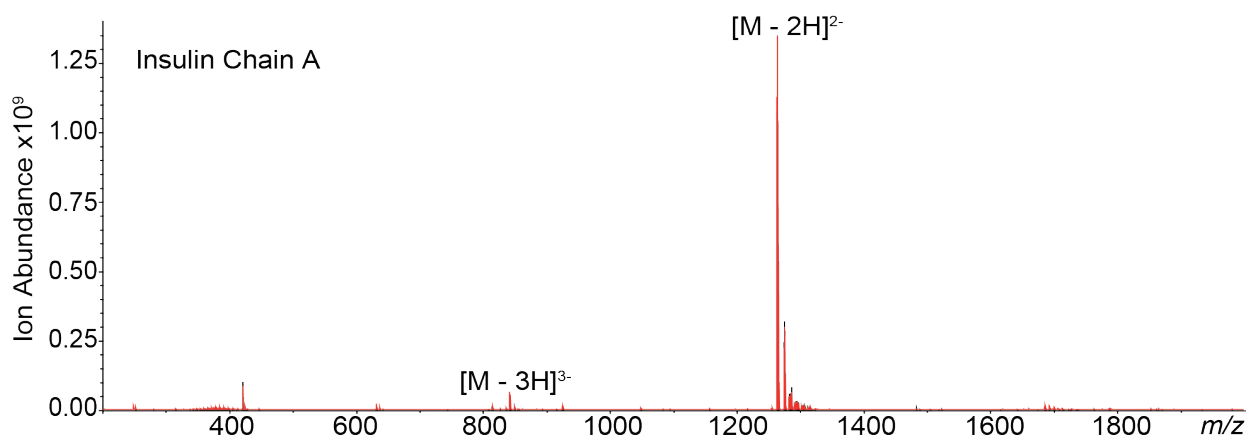


Figure 4.11. Mass spectrum of oxidized insulin chain A peptide before (black) and after (red) IR irradiation.

Peak (e) (Fig. 4.5) corresponds to the 4-azidophenylalanine-containing PRORP1 peptide. Upon IR irradiation, this peak decreases by 51%. This unexpected result may be due to unique gas-phase properties of the azide group. Previous computational and experimental determinations of N_3^\bullet and N_3^- vibrational spectra do not show evidence for absorption around $943\ \text{cm}^{-1}$ (corresponding to the $10.6\ \mu\text{m}$ photons utilized here).³⁵ However, a peptide-linked azide group may show absorption shifts. Also, as shown in

Figure 4.12, the absence of fragmentation suggests that the IR irradiation at 150 ms is not sufficient to induce fragmentation of the peptide. Nevertheless, the observed behavior introduces a possible false positive although azide groups are not typically used for RNA-protein photo-crosslinking. Further optimization of this technique (e.g., IR laser power and pulse length) is needed to obtain more extensive fragmentation whilst still remaining selective for phosphate containing molecules. Overall, the data presented suggest that IRMPD can be used as an effective tool for selectively dissociating RNA-peptide crosslinked species within a pool of tryptic unmodified peptides.

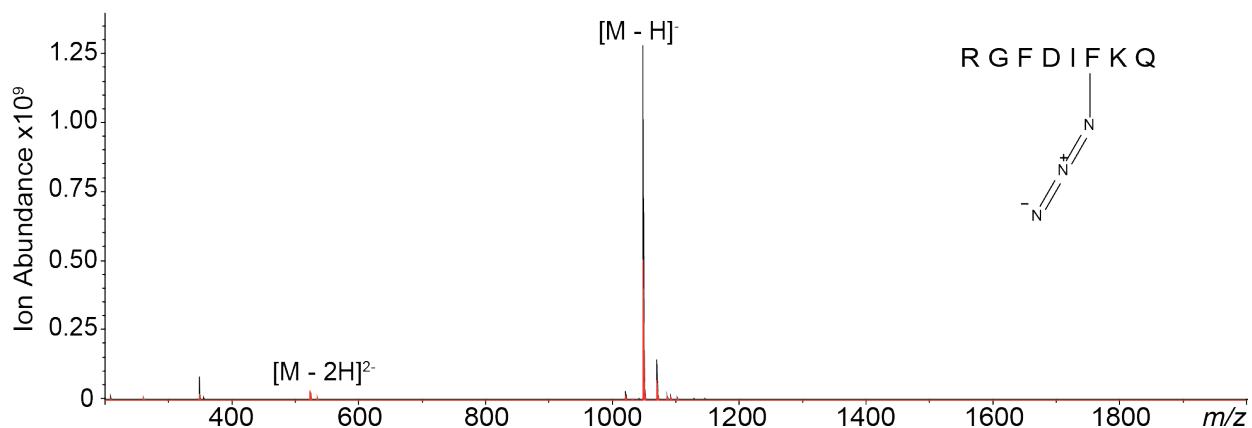


Figure 4.12: Mass spectrum of 4-azidophenylalanine-containing PRORP1 peptide before (black) and after (red) IR irradiation.

4.4 Conclusions

Slow heating MS/MS techniques (e.g., CID) resulted in near complete sequence information for the RNA moiety within peptide-RNA non-covalent complexes. Binding site information, however, is lost because the primary fragmentation pathway is dissociation of the complex. niECD, on the other hand, does not result in such dissociation, suggesting that niECD could be a potentially powerful technique for probing binding site information within non-covalent RNA complexes. Click-chemistry was used to produce stable, short-linker crosslinks, mimicking the crosslinked species produced by UV crosslinking approaches. Continued optimization of crosslinking conditions should improve crosslinking yield for improved information content in MS/MS spectra and allow for additional electron-based MS/MS techniques (e.g., niECD). We also examined the use of IRMPD to selectively identify RNA containing molecules.

Upon IR irradiation, fragmentation occurred for all RNA containing species within a peptide mixture, thus allowing for facile identification RNA-peptide crosslinked species. The data presented here introduce potential tools for identifying and elucidating RNA-peptide crosslinking sites within a tRNA-PRORP1 digest.

4.5 References

- (1) Draper, D. E. Themes in RNA-Protein Recognition. *J. Mol. Biol.* **1999**, *293*, 255-270.
- (2) Gesteland, R. F.; Cech, T. R.; Atkins, J. F. *The RNA World*; Cold Spring Harbor Laboratory Press: New York, 1999.
- (3) Holzmann, J.; Frank, P.; Löffler, E.; Bennett, K. L.; Gerner, C.; Rossmann, W. RNase P without RNA: Identification and Functional Reconstitution of the Human Mitochondrial tRNA Processing Enzyme. *Cell* **2008**, *135*, 462-474.
- (4) Walker, S. C.; Engelke, D. R. A Protein-only RNase P in Human Mitochondria. *Cell* **2008**, *135*, 412-414.
- (5) Howard, M. J.; Lim, W. H.; Fierke, C. A.; Koutmos, M. Mitochondrial Ribonuclease P Structure Provides Insight into the Evolution of Catalytic Strategies for Precursor-tRNA 5' Processing. *Proc. Natl. Acad. Sci.* **2012**, *109*, 16149-16154.
- (6) Schmidt, C.; Kramer, K.; Urlaub, H. Investigation of protein-RNA interactions by mass spectrometry-Techniques and applications. *J. Proteomics* **2012**, *75*, 3478-3494.
- (7) Kuhn-Holsken, E.; Lenz, C.; Sander, B.; Luhrmann, R.; Urlaub, H. Complete MALDI-ToF MS Analysis of Cross-linked Peptide-RNA Oligonucleotides Derived from Nonlabeled UV-irradiated Ribonucleoprotein Particles. *RNA* **2005**, *11*, 1915-1930.
- (8) Golden, M. C.; Resing, K. A.; Collins, B. D.; Willis, M. C.; Koch, T. H. Mass Spectral Characterization of a Protein-nucleic Acid Photocrosslink. *Protein Sci.* **1999**, *8*, 2806-2812.
- (9) Hagan, N.; Fabris, D. Direct Mass Spectrometric Determination of the Stoichiometry and Binding Affinity of the Complexes between Nucleocapsid Protein and RNA Stem-Loop Hairpins of the HIV-1 Ψ -Recognition Element. *Biochemistry* **2003**, *42*, 10736-10745.
- (10) Yu, E.; Fabris, D. Direct Probing of RNA Structures and RNA-Protein Interactions in the HIV-1 Packaging Signal by Chemical Modification and Electrospray Ionization Fourier Transform Mass Spectrometry. *J. Mol. Biol.* **2003**, *330*, 211-223.
- (11) Harris, M. E.; Christian, E. L. RNA Crosslinking Methods. *Methods Enzymol.* **2009**, *468*, 127-146.
- (12) Hoffman, E. A.; Frey, B. L.; Smith, L. M.; Auble, D. T. Formaldehyde crosslinking: a tool for the study of chromatin complexes. *J Biol Chem* **2015**, *290*, 26404-26411.

- (13) Sutherland, B. W.; Toews, J.; Kast, J. Utility of Formaldehyde Cross-linking and Mass Spectrometry in the Study of Protein-protein Interactions. *J. Mass Spectrom.* **2008**, *43*, 699-715.
- (14) Saito, I.; Sugiyama, H.; Matsuura, T. Photochemical Reactions of Nucleic Acids and Their Constituents of Photobiological Relevance. *Photochem. Photobiol.* **1983**, *38*, 735-743.
- (15) Kramer, K.; Hummel, P.; Hsiao, H.-H.; Luo, X.; Wahl, M.; Urlaub, H. Mass-spectrometric Analysis of Proteins Cross-linked to 4-thio-uracil- and 5-bromo-uracil-substituted RNA. *Int. J. Mass Spectrom.* **2011**, *304*, 184-194.
- (16) Gott, J. M.; Wiliis, M. C.; Koch, T. H.; Uhlenbeck, O. C. A Specific, UV-Induced RNA-Protein Cross-Link Using 5-Bromouridine-Substituted RNA. *Biochemistry* **1991**, *30*, 6290-6295.
- (17) Willis, M. C.; LeCuyer, K. A.; Meisenheimer, K. M.; Uhlenbeck, O. C.; Koch, T. H. An RNA Protein Contact Determined by 5 Bromouridine substitution, Photocrosslinking and Sequencing. *Nucleic Acids Res.* **1994**, *22*, 4947-4952.
- (18) Richter, F. M.; Hsiao, H. H.; Plessmann, U.; Urlaub, H. Enrichment of Protein-RNA Crosslinks from Crude UV-Irradiated Mixtures for MS Analysis by On-line Chromatography Using Titanium Dioxide Columns. *Biopolymers* **2009**, *91*, 297-309.
- (19) Kuhn-Holsken, E.; Dybkov, O.; Sander, B.; Luhrmann, R.; Urlaub, H. Improved Identification of Enriched Peptide RNA Cross-links From Ribonucleoprotein Particles (RNPs) by Mass Spectrometry. *Nucleic Acids Res.* **2007**, *35*, e95.
- (20) Larsen, M. R.; Thingholm, T. E.; Jensen, O. N.; Roepstorff, P.; Jorgensen, T. J. D. Highly Selective Enrichment of Phosphorylated Peptides from Peptide Mixtures Using Titanium Dioxide Microcolumns. *Mol. Cell Proteomics* **2005**, 873-886.
- (21) Flora, J. W.; Muddiman, D. C. Selective, Sensitive, and Rapid Phosphopeptide Identification in Enzymatic Digests Using ESI-FTICR-MS with Infrared Multiphoton Dissociation. *Anal. Chem.* **2001**, *73*, 3305-3311.
- (22) Crowe, M. C.; Brodbelt, J. S. Differentiation of Phosphorylated and Unphosphorylated Peptides by High-Performance Liquid Chromatography-Electrospray Ionization-Infrared Multiphoton Dissociation in a Quadrupole Ion Trap. *Anal. Chem.* **2005**, *77*, 5726-5734.
- (23) Gardner, M. W.; Vasicek, L. A.; Shabbir, S.; Anslyn, E. V.; Brodbelt, J. S. Chromogenic Cross-Linker for the Characterization of Protein Structure by Infrared Multiphoton Dissociation Mass Spectrometry. *Anal. Chem.* **2008**, *80*, 4807-4819.
- (24) Lenz, C.; Kuhn-Holsken, E.; Urlaub, H. Detection of Protein-RNA Crosslinks by NanoLC-ESI-MS/MS using Precursor ion Scanning and Multiple Reaction Monitoring (MRM) Experiments. *J. Am. Soc. Mass Spectrom.* **2007**, *18*, 869-881.
- (25) Kramer, K.; Sachsenberg, T.; Beckmann, B. M.; Qamar, S.; Boon, K. L.; Hentze, M. W.; Kohlbacher, O.; Urlaub, H. Photo-cross-linking and High-resolution Mass spectrometry for Assignment of RNA-binding sites in RNA-binding Proteins. *Nat. Methods* **2014**, *11*, 1064-1070.

- (26) Catron, B.; Caruso, J. A.; Limbach, P. A. Selective Detection of Peptide-oligonucleotide Heteroconjugates Utilizing Capillary HPLC-ICPMS. *J. Am. Soc. Mass. Spectrom.* **2012**, *23*, 1053-1061.
- (27) Kong, A. T.; Leprevost, V. F.; Avtonomov, D. M.; Mellacheruvu, D.; Nesvizhskii, A. MSFragger: Ultrafast and Comprehensive Identification of Peptides from Tandem Mass Spectra. *Nat. Methods* **2017**, *14*, 513-526.
- (28) Schneeberger, E. M.; Breuker, K. Native Top-Down Mass Spectrometry of TAR RNA in Complexes with a Wild-Type tat Peptide for Binding Site Mapping. *Angew. Chem. Int. Ed.* **2017**, *56*, 1254-1258.
- (29) Flett, F. J.; Walton, J. G.; Mackay, C. L.; Interthal, H. Click chemistry generated model DNA-peptide heteroconjugates as tools for mass spectrometry. *Anal. Chem.* **2015**, *87*, 9595-9599.
- (30) Woods, A. S.; Ferre, S. Amazing Stability of the Arginine-Phosphate Electrostatic Interaction. *J. Proteome Res.* **2005**, *4*, 1397-1402.
- (31) Little, D. P.; Speir, P. J.; Senko, M. W.; O'Connor, P. B.; McLafferty, F. W. Infrared Multiphoton Dissociation of Large Multiply Charged Ions for Biomolecule Sequencing. *Anal. Chem.* **1994**, *66*, 2809-2815.
- (32) Correia, C. F.; Balaj, P. O.; Scuderi, D.; Maitre, P.; Ohanessian, G. Vibrational Signatures of Protonated, Phosphorylated Amino Acids in the Gas Phase. *J. Am. Chem. Soc.* **2008**, *130*, 3359-3370.
- (33) Borotto, N. B.; McClory, P. J.; Martin, B. R.; Hakansson, K. Targeted Annotation of S-Sulfonylated Peptides by Selective Infrared Multiphoton Dissociation Mass Spectrometry. *Anal. Chem.* **2017**, *89*, 8304-8310.
- (34) Hofstadler, S. A.; Griffey, R. H.; Pasa-Tolic, L.; Smith, R. D. The Use of a Stable Internal Mass Standard for Accurate Mass Measurements of Oligonucleotide Fragment Ions Using Electrospray Ionization Fourier Transform Ion Cyclotron Resonance Mass Spectrometry with Infrared Multiphoton Dissociation. *Rapid Commun. Mass Spectrom.* **1998**, *12*.
- (35) Tian, R.; Facelli, J. C.; Michl, J. Vibrational and Electronic Spectra of Matrix-Isolated N,* and N3-. *J. Phys. Chem.* **1988**, *92*, 4073-4079.

Chapter 5

On-Chip Mixing for Colorimetric Quantitation of Salicylic Acid in Agar Microfluidic Channels: An Undergraduate Laboratory Experiment

5.1 Introduction

“Lab on a chip” technologies have gained much popularity over the past decade because high sensitivity is achieved with very little sample requirement (down to femto-liter amounts).¹⁻⁴ The field of microfluidics is revolutionizing chemical analysis as shown in the areas of clinical diagnostics, separations, DNA amplification, protein engineering, single cell analysis, to name a few.⁵⁻⁹ Microfluidic devices are typically on the micrometer scale and can manipulate extremely small amounts of fluids. In the on-going attempt to modernize undergraduate analytical chemistry curricula, many institutions have incorporated microfluidics as a tool to teach chemical principles.¹⁰⁻¹⁸

Photolithography is a common approach to device fabrication and polydimethylsiloxane (PDMS) is among the most common materials used.^{19,20} Yang et al. introduced a soft lithography workflow which utilizes cost effective everyday materials such as coffee stirrers, paper plates, and Jell-O to mimic conventional photolithographic workflows.²¹ However, attempts to implement this Jell-O-based laboratory in our introductory analytical chemistry course proved challenging due to the brittleness of Jell-O. We also sought to expand the experiment to include on-chip quantitative analysis but the strong color of Jell-O was not suitable for colorimetry. Therefore, we use agar as our molds. Agar provides several advantages, including being translucent and thus allowing fluids to be easily visualized as they flow through microfluidic channels. Agar, also, cures relatively quickly (~15 minutes), greatly reducing experimental time.

The laminar flow in microfluidic channels prevents effective mixing, thus making it challenging to probe chemical reactions. Chip geometries are typically modified in order

to circumvent this issue, such as introducing bumps and turns.²²⁻²⁴ Here we describe a novel experiment, which explores different channel geometries and solvent conditions to affect mixing in the agar-based microfluidic chip and uses image analysis (employing ImageJ, a Java-based image processing program freely available from the National Institutes of Health) to quantify the concentration of salicylic acid flowing through a microfluidic channel. Students can use their smart phones, similar to the acid-base titration experiment introduced by Nogueira et al. who used a free app for colorimetric analysis on wax printed paper,²⁵ or digital cameras available in the lab. Our experiment achieves several pedagogical goals, including (1) introduction of the fundamentals of microfluidics, (2) teaching the basics of lithography in the context of agar chip fabrication, (3) employing the designed chips to study fluid dynamics and mixing in the context of laminar vs. turbulent flow, and (4) quantitative analysis of salicylic acid via colorimetric analysis with Image J. We chose quantification of salicylic acid through complexation with iron (III) because the iron (III)–salicylate complex is highly colored and easily visualized in the microfluidic devices. RGB analysis is employed to construct a calibration curve as a function of salicylate concentration. This calibration curve is compared to a calibration curve constructed via visible spectrometry, an experiment performed earlier in the course).

5.2 Experimental Overview

This experiment is intended for two 4-hour lab periods in an introductory level analytical chemistry laboratory course (Quantitative Analysis Lab). Chip fabrication and characterization is accomplished in the first lab period. Students are encouraged to prepare multiple chips (at least 6) to ensure success of the experiment. Figure 5.1 shows various chip geometries: a straight “Y-channel”, “Zig-Zag”, and “90°” channels. Once the chips are constructed, students characterize them by determining whether their chips promote laminar or turbulent flow regimes (see below for detailed description). The final part of the experiment is the on-chip detection of iron-salicylate. Here, students use digital cameras or smart phones and ImageJ software to determine the concentration of various iron salicylate solutions by RGB analysis.

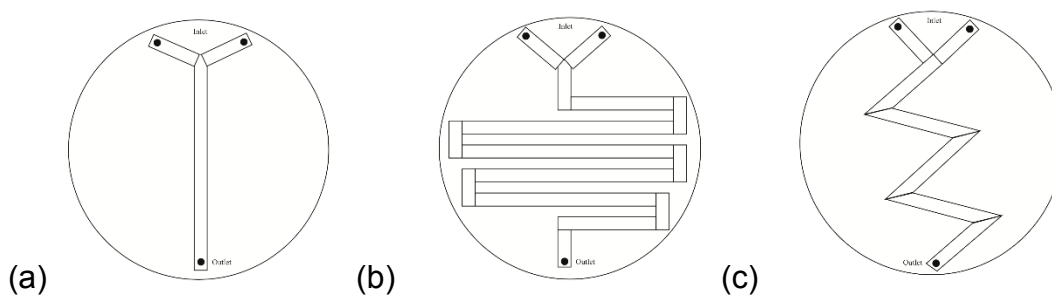


Figure 5.1. Outline of channel geometries that students will construct: “Y” channel (A), “90°” channel (B), and “Zigzag” channel. Figures are not drawn to scale.

5.2.1 Fabrication of Microfluidic Chips

The main materials used to create the molds are aluminum weighing pans, wooden coffee stirrers, and super glue. The coffee stirrers are cut into different shapes and sizes depending on the design of the mold and then glued onto the aluminum, creating a specific pattern. Students produce three types of molds (Figure 5.1): “Y-channel” molds, “Zig-Zag” molds, and “90°” molds. Students construct the desired shape molds on the aluminum weighing pans by cutting and super gluing the coffee stirrers to their desired geometries. The Graduate Student Instructor provides sample molds to ease the cutting process. It is important that the entire length of each segment of the mold is glued securely, as any loose pieces can be displaced when the agar is added, thus ruining the chip. The channel(s) are arranged so that the inlets and outlets are placed at the edges of the weighing pans. Once the coffee stirrers are glued to the pan, a light coat of nail polish is applied over the wooden stirrers. For each mold, 4.5 g of agar powder is added to 150 mL of boiling DI water and stirred constantly with a stir bar. To streamline the process, students are encouraged to use 600 mL of boiling water (1L glass beakers are provided for this purpose) and add 18 g of agar slowly/little by little to avoid clumps (this amount should be enough for four molds so repeated twice). NOTE: As soon as the agar has been added and the solution is cooling, it will begin to thicken immediately, making transfer of the solution difficult if the chips are not ready for immediate pouring. The agar mixture is slowly poured into the molds that were previously prepared,

ensuring that the coffee stirrers are covered completely. The filled molds are allowed to cool to room temperature on the lab bench until they begin to set. After the chips have cured, they are carefully peeled from the molds and placed on acrylic surfaces.

5.2.2 Characterization of Flow Regimes

Liquid flow is delivered at the “top” of the Y inlet by calibrated peristaltic pumps, previously used for titration-based experiments. The peristaltic pumps are set at flow rates in the range of 0.8-1.2 mL/min. To improve the robustness of the setup, the tubings are run through and held by “helping hands” (Figure 5.2). Blue and red colored water are slowly, but evenly, injected into the separate channels. The flow profile is documented with digital cameras or smart phones. The experiments are repeated with methanol-based solutions. Viscometers are used for viscosity measurements; triplicate measurements are taken. All chip geometries are characterized in the same way.

5.2.3 On-chip Detection of Salicylate

Five standard solutions of sodium salicylate are prepared in deionized water; 10 mM, 25 mM, 40 mM, 60 mM and 75 mM. The chip design/conditions that provided most effective mixing is the most ideal chip to use for this part of the experiment. Salicylate solutions are injected into one channel via one of the inlets whereas acidic 10 mM ferric nitrate solution is injected into the other. In cases where mixing was not achieved for any of the chip designs, students can mix 100 μ L of each salicylate solution with 10 mL ferric nitrate solution and then inject this mixture directly. For either scenario, it is very important to start with the lowest concentration, as the purple iron-salicylate solution tends to stain the channel in the chip. For RGB color analysis of the resulting images, the freeware ImageJ from the NIH is used.

5.2.4 Hazards

Students should be in proper personal protective equipment at all times when working in the laboratory. Heat gloves or “hot hands” are strongly recommended when working with the boiling agar solutions. Laboratory gloves are also recommended when handling iron salicylate and acidic ferric nitrate solutions.

5.3 Results and Discussion

5.3.1 Chip Fabrication

The soft lithography technique, used to fabricate the chip, was adapted from the method of Yang et al.²¹ The changes made to their method provided many benefits. The agar being translucent allowed for clear visualization of on-chip mixing, in contrast to a Jell-O based mold that is highly colored. Also, the agar cured in roughly 10 minutes whereas it takes Jell-O up to several hours to cure. Students are thus able to prepare many more chips in the event that some of their chips break. Finally, agar is much more sturdy once cured than Jell-O. Another change was that double-sided tape was replaced by superglue. Along with the light coat of nail polish, the glued coffee stirrers made for very fine, uniform channels. Finally, the cured chips were placed on acrylic surfaces for analysis. The acrylic surface created a superior seal with the agar mold compared with the previously used aluminum dishes, preventing any fluid from escaping the channels. Students are able to prepare at least six chips in the first two hours of the first day of the two-part experiment. The ease of the protocol introduces students to lithography techniques in the context of fabricating microfluidic devices. Also, students are given the opportunity to be creative and design a chip, which they believe will provide optimal mixing.

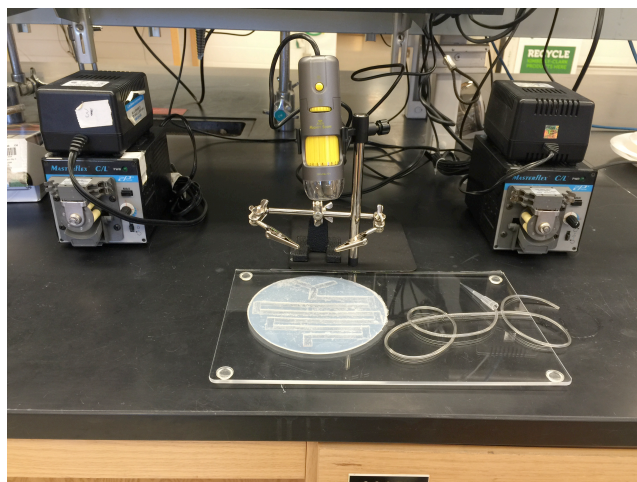


Figure 5.2. Photo of experimental setup.

5.3.2 Characterization of chip: The Reynolds's Number

The microfluidic chips are characterized by their ability to promote either laminar or turbulent flow. One consequence of laminar flow is that turbulent mixing of fluids does not occur, which is a major problem when attempting to perform reactions on chip, in our case attempting to mix iron (III) and salicylate on the chip. A number of dimensionless parameters exist that govern the behavior of fluids in microfluidic channels. For example, the Reynolds number (R_e) relates inertial to viscous forces, the Peclet number relates convection to diffusion, and the capillary number relates viscous forces to interfacial forces. In this experiment, students focus on R_e , as its variables are easily manipulated to alter the R_e value:

$$R_e = \frac{LV\rho}{\mu} \quad (\text{Equation 5.1})$$

in which L is the channel length, V is the average fluid velocity, ρ is the fluid density, and μ is the dynamic viscosity. As the R_e increases, inertial forces dominate, destabilizing the flow, and resulting in irregular turbulence. The transition from laminar to turbulent flow regimes in a straight circular pipe occurs at R_e between 2,000 and 3,000. Students use these numbers to differentiate flow regimes (Table 1)²⁶. The effect of R_e is demonstrated by having students manipulate channel geometry and solvent viscosity in

order to achieve on-chip mixing. Students use blue and red food coloring dye to visualize the fluid dynamics.

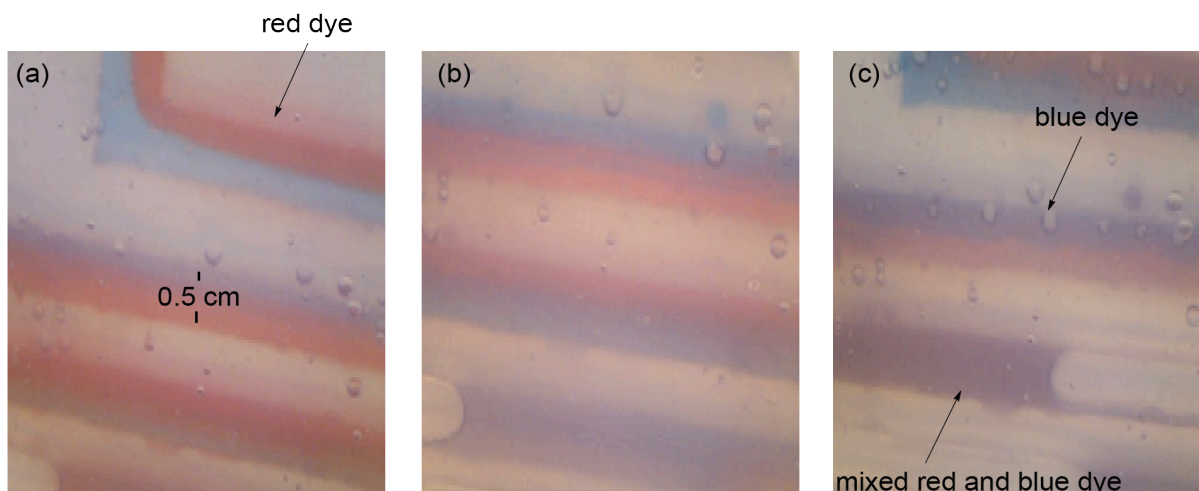


Figure 5.3. Representative photos taken from 90° turning channels on student-constructed chips; (a) Pure water; the flow remains laminar with the red and blue dye flowing side by side. (b) 50/50 water/methanol; little mixing is observed. (c) Pure methanol; mixing is observed. Photos were taken of the same region of the channel. The width of the channel is 0.5 cm.

Figure 5.3 shows red and blue color dye as they are introduced in the two separate inlets and flow through the “90°” chip geometry. The flow remains laminar through the channel when pure water is used (Figure 5.3a). As the methanol to water ratio increases, students observe more mixing in the channels (Figure 5.3b-c). We observe similar behavior with the other two channel geometries: mixing of the red and blue color dyes was not observed with 100% water despite chip geometries with sharp turns (Figure 5.4a-c). Increasing the methanol content to 50% promoted mixing in the “Zig-Zag” and “90°” channels (Figure 5.4e and f, respectively). Very little to no mixing, however, was observed in the “Y” channel despite increased methanol composition (Figure 5.4d), presumably because angled turns are needed to promote turbulent mixing.

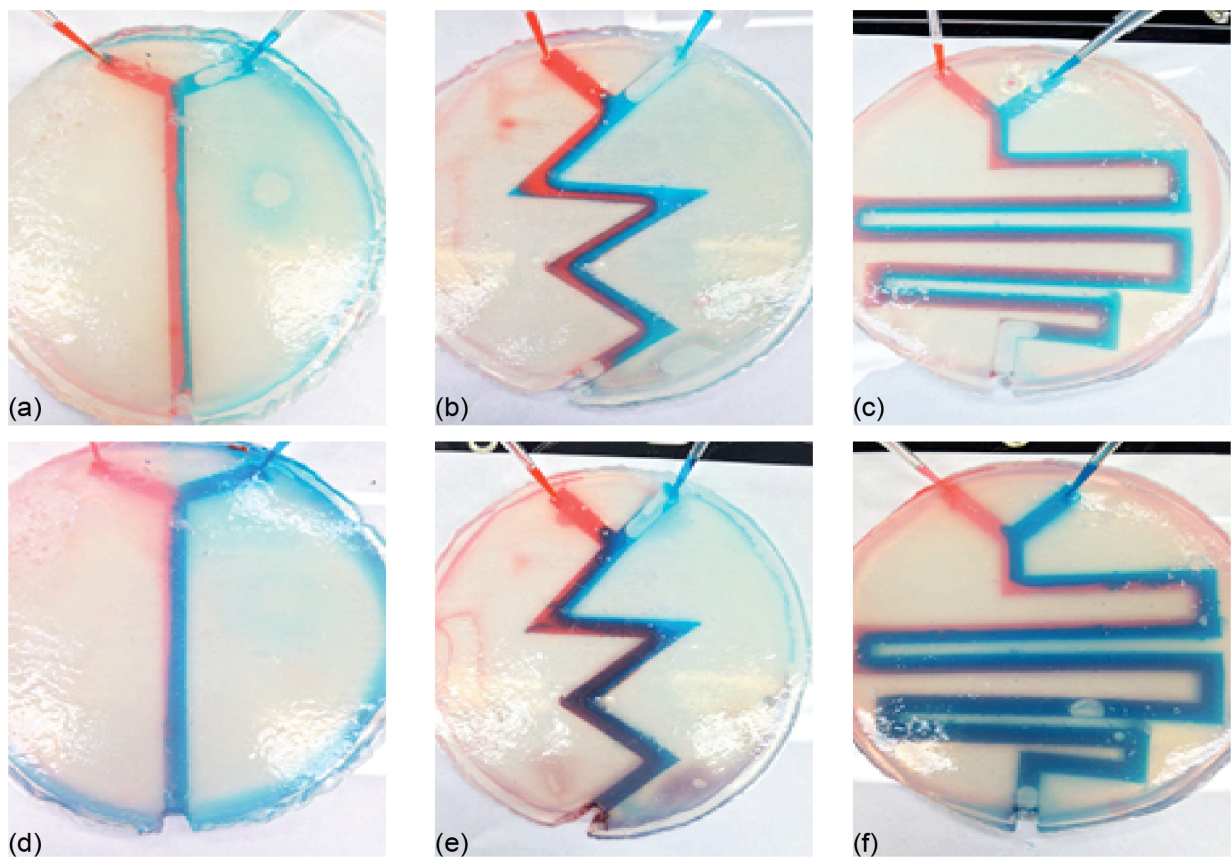


Figure 5.4. Photographs of student-constructed microfluidic devices. Channels a-c have colored water flowing through the channels. Despite varying the channel geometry, the flow remains laminar. Channels d-f contain 50% methanol dye solutions. In these cases, mixing is observed. However, despite this fluid composition, very little to no mixing was observed in the “Y” channels (d).

The “90°” channel geometry generally showed the most effective mixing, likely due to the long channel length and the number of corners. The determined Re for the “90°” geometry was highest among the chip geometries, as shown in Table 1. The “Y” channel had the lowest Re with flows being almost exclusively laminar. One interesting observation to note regarding Table 1 is that the Re was much lower for the 50/50 water/methanol mixtures across all geometries because viscosity does not vary linearly with increasing methanol content (Figure 5.5). As methanol and water mix, the mixture moves away from ideality.²⁷ Intermolecular forces (i.e., hydrogen bonds) increase, which results in a more viscous fluid. The viscosity peaks around 55% methanol content and then drops back down when the solution becomes more pure.

Table 5.1| R_e as a function of methanol composition and channel geometry

Channel Geometry	Percent Methanol	Reynolds Number (R_e)
"Y"	0	256
	50	125
	100	296
"Zig-Zag"	0	430
	50	210
	100	496
"90°"	0	1530
	50	748
	100	1770

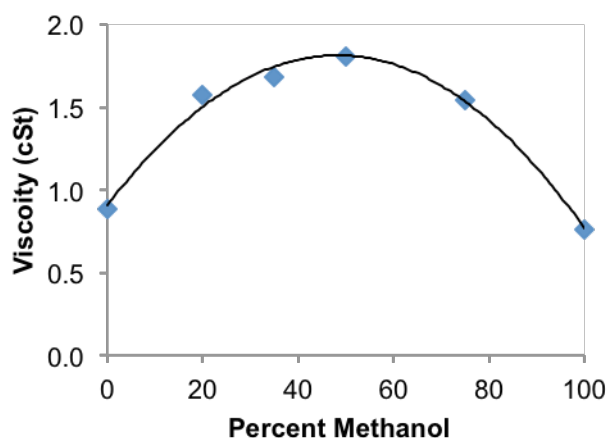


Figure 5.5. Measured kinematic viscosity as a function of methanol composition at room temperature.

5.3.3 On-chip detection

In the second week of the experiment, students use RGB analysis to quantify salicylate concentration and generate a calibration curve. They compare this calibration curve to one generated via visible spectrometry analysis, an experiment performed earlier in the course). We take advantage of the fact that iron (III)–salicylate complexes are highly colored. As the concentration of salicylate in solution increases, the solution becomes darker (Figure 5.6).

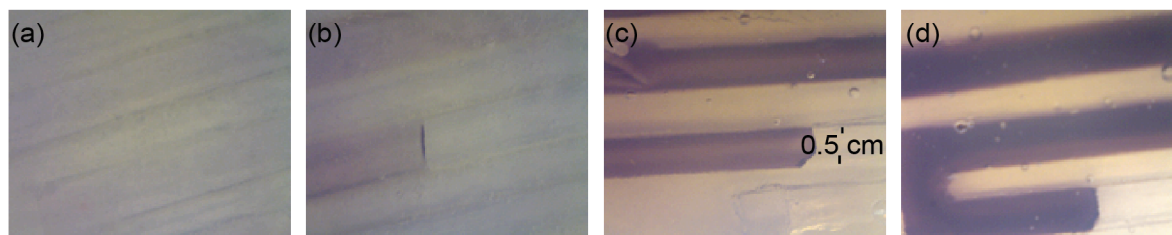
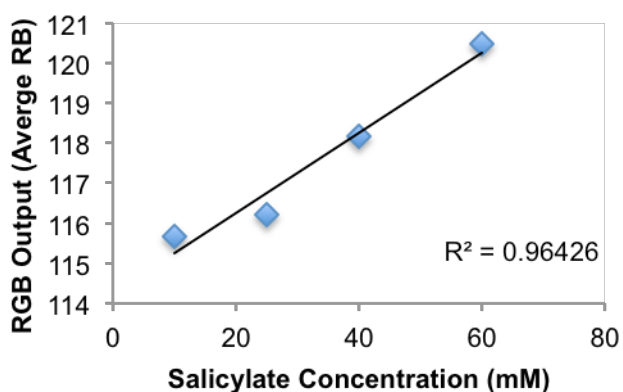


Figure 5.6. Iron (III)–salicylate solutions at increasing concentrations of salicylate. The width of the channel is 0.5 cm.

Students use smart phones or digital cameras to capture images of the solutions at the outlet end of the microfluidic channels. Students then transfer these images to the ImageJ software in which they are able to calculate the RGB of the purple solution. Because the iron (III)-salicylate complex is purple, red and blue color is likely most representative $(\text{red}(\text{mean}) + \text{blue}(\text{mean}))/2$. However, students are encouraged to attempt to utilize solely the blue and red output as well. For generation of a calibration curve, students plot RB (average), R, or B vs. concentration. In an RGB scale, the intensity of the color is defined as an integer between 0 and 255. As the intensity of the color decreases, so does the RGB value. In order to plot the calibration curve with a positive slope, it is necessary to subtract the RB (average), R, or B values from 255 and plot them against the known concentrations.



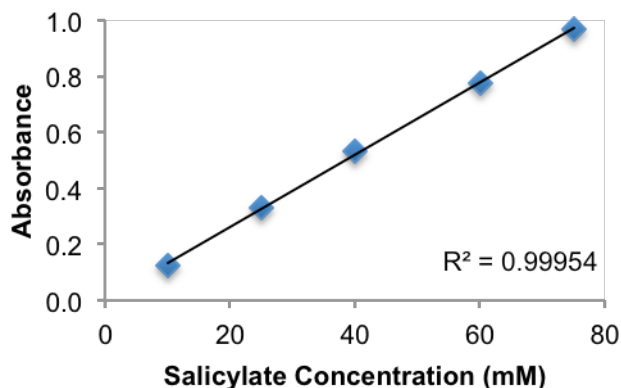


Figure 5.7. Representative calibration curves from student-constructed microfluidic device (top) and from visible spectroscopy (bottom). Very good correlation is observed between the RGB analysis and salicylate concentration with an R^2 value of 0.96, which is only slightly lower than for the absorbance vs. salicylate curve.

Figure 5.7 shows that very good correlation between RGB and salicylate concentration can be achieved. It is important to note that, in order to obtain reproducible data, students must carefully adjust lighting and capture images in the same region of the channel for each concentration. In cases where students elected to use their smartphones to capture images, higher resolution was achieved as the smartphone cameras handled lighting in a superior manner. Nevertheless, the data are promising as they suggest that agar-based microfluidic devices can be used to quantify unknown concentrations of analytes.

5.3.4 Student Responses

We surveyed two laboratory sections before and after completion of the experiment, 25 total students completed the survey. The goal of the survey was to gauge the level of knowledge of microfluidics, fluid dynamics, and chip fabrication that the students had prior to performing the experiment.^{15,28} The post survey gauged the level of confidence the students possessed on the aforementioned topics. Figure 5.8 summarizes the results of the survey. Students responded to a series of statements with values ranging from 1 to 5, with strong disagreement as 1 and strong agreement as 5, respectively. Overall knowledge and understanding of microfluidics increased after completing this

experiment. Students also felt much more confident overall that they could explain basic fundamentals of microfluidics to their peers.

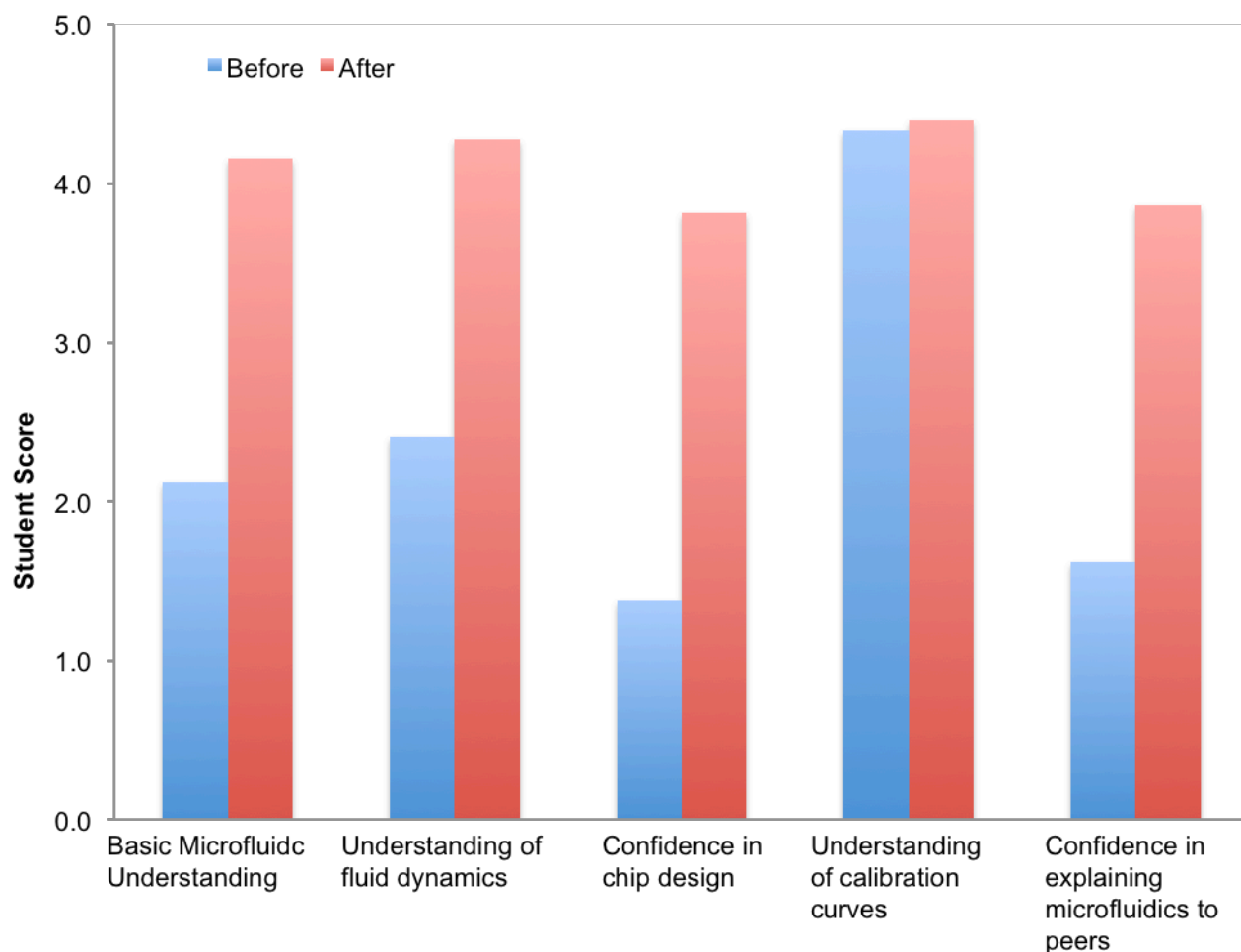


Figure 5.8. Results of student surveys: We surveyed students across two sections (N = 47) before and after they completed the microfluidics experiment. Students replied to a series of statements with values that ranged from 1 (strongly disagree) to 5 (strongly agree).

5.4 Conclusion

The agar-based microfluidic experiment described here provides students with an inexpensive introduction to the field of microfluidics. Pedagogically, this experiment introduces students to the fundamentals of lithography, in the context of chip fabrications. Students also learn about fluid dynamics in microfluidic channels. In addition, students have the opportunity to be creative with everyday materials as they

design and optimize their own devices. We are currently working on expanding this experiment and introducing an unknown sample component in which students will use their calibration curve to determine an unknown amount of salicylate. The described experiment can be performed in high school and undergraduate laboratory courses everywhere.

5.5 References

- (1) Teh, S. Y.; Lin, R.; Hung, L. H.; Lee, A. P. Droplet microfluidics. *Lab Chip* **2008**, *8*, 198-220.
- (2) Zhu, Y.; Fang, Q. Analytical detection techniques for droplet microfluidics--a review. *Anal. Chim. Acta.* **2013**, *787*, 24-35.
- (3) Puleo, C. M.; Wang, T. H. Microfluidic means of achieving attomolar detection limits with molecular beacon probes. *Lab Chip* **2009**, *9*, 1065-1072.
- (4) Li, Y.; Xuan, J.; Song, Y.; Wang, P.; Qin, L. A microfluidic platform with digital readout and ultra-low detection limit for quantitative point-of-care diagnostics. *Lab Chip* **2015**, *15*, 3300-3306.
- (5) Wheeler, A. R.; Thronset, W. R.; Whelan, R. J.; Leach, A. M.; Zare, R. N.; Liao, Y. H.; Farrell, K.; Manger, I. D.; Daridon, A. Microfluidic Device for Single-Cell Analysis. *Anal. Chem.* **2003**, *75*, 3581-3586.
- (6) Whitesides, G. M. The Origins and the Future of Microfluidics. *Nature* **2006**, *442*, 368-373.
- (7) Dittrich, P. S.; Manz, A. Lab-on-a-chip: Microfluidics in Drug Discovery. *Nat. Rev. Drug Discov.* **2006**, *5*, 210-218.
- (8) Wade, J. H.; Jones, J. D.; Lenov, I. L.; Riordan, C. M.; Sligar, S. G.; Bailey, R. C. Microfluidic platform for efficient Nanodisc assembly, membrane protein incorporation, and purification. *Lab Chip* **2017**, *17*, 2951-2959.
- (9) Doonan, S. R.; Bailey, R. C. K-Channel: A Multifunctional Architecture for Dynamically Reconfigurable Sample Processing in Droplet Microfluidics. *Anal. Chem.* **2017**, *89*, 4091-4099.
- (10) Chia, M. C.; Sweeney, C.; Odom, T. W. Chemistry in Microfluidic Channels. *J. Chem. Ed.* **2011**, *88*, 461-464.
- (11) Piunno, P. A. E.; Zetina, A.; Chu, N.; Tavares, A. J.; Noor, M. O.; Petryayeva, E.; Uddayasankar, U.; Veglio, A. A Comprehensive Microfluidics Device Construction and Characterization Module for the Advanced Undergraduate Analytical Chemistry Laboratory. *J. Chem. Ed.* **2014**, *91*, 902-907.
- (12) Feng, Z. V.; Edelman, K. R.; Swanson, B. P. Student-Fabricated Microfluidic Devices as Flow Reactors for Organic and Inorganic Synthesis. *J. Chem. Ed.* **2015**, *92*, 723-727.
- (13) Hemling, M.; Crooks, J. A.; Oliver, P. M.; Brenner, K.; Gilbertson, J.; Lisensky, G. C.; Weibel, D. B. Microfluidics for High School Chemistry Students. *J. Chem. Ed.* **2014**, *91*, 112-115.

- (14) Gerber, L. C.; Kim, H.; Riedel-Kruse, I. H. Microfluidic assembly kit based on laser-cut building blocks for education and fast prototyping. *Biomicrofluidics* **2015**, *9*, 064105.
- (15) Morton, J. A.; Bridle, H. Student-led microfluidics lab practicals: Improving engagement and learning outcomes. *Biomicrofluidics* **2016**, *10*, 034117.
- (16) Fintschenko, Y. Education: A modular approach to microfluidics in the teaching laboratory. *Lab Chip* **2011**, *11*, 3394-3400.
- (17) Nguyen, D.; McLane, J.; Lew, V.; Pegan, J.; Khine, M. Shrink-film microfluidic education modules: Complete devices within minutes. *Biomicrofluidics* **2011**, *5*, 22209.
- (18) Greener, J.; Tumarkin, E.; Debono, M.; Dicks, A. P.; Kumacheva, E. Education: a microfluidic platform for university-level analytical chemistry laboratories. *Lab Chip* **2012**, *12*, 696-701.
- (19) McDonald, J. C.; Duffy, D. C.; Anderson, J. R.; Chiu, D. T.; Wu, H.; Schueller, O. J. A.; Whitesides, G. M. Fabrication of microfluidic systems in poly(dimethylsiloxane). *Electrophoresis* **2000**, *21*, 27-40.
- (20) Ng, J. M. K.; Gitlin, I.; Stroock, A. D.; Whitesides, G. M. Components for Integrated Poly(dimethylsiloxane) Microfluidic Systems. *Electrophoresis* **2002**, *23*, 3461-3473.
- (21) Yang, C.; Ouellet, E.; Lagally, E. T. Using Inexpensive Jell-O Chips for Hands-On Microfluidics Education. *Anal. Chem.* **2010**, *82*, 5408-5414.
- (22) Chen, H.; Meiners, J.-C. Topologic mixing on a microfluidic chip. *Appl. Phys. Lett.* **2004**, *84*, 2193-2195.
- (23) Stroock, A. D.; Dertinger, S. K. W.; Ajdari, A.; Mezic, I.; Stone, H. A.; Whitesides, G. M. Chaotic Mixer for Microchannels. *Science* **2002**, *295*, 647-651.
- (24) Lee, C. Y.; Chang, C. L.; Wang, Y. N.; Fu, L. M. Microfluidic mixing: a review. *Int. J. Mol. Sci.* **2011**, *12*, 3263-3287.
- (25) Nogueira, S.; Sousa, L.; Silva, N.; Rodrigues, P.; Coltro, W. Monitoring Acid-Base Titrations on Wax Printed Paper Microzones Using a Smartphone. *Micromachines* **2017**, *8*, 139.
- (26) Squires, T. M. Microfluidics: Fluid Physics at the Nanoliter Scale. *Rev. Mod. Phys.* **2005**, *77*, 977-1026.
- (27) Colin, H.; Diez-Masa, J. C.; Guiochon, G.; Czajkowska, T.; Miedziak, I. The Role of the Temperature in Reversed-Phase High-Performance Liquid Chromatography Using Pyrocarbon-Containing Adsorbents. *J. Chromatogr.* **1978**, *167*, 41-65.
- (28) Hill, B. W. Using College Chemistry to Influence Creativity. *J. Res. Sci. Teach.* **1976**, *13*, 71-77.

5.6 Forms

Figure 5.9. Pre-lab protocol provided to students

Experiment 6: Introduction to Microfluidics

(Adapted from Yang et al. *Anal. Chem.* **2010**, *82*, 5408–5414)

1. Introduction: Goals of Experiment and Background

The goal of this experiment is to teach you some fundamentals of microfluidics, especially laminar vs. turbulent flow and the difficulty of on-chip mixing of fluids. Your objective is to construct channels (using coffee stirrers) of varying geometry in Agar and then study the effect of solvent viscosity on mixing of red and blue food color on the chip. Digital cameras are available for documenting your results. If mixing is feasible, you will mix iron(III) and salicylate on the chip to construct calibration curves for salicylate concentration and compare image analysis (employing ImageJ, a Java-based image processing program freely available from the National Institutes of Health) to the spectrophotometric determination you performed in Experiment 2.

The interdisciplinary field of microfluidics develops miniaturized technologies for manipulating the flow and reaction of small amounts of fluids. Microfluidics has the potential to revolutionize modern biology and medicine because it offers the advantages of working with smaller reagent volumes and shorter reaction times, which greatly reduce the cost required for an analysis. Current efforts are being made to integrate an entire laboratory's worth of analytical instrumentation onto a single chip to produce "lab on a chip" systems. Microfluidics has been applied to solve problems in diverse areas in both basic and applied sciences, and highly parallelized microfluidic systems are also being actively explored to improve existing technologies. Currently, highly integrated microfluidic chips with a thousand or more detection chambers can be produced and implemented easily.

Many types of materials are used to fabricate microfluidic channels and chips. Among these, PDMS elastomer has been extensively used in microfluidics because of its low cost, optical transparency, relatively simple processing, and biocompatibility. PDMS chips are usually fabricated using soft lithography, typically in three steps: rapid prototyping, replica molding, and sealing. Rapid prototyping produces the silicon mold; replica molding produces a solid PDMS chip from its liquid precursor; and sealing produces a seal between the PDMS and a rigid substrate, forming enclosed microfluidic channels. In addition, the PDMS surface can be chemically modified and used in multiple applications including protein separation and biological studies. Figure 1 presents a workflow of how to mimic the soft lithography fabrication process with coffee stirrers and Agar.

2. Introduction: Reynolds number

Reynolds number (R_e) is a dimensionless parameter, relating inertial to viscous forces in fluid flows:

$$R_e = LV\rho/\mu \quad (1)$$

where L is the channel length, V is the average fluid velocity, ρ is the fluid density, and μ is the dynamic fluid viscosity (resistance to shearing flows).

A high R_e implies that inertial forces are dominant whereas a low R_e implies that viscous forces are dominant. Therefore, R_e is used to differentiate between laminar and turbulent flows. Using water as

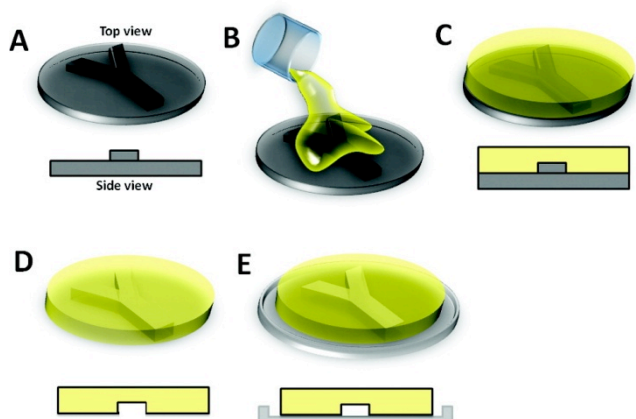


Fig. 1. Scheme for producing Agar chips using soft lithography. (A) A negative mold is made with desired features. (B) Liquid chip material is poured onto the mold. (C) Mold with liquid material is cured. (D) Solidified chip is peeled off and (E) placed on a rigid substrate for experiments.

the working fluid ($\rho = 1.0 \text{ g/cm}^3$ and $\mu = 0.010 \text{ g/cm}\cdot\text{s}$) with a velocity of 1.0 cm/s and a channel radius of 0.30 cm yields $Re = 30$. Typically, the transition from laminar to turbulent flow in round pipes occurs at $Re = 2000\text{-}3000$, so $Re = 30$ indicates that the flow is well within the laminar flow regime. One consequence of laminar flow is that turbulent mixing of fluids does NOT occur, which is a major problem in many microfluidics applications, e.g., attempting to mix iron(III) and salicylate on the chip. In your experiments you will manipulate solvent viscosity and channel geometry to attempt on-chip mixing.

3. Experimental

3.1 Chemicals

- Agar powder
- Food color (red and blue)
- Methanol
- Salicylate
- Ferric nitrate

3.2. Materials

- Twelve 5" aluminum weighing pans
- 7" wooden coffee stirrers (flat!)
- Single- and double-sided tape

3.3. Instrument Setup

- Peristaltic pumps (2)
- Pipette tips
- Digital camera
- ImageJ program

4. Procedure

4.1. Procedure for Agar Chip Fabrication

The main materials used to create the molds are aluminum weighing pans, wooden coffee stirrers, and tape (bring out your inner MacGyver!). The coffee stirrers are cut into different shapes and sizes depending on the design of the mold and then taped onto the aluminum pans using double sided tape, creating a specific pattern. **You will first produce two types of molds: Y-channel molds (see Fig. 2B), and zigzag molds.** Make four of each to make sure you have enough chips! For the zigzag molds, construct two inlets, similar to the Y channel but then have the mixing channel adopt a zigzag pattern on the plate. To enhance turbulence at the corners, small angle turns should be used – you can experiment with different designs (i.e., sharp and less sharp zigzag turns). The chips themselves are made by pouring liquid Agar onto the molds; these are left to cure 15-20 min. A general workflow for fabricating these Agar chips is shown in Figure 2.

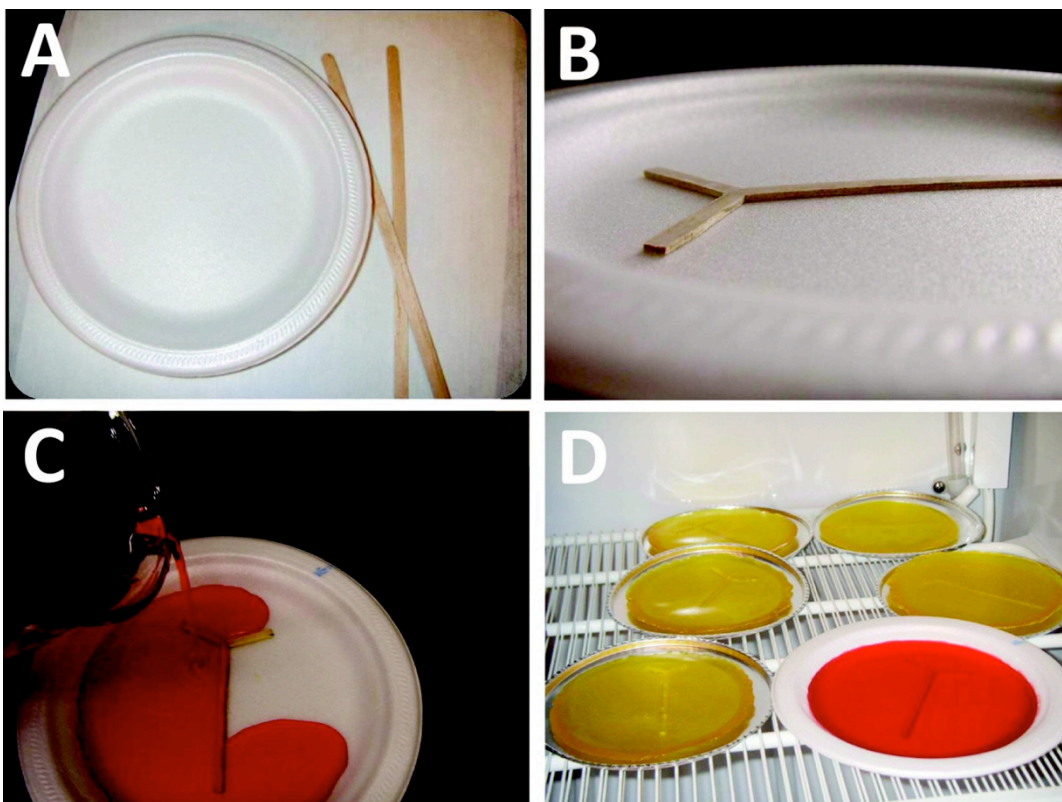


Fig. 2. General workflow for producing Agar chips using soft lithography approach. (A) Foam plate (here replaced with aluminum weighing pans) and wooden coffee stirrers are starting materials for making the mold. (B) A negative mold (here a Y-channel) is made with desired features using double-sided tape. (C) Agar is poured onto the mold. (D) The molds with liquid material are left to cure 15-20 min.

The following procedure should be followed:

1. Using double-sided tape and coffee stirrers, construct the desired shape molds on the aluminum weighing pans (the GSIs will provide you with sample molds). It is important to secure the entire length of each segment of the mold with tape, as any loose pieces can be displaced when the agar is added, thus ruining the chip. Arrange the channel(s) so that the entrances and exits are at the edges of the plate bottom. Label each mold with your group number.
2. For each mold, 4.5 g of agar powder is added to 150 mL of boiling DI water (use a hot plate, stirring constantly with a stir bar). To streamline the process, use 600 mL of water (1L glass beakers are provided for this purpose) and add 18 g of agar (this amount should be enough for four molds so repeat twice). NOTE: as soon as the agar has been added and the solution is cooling, it will begin to thicken immediately, making transfer of the solution difficult if the chips are not ready for immediate pouring.
3. SLOWLY pour the liquid agar into the molds prepared in steps 1-2. Ensure that the coffee stirrers are covered completely. Be careful – the solution and the beaker are hot – mittens are provided.
4. Allow the filled molds to cool on the lab bench until they begin to set.
5. At this point in time, the chips should be allowed to cure for 15-20 min. At the end of the day, store your chips in the cold room (GSIs will show you where it is) for continued use in lab period 2.

4.2. Characterization of Flow Regimes

After your chips have cured, they can be peeled from the molds, and placed on fresh aluminum pans for your experiments. It will be a little tricky to peel the chip without breaking it (however, you made more than one!), especially around the coffee stirrers. Please use patience and care when peeling your chips.

1. First, use a spatula to cut away the agar at the two inlets – this will allow you to insert the tubing from the peristaltic pumps easily (it can be laid down flat on the pan – make holes in the pans if needed). Also, cut out a detection window towards the end of the mixing channel.
2. Begin working with your Y channels. Liquid flow is delivered at the “top” of the Y by using the peristaltic pumps you acquainted yourselves with in Experiment 1B (it is preferable to use the one you calibrated in Experiment #1 but you will also need to calibrate a second pump). Set the knobs to deliver approx. 1 ml/min of solution (use pure water to calibrate, and make sure you measure the temperature and correct for density). Flow rates in the range of 0.8-1.2 mL/min is a good place to start. The tubings can be taped down with lab tape to improve robustness of the set-up. Inject blue and red water slowly but evenly into the separate channels and observe the flow profile. What happens where the red and blue fluids meet? Do they mix in the channel? Use the digital camera to document your observations. The camera attaches to the computer and images can be stored there.
3. The easiest way to manipulate R_e is to change the viscosity. Repeat the experiments above with methanol-based solutions (you can simply dilute the food color into methanol).
4. In order to calculate R_e for water and methanol (equation 1), the channel length (L) and the viscosity need to be determined. Use a ruler to determine L. For viscosity determination, viscometers and stop watches are available. Please consult the available data sheet to correct for the particular geometry of the viscometer you choose (they are not all the same). Please perform multiple measurements for determination of standard deviation.

NOTE: The available viscometers measure *kinematic* rather than dynamic viscosity (μ in equation 1). Kinematic viscosity (ν) relates to dynamic viscosity as: $\nu = \mu/r$ in which r is the liquid density. Thus, the R_e equation can be simplified to:

$$R_e = LV/\nu$$

– this rearrangement eliminates the need to determine r !

5. Perform the same experiments (red and blue water and methanol solutions) for your zigzag channels, document any differences compared with the Y-channel results.

4.3. On-chip Detection of Salicylate

One advantage of microfluidic devices is that, e.g., sample manipulation, separation, and detection can all occur on the chip. We will investigate whether detection of salicylate via complexation with iron(III) (see Experiment 2) can be performed on your chip. Ideally, if you found conditions in part 2 where mixing occurred (i.e., channel design, flow rate), those conditions should be used to mix the salicylate and iron(III) solutions on the chip. If such conditions were not found, please make a single channel design to infuse premixed solutions for generation of a calibration curve.

Similar to Experiment 2, prepare five standard solutions of sodium salicylate in deionized water. Use a 100 ml volumetric flask to prepare an initial stock solution of 100 mM (0.1 M) of sodium salicylate. You should weigh out sodium salicylate so you will know the exact molarity after you dilute the volumetric flask to mark. By dilution in appropriate volumetric flasks, prepare standards of 10 mM, 25 mM, 40 mM, 60 mM and 75 mM.

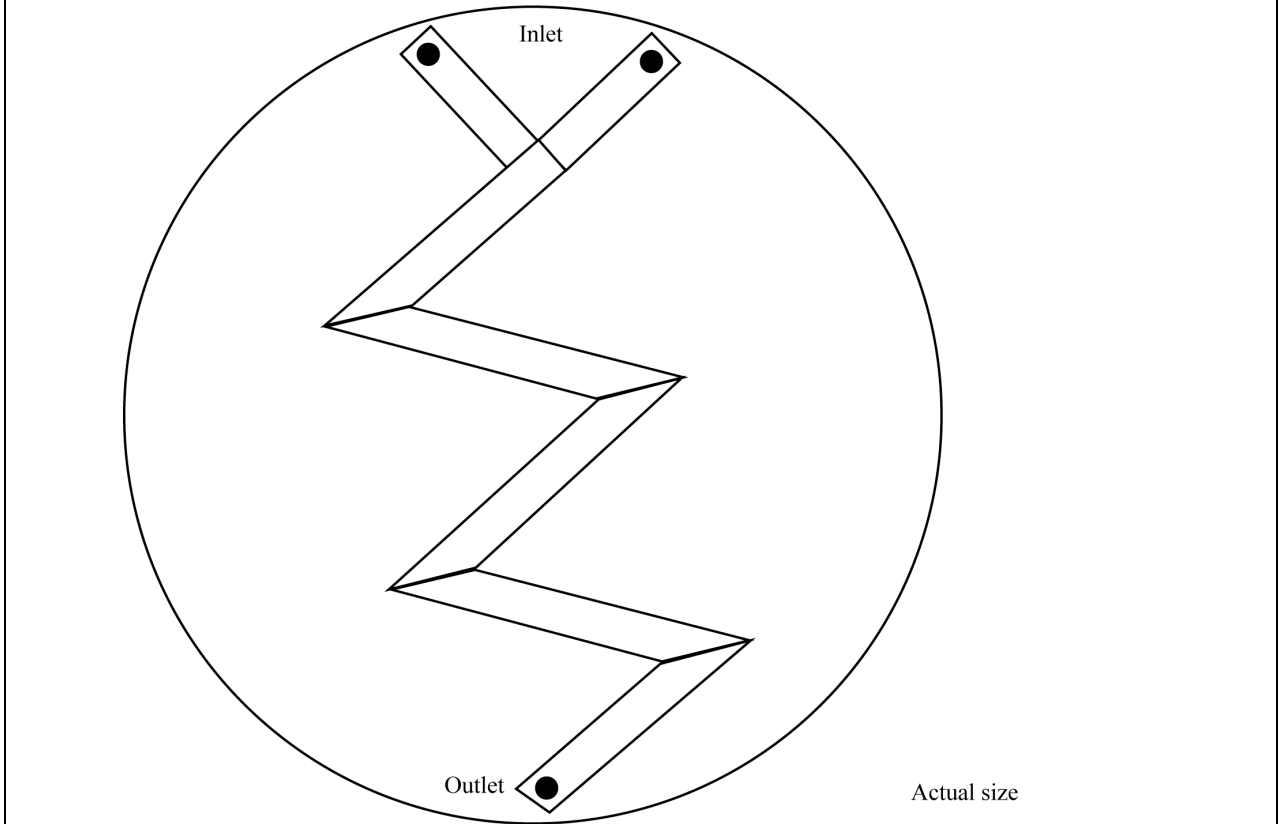
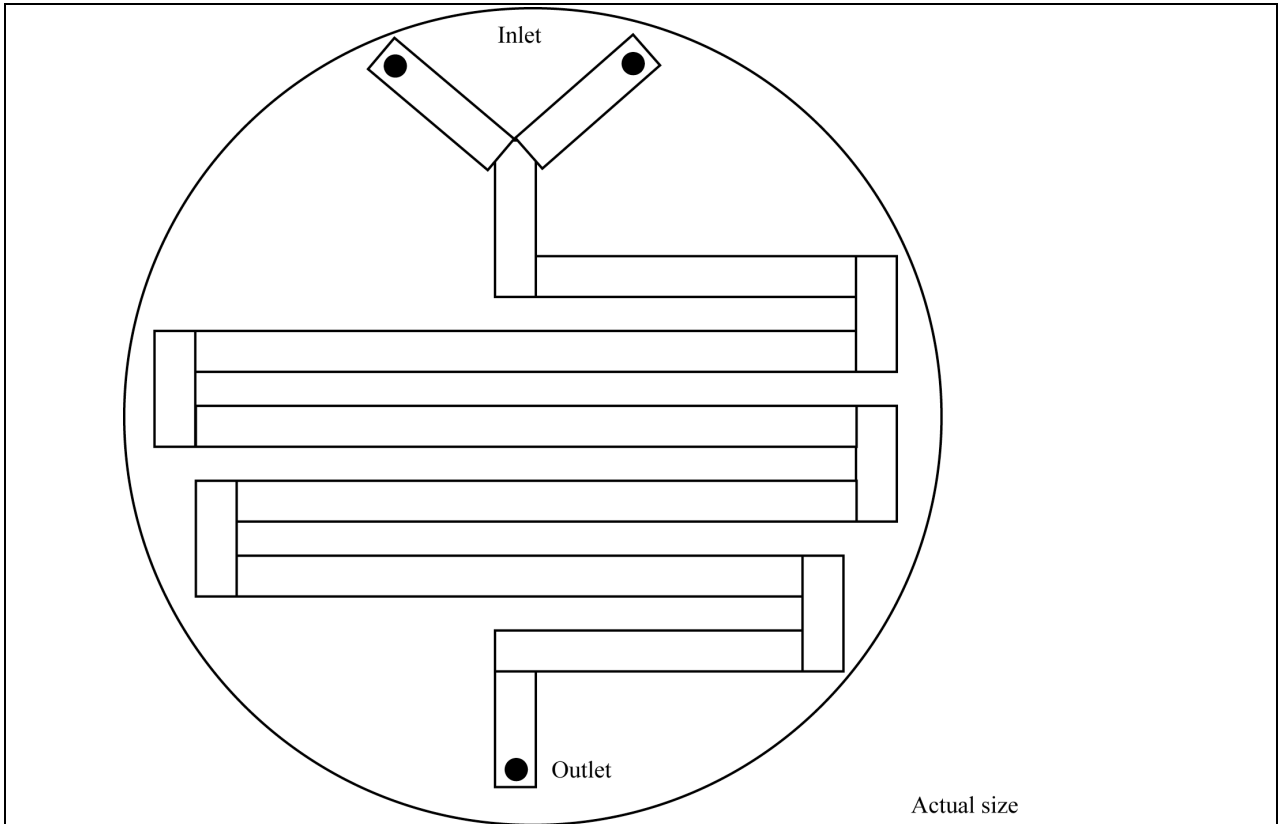
If mixing was achieved on the chip in part 2, use the chip design/conditions that allowed mixing and infuse your salicylate solutions into one channel while you are infusing acidic 10 mM ferric nitrate solution (stock in lab) into the other. If mixing was not achieved on the chip, mix 100 μ L of each salicylate solution with 10 mL ferric nitrate solution and then infuse this mixture into the single channel design. For either scenario, it is very important to start with the lowest concentration as there is some color carry-over in the chip. Document each concentration with the digital camera.

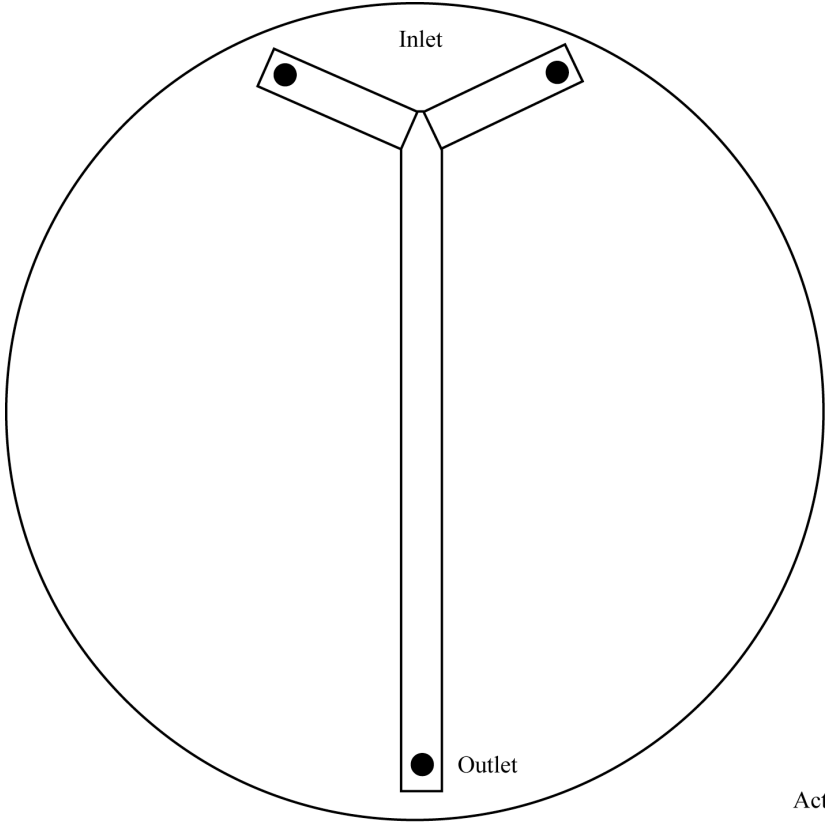
For RGB color analysis of the resulting images, the freeware ImageJ from the NIH is used. Open the ImageJ program on your computer and find the image you want to analyze (File→Open→Find your picture). Then select an area you want to analyze – make sure this area is well within the channel for best results. For analysis, select plugins→analyze→measure RGB. This command will provide five different values: a mean red (R), a mean green (G), and a mean blue (B), an average of the three, and a grayscale brightness. Write down these values in your lab notebook. Because the iron(III)-salicylate complex is purple, red and blue color is likely most representative ($(\text{red}(\text{mean}) + \text{blue}(\text{mean}))/2$) but you should also attempt to use just blue and just red. For generation of a calibration curve, plot RB(average), R, or B vs. concentration.

5. Lab Data Report

1. Describe the expected effects of channel geometry (Y vs. zigzag) on color mixing on the chip and how mixing relates to laminar vs. turbulent flow.
2. Provide example photographs of liquid flow in the Y- and zigzag channel chips and describe the observations.
3. Report R_e values for the water and methanol solutions.

4. Describe your iron(III)-salicylate experiments – was mixing feasible on the chip? If not, discuss changes you could do to the chip design to facilitate mixing.
5. Show your iron(III)-salicylate calibration curve and discuss pros and cons of the procedure you used in Experiment 2 vs. the one you used here.

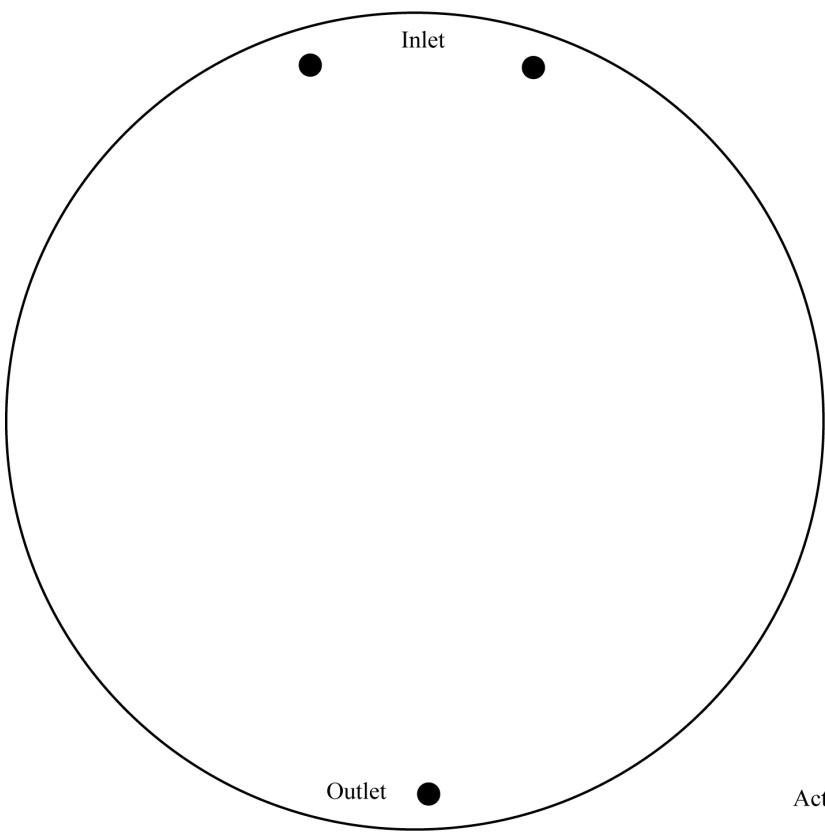




Inlet

Outlet

Actual size



Inlet

Outlet

Actual size

5.6.1 Pre-lab Questionnaire

CHEM 242 Lab Questionnaire

Section (Day/Time):

Please circle the number that best describe you.

Statements	Strongly Agree	Agree	Neutral	Disagree	Strongly Disagree
I have heard of microfluidics and I am aware of some of the applications of microfluidics.	5	4	3	2	1
I know the advantages of microfluidics devices in analytical techniques.	5	4	3	2	1
I am familiar with the terms laminar flow, turbulent flow, and diffusion in the context of fluid dynamics.	5	4	3	2	1
I have heard of Reynolds number (R_e) and I know what information I can obtain from this number.	5	4	3	2	1
I am able to list the factors that govern the mixing of two fluids in a micro-channel.	5	4	3	2	1
I can design a microfluidics chip that produces mixing of two fluids <i>via</i> turbulence primarily.	5	4	3	2	1
I can design a microfluidics chip that produces mixing of two fluids <i>via</i> diffusion primarily.	5	4	3	2	1
I understand the concept and importance of calibration curve in analytical techniques.	5	4	3	2	1
I can report the concentration of an unknown sample confidently.	5	4	3	2	1
I can explain microfluidics to my peers.	5	4	3	2	1

5.6.2 Post-lab Questionnaire

CHEM 242 Lab Questionnaire

Section (Day/Time):

Please circle the number that best describe you.

Statements	Strongly Agree	Agree	Neutral	Disagree	Strongly Disagree
I have heard of microfluidics and I am aware of some of the applications of microfluidics.	5	4	3	2	1
I know the advantages of microfluidics devices in analytical techniques.	5	4	3	2	1
I am familiar with the terms laminar flow, turbulent flow, and diffusion in the context of fluid dynamics.	5	4	3	2	1
I have heard of Reynolds number (R_e) and I know what information I can obtain from this number.	5	4	3	2	1
I am able to list the factors that govern the mixing of two fluids in a micro-channel.	5	4	3	2	1
I can design a microfluidics chip that produces mixing of two fluids <i>via</i> turbulence primarily.	5	4	3	2	1
I can design a microfluidics chip that produces mixing of two fluids <i>via</i> diffusion primarily.	5	4	3	2	1
I understand the concept and importance of calibration curve in analytical techniques.	5	4	3	2	1
I can report the concentration of an unknown sample confidently.	5	4	3	2	1
I can explain microfluidics to my peers.	5	4	3	2	1

1. Did you find the CHEM 242 Microfluidics laboratory interesting? Did this lab help you in learning microfluidics or deepening your understanding in this technology if you are already familiar with it?
2. Any aspects of the lab you liked or disliked about? What improvements could we do to enhance your experience in this lab?

Chapter 6

Conclusions and Future Outlook

6.1 Summary of Results

This dissertation presents negative-ion mode mass spectrometric methods to investigate RNAs and their complexes with small molecules or proteins. In Chapter 2, a mechanism for negative-ion electron capture dissociation (niECD) of RNA was proposed. This mechanism follows the gas-phase zwitterion theory in which the nitrogenous bases are protonated and the phosphate backbone is deprotonated, producing semi-complementary d' and w' ions. Electron capture occurs at the nitrogenous bases at different efficiencies; purine bases capture electrons more efficiency than their pyrimidine counterparts and form a much more stable radical species. As charge state increases, it becomes more difficult for gas-phase anions to capture an electron due to Coulomb repulsion, thus decreasing niECD efficiency. Proton-transfer reactions combined with niECD were demonstrated as a means of charge reduction, thus enhancing niECD performance.

In Chapter 3, we examined the effect of conventional electrospray solution on an RNA hairpin construct. Upon ESI from native-like solvent (10 mM ammonium acetate) and methanol-containing solvent (up to 50%), identical charge state distributions were generated, suggesting that methanol (in this range) has a small effect on the overall RNA conformation. Replica-exchange molecular dynamics sampled a wide range of hairpin conformations for given charge states. At lower charge states (5- and 6-), the RNA adopts a globular collapsed structure, owing to self-solvation. The 7- charge state showed retention of a hairpin, adopting a conformation that most closely resembles the native structure present in solution. Ligand binding assays with paromomycin, for example, in the presence of varied methanol content resulted in strongest binding at 0%

methanol (K_D value of 64 ± 6 nM). However the K_D value remained within one standard deviation up to 50% methanol, suggesting that the binding site is mainly unperturbed upon addition of methanol. Ligand binding assays at varied pH values showed strongest binding (lowest K_D value) at neutral pH.

Chapter 4 explored RNA-centric approaches for determining interaction sites within RNA-peptide complexes. Collisional activation provides full sequence coverage of the RNA moiety within RNA-peptide complexes while disrupting non-covalent interactions within the complex and thus losing site-specific information. On the other hand, niECD in combination with supplemental IR activation provides sufficient sequence coverage while not disrupting non-covalent interactions. Here, we also presented a method for selectively identifying RNA-peptide crosslinks within a peptide mixture as phosphate containing molecules (such as RNA) selectively dissociates upon IR irradiation with 10.6 μm photons.

Finally, in Chapter 5, a 2- week (8 hours total) microfluidics laboratory experiment for an undergraduate analytical chemistry course was developed and optimized. Students are introduced to the concepts of soft lithography as they design and characterize their own agar-based microfluidic chips. Students learn about the fundamentals of fluid dynamics as they approach the challenge of mixing in microfluidic channels. By varying solvent viscosity and channel geometries, terms that govern the Reynolds number, students are able to optimize channel and solvent conditions that promote optimal mixing within a channel. In the second week of the experiment, the optimal chip geometry is used to quantify the concentration of salicylic acid in complex with iron (III) via colorimetric analysis.

6.2 Future Work and Development

6.2.1 Expanding the Utility of PTR/niECD to Larger Ions

The performance of negative ion electron capture dissociation (niECD) is dependent on the precursor ion charge state.^{1,2} As charge state increases, it becomes more difficult for gas-phase anions to capture electrons due to Coulomb repulsion, thus decreasing

niECD efficiency. Methods, therefore, must be developed and implemented to reduce charge states in order to improve niECD efficiency for electrosprayed large ions. Ion-ion reactions, such as proton transfer reactions (PTR) with tandem mass spectrometry, have been demonstrated to expand the structural characterization of proteins. In Chapter 2, we demonstrated the utility of PTR/niECD for RNA hexamers and an 11-mer sequence. We seek to expand this strategy to larger ions and more biologically relevant systems, such as A-site/aminoglycoside complexes. As shown in Figure 6.1, efficient PTR of the 4- charge state of the 27-mer A-site construct results in 3- and 2- charge states. PTR increases signal abundance of electrospray-generated ions with m/z ratios beyond 3,000 in a 7-T FT-ICR mass spectrometer; an m/z range that should be ideal for niECD, resulting in sequence informative ions and ultimately the elucidation of binding sites.

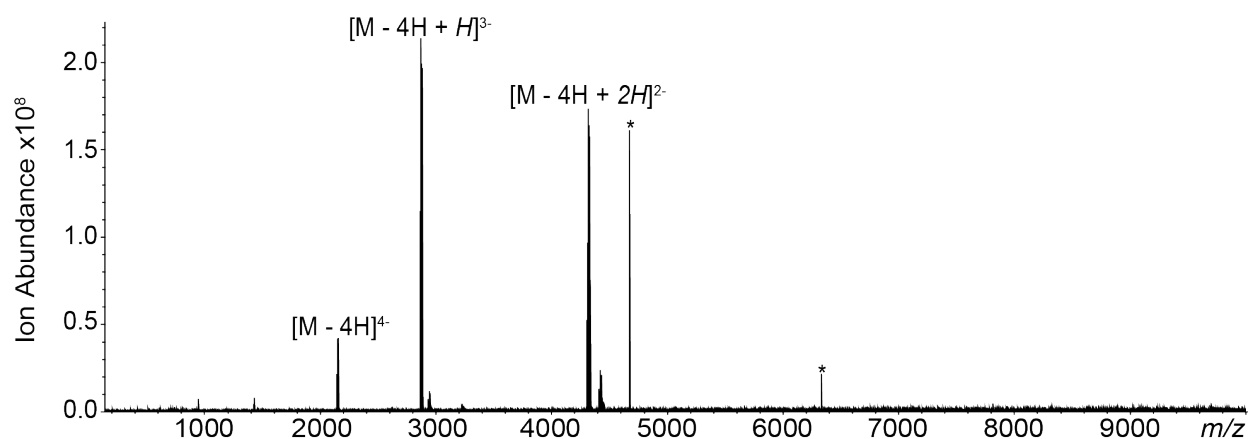


Figure 6.1. ESI-PTR mass spectra of a 27-mer RNA oligonucleotide anion. Upon PTR of the quadrupole-isolated, quadruply deprotonated species, triply and doubly deprotonated species at high m/z values are observed. PTR reagent was accumulated for 500 ms. Data collected on a solariX-XR FT-ICR mass spectrometer, at Bruker Daltonics (Billerica, MA), equipped with an ETD module for PTR and a ParaCell³ for mass analysis. * denotes noise peaks.

6.2.2 Further Interrogation of RNA Conformations in the Gas Phase

Native mass spectrometry has been shown to be effective in preserving protein solution-phase structure into the gas phase.⁴ Protein complexes and protein interaction networks have been studied extensively in this manner. Memory of the solution-phase structure has allowed mass spectrometry to accurately determine biologically relevant

structures. Much less is known about the fate of nucleic acids through the electrospray process although recent studies have begun to investigate this process.⁵ In the absence of bulk solvent, nucleic acids self-solvate, resulting in much more compact globular conformations. Similar results are presented in Chapter 3, where the lower charge states of a model RNA hairpin adopted more compact structures. These structures are not indicative of the native structure observed in solution. While replica exchange molecular dynamics (REMD) samples a wide conformational space, this method is highly dependent on charge location. In order to more accurately sample gas-phase conformations, a broader range of charge locations must be considered. The limited range of structures sampled so far may provide a rationale for the discrepancy in collisional cross sections observed for the low (5- and 6-) and high charge states (9-) observed in Chapter 3 compared with the experimentally determined ones. Gaining improved insight into RNA gas-phase conformation will allow us to better understand the biological relevancy of the lower charge states and ultimately use negative-ion mode ion mobility and mass spectrometry methods to study other classes of RNAs (e.g., noncoding RNA complexes).

6.2.3 Negative-Ion Mode RNA-Centric Mass Spectrometry for Revealing Interaction Sites within RNA-Protein Complexes

Interaction sites within RNA-protein complexes have been examined by mass spectrometry via solution-phase crosslinking strategies.⁶ Crosslinking is achieved, e.g., by UV irradiation of brominated RNA (uracils are replaced with bromo-uracil). At ~312 nm, highly reactive uracilyl radicals are produced, which react and form covalent bonds with protein side chains of closest vicinity. The subsequent crosslinked complex is digested with proteases (typically trypsin) and nucleases (typically RNase T1 and RNase A) in order to form crosslinks of peptides and mono-, di-, or tri- nucleotides (Figure 6.2). Crosslinks are analyzed via LC-MS/MS and the observed fragmentation patterns are compared with a control (non-crosslinked sample) in order to identify potential crosslinked peptides. The identified crosslinks are then compared to other

RNA-protein structural data when available. Urlaub and co-workers have used such workflows to successfully identify binding sites within RNA-protein complexes.⁷⁻¹²

Although conventional techniques are powerful for the elucidation of binding sites from crosslinking data, limited information about the interaction site within the RNA is generated. As a result, a complementary, RNA-centric workflow is required. In the proposed workflow (Figure 6.2), after UV irradiation, the RNA moiety (tRNA) of a tRNA-PRORP1 complex would be digested with just one nuclease in order to produce a larger RNA fragment relative to the conventional workflow. Digested crosslinks would be analyzed on an Orbitrap Fusion Lumos (which will be retrofitted with an IR laser). As proposed in Chapter 4, a data dependent acquisition (DIA) LC MS/MS approach would be used to flag and fragment RNA containing peptides in a single scan. The traditional workflow would be performed in a separate experiment to produce complementary crosslinking information (e.g., residue specific interactions within crosslinked peptides). RNA-protein interaction sites can then be compared to previous structural data.¹³

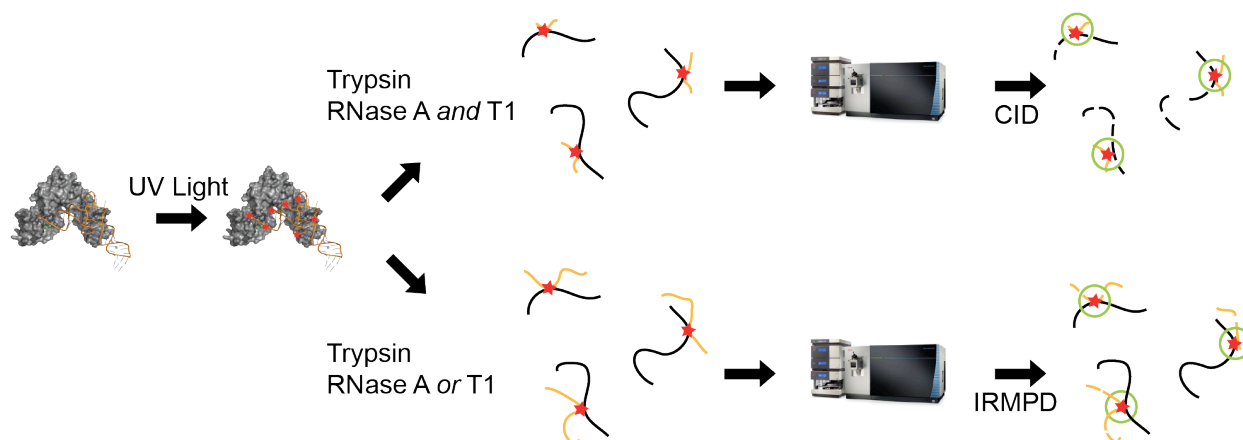


Figure 6.2. Proposed workflows for the study of the tRNA-PRORP1 complex; (top) conventional workflow identifying crosslinking sites at the residue level on peptides whereas (bottom) proposes an RNA-centric approach for crosslink identification.

6.3 References

- (1) Yoo, H. J.; Wang, N.; Zhuang, S.; Song, H.; Hakansson, K. Negative-ion electron capture dissociation: radical-driven fragmentation of charge-increased gaseous peptide anions. *J. Am. Chem. Soc.* **2011**, *133*, 16790-16793.

- (2) Hersberger, K. E.; Hakansson, K. Characterization of O-sulfopeptides by negative ion mode tandem mass spectrometry: superior performance of negative ion electron capture dissociation. *Anal. Chem.* **2012**, *84*, 6370-6377.
- (3) Boldin, I. A.; Nikolaev, E. N. Fourier transform ion cyclotron resonance cell with dynamic harmonization of the electric field in the whole volume by shaping of the excitation and detection electrode assembly. *Rapid Commun. Mass Spectrom.* **2011**, *25*, 122-126.
- (4) Heck, A. J. Native mass spectrometry: a bridge between interactomics and structural biology. *Nat. Methods* **2008**, *5*, 927-933.
- (5) Porrini, M.; Rosu, F.; Rabin, C.; Darre, L.; Gomez, H.; Orozco, M.; Gabelica, V. Compaction of Duplex Nucleic Acids upon Native Electrospray Mass Spectrometry. *ACS Cent. Sci.* **2017**, *3*, 454-461.
- (6) Kramer, K.; Sachsenberg, T.; Beckmann, B. M.; Qamar, S.; Boon, K. L.; Hentze, M. W.; Kohlbacher, O.; Urlaub, H. Photo-cross-linking and High-resolution Mass spectrometry for Assignment of RNA-binding sites in RNA-binding Proteins. *Nat. Methods* **2014**, *11*, 1064-1070.
- (7) Kuhn-Holsken, E.; Lenz, C.; Sander, B.; Luhrmann, R.; Urlaub, H. Complete MALDI-ToF MS Analysis of Cross-linked Peptide–RNA Oligonucleotides Derived from Nonlabeled UV-irradiated Ribonucleoprotein Particles. *RNA* **2005**, *11*, 1915-1930.
- (8) Lenz, C.; Kuhn-Holsken, E.; Urlaub, H. Detection of Protein-RNA Crosslinks by NanoLC-ESI-MS/MS using Precursor ion Scanning and Multiple Reaction Monitoring (MRM) Experiments. *J. Am. Soc. Mass Spectrom.* **2007**, *18*, 869-881.
- (9) Richter, F. M.; Hsiao, H. H.; Plessmann, U.; Urlaub, H. Enrichment of Protein-RNA Crosslinks from Crude UV-Irradiated Mixtures for MS Analysis by On-line Chromatography Using Titanium Dioxide Columns. *Biopolymers* **2009**, *91*, 297-309.
- (10) Kuhn-Holsken, E.; Dybkov, O.; Sander, B.; Luhrmann, R.; Urlaub, H. Improved Identification of Enriched Peptide RNA Cross-links From Ribonucleoprotein Particles (RNPs) by Mass Spectrometry. *Nucleic Acids Res.* **2007**, *35*, e95.
- (11) Schmidt, C.; Kramer, K.; Urlaub, H. Investigation of protein-RNA interactions by mass spectrometry-Techniques and applications. *J. Proteomics* **2012**, *75*, 3478-3494.
- (12) Kramer, K.; Hummel, P.; Hsiao, H.-H.; Luo, X.; Wahl, M.; Urlaub, H. Mass-spectrometric Analysis of Proteins Cross-linked to 4-thio-uracil- and 5-bromo-uracil-substituted RNA. *Int. J. Mass Spectrom.* **2011**, *304*, 184-194.
- (13) Howard, M. J.; Lim, W. H.; Fierke, C. A.; Koutmos, M. Mitochondrial Ribonuclease P Structure Provides Insight into the Evolution of Catalytic Strategies for Precursor-tRNA 5' Processing. *Proc. Natl. Acad. Sci.* **2012**, *109*, 16149-16154.